

UNIVERSITY OF LEEDS
School of Electronic and Electrical Engineering



STORM Lab

Science and Technology Of Robotics in Medicine

Investigating Ultrasound-Guided Autonomous Assistance during Robotic Minimally Invasive Surgery

Submitted in accordance with the requirements for the degree of
Doctor of Philosophy in Electronic and Electrical Engineering

November 2023

PhD Candidate:

Nils-Jorge Marahrens, M.Sc.

Supervisor:

Prof. Pietro Valdastri

Co-Supervisor:

Prof. Alejandro Frangi

Declaration of Authorship

The candidate confirms that the work submitted is his/their own, except where work which has formed part of jointly authored publications has been included. The contribution of the candidate and the other authors to this work has been explicitly indicated below. The candidate confirms that appropriate credit has been given within the thesis where reference has been made to the work of others.

1. Chapter 2 includes work from the jointly authored, soon to be submitted manuscript Jones, D., **Marahrens, N.**, Sarikaya, D. and Valdastrì, P. "Autonomy in Robot-Assisted Minimally Invasive Surgery." *Robotica*, ready for submission.

The work from this publication included in chapter 2 is my own. I, Nils Marahrens, contributed to the conception, literature review and writing, in particular the chapters on perception technologies and levels of autonomy. Dominic Jones contributed and led the conception, literature review, writing and revision. Duygu Sarikaya contributed to revising the sections involving artificial intelligence. Pietro Valdastrì contributed toward scientific support and manuscript revision.

2. Chapter 4 is largely based work from the jointly authored manuscript **Marahrens, N.**, Scaglioni, B., Jones, D., Prasad, R., Biyani, C.S. and Valdastrì, P. "Towards Autonomous Robotic Minimally Invasive Ultrasound Scanning and Vessel Reconstruction on Non-Planar Surfaces." *Frontiers in Robotics and AI*, vol. 178, 2022.

The work from this publication included in chapter 4 is my own. I, Nils Marahrens, contributed to and led the design conception, prototyping and implementation of the robotic setup, experimental design, execution and evaluation as well as manuscript conception and writing. Bruno Scaglioni contributed to the design conception and manuscript revision. Dominic Jones assisted in FSR sensor integration and calibration of the robotic platform. Raj Prasad and Shekhar Biyani contributed with feedback on the surgical boundary conditions and manuscript revision. Pietro Valdastrì contributed toward scientific support and manuscript revision.

3. Chapter 5 is largely based on work from the jointly authored publication **Marahrens, N.**, Dominic J., Murasovs, N., Biyani, C.S. and Valdastrì, P. "An Ultrasound-guided System for Autonomous Marking of Tumor Boundaries during Robot-assisted Surgery." *IEEE Transactions on Medical Robotics and Bionics*, under review.

The work from this publication included in chapter 5 is my own. Please note that at the time of submission, this publication is still under review and has not yet been published nor accepted for publication. I, Nils Marahrens, contributed to and led the extension of the robotic setup, experimental design, execution and evaluation as well as manuscript conception and writing. Dominic Jones helped with conception and manuscript revision, as well as assisting in experimental planning. Nikita Murasovs assisted in producing ultrasound phantoms. Shekhar Biyani contributed with feedback on the surgical boundary conditions and manuscript revision. Pietro Valdastri contributed toward scientific support and manuscript revision.

In addition the candidate has been co-author on following publications, without their content being part of this thesis:

1. Attanasio, A.*, **Marahrens, N.***, et al, "An open source motion planning framework for autonomous minimally invasive surgical robots", *IEEE International Conference on Autonomous Systems (ICAS)*, Montréal, QC, Canada, 2022, ***authors contributed equally**
2. Attanasio, A., Alberti, C., Scaglioni, B., **Marahrens, N.**, et al, "A Comparative Study of Spatio-Temporal U-Nets for Tissue Segmentation in Surgical Robotics." *IEEE Transactions on Medical Robotics and Bionics*, vol.3, no. 1, 2021.
3. Lloyd, P., Hoshidar, A. K., da Veiga, T., Attanasio, A., **Marahrens, N.**, et al, "A Learnt Approach for the Design of Magnetically Actuated Shape Forming Soft Tentacle Robots." *IEEE Robotics and Automation Letters*, vol. 5, no. 3, 2020.

This copy has been supplied on the understanding that it is copyright material and that no quotation from the thesis may be published without proper acknowledgement.

Abstract

Despite it being over twenty years since the first introduction of robotic surgical systems in common surgical practice, they are still far from widespread across all healthcare systems, surgical disciplines and procedures. At the same time, the systems that are used act as mere tele-manipulators with motion scaling and have yet to make use of the immense potential of their sensory data in providing autonomous assistance during surgery or perform tasks themselves in a semi-autonomous fashion. Equivalently, the potential of using intracorporeal imaging, particularly Ultrasound (US) during surgery for improved tumour localisation remains largely unused. Aside from the cost factors, this also has to do with the necessity of adequate training for scan interpretation and the difficulty of handling an US probe near the surgical sight. Additionally, the potential for automation that is being explored in extracorporeal US using serial manipulators does not yet translate into ultrasound-enabled autonomous assistance in a surgical robotic setting.

Motivated by this research gap, this work explores means to enable autonomous intracorporeal ultrasound in a surgical robotic setting. Based around the the da Vinci Research Kit (dVRK), it first develops a surgical robotics platform that allows for precise evaluation of the robot's performance using Infrared (IR) tracking technology. Based on this initial work, it then explores the possibility to provide autonomous ultrasound guidance during surgery. Therefore, it develops and assesses means to improve kinematic accuracy despite manipulator backlash as well as enabling adequate probe position with respect to the tissue surface and anatomy. Founded on the acquired anatomical information, this thesis explores the integration of a second robotic arm and its usage for autonomous assistance. Starting with an autonomously acquired tumor scan, the setup is extended and methods devised to enable the autonomous marking of margined tumor boundaries on the tissue surface both in a phantom as well as in an ex-vivo experiment on porcine liver. Moving towards increased autonomy, a novel minimally invasive High Intensity Focused Ultrasound (HIFUS) transducer is integrated into the robotic setup including a sensorised, water-filled membrane for sensing interaction forces with the tissue surface. For this purpose an extensive material characterisation is carried out, exploring different surface material pairings. Finally, the proposed system, including trajectory planning and a hybrid-force position control scheme are evaluated in a benchtop ultrasound phantom trial.

Acknowledgements

It seems surreal to think back how everything started at a techno club in Seoul, South Korea as part of iSMIT 2019 in the midst of a fun night. Thank you Pietro for being my supervisor and mentor for the past four and a half years. It's been a pleasure working with you and I am grateful for all the opportunities I had during my time at STORM Lab. Additionally, I also need to thank Harald Fischer for giving me the initial push at iSMIT 2019 to embark on this journey.

During my time at the University of Leeds I had the opportunity to work with some amazing people. Thank you Bruno for guiding me during my first two years. Thank you Dom for always having an open door and ear for me and assisting me in my academic journey. Thank you James McLaughlan for helping me out with everything ultrasound related. Thank you Samwise for all the entertainment and technical support (in that order).

Thank you everyone at STORM Lab. You guys are awesome and have made life in the lab so much more pleasurable! I will miss all the crazy lunch time conversations and the collective "Nils, Nils, Nils" chants. Also thank you Claire for always being there, particularly when last minute bookings needed to be done or when it was time to party.

Having done a PhD without music would be unthinkable for me. Thank you to everyone who is and has been involved in Leeds Project Big Band for letting me be part of this wild journey and supporting me to grow as a musician and person. You, along with the Leeds music scene and jam sessions at Golaccio, HEART and Hyde Park Book Club, just to name a few, were a much needed shelter and distraction from my PhD life at times. Thank you to everyone who is making the Leeds music scene as vivid as it is! I am also incredibly grateful to have met and befriended Gio, Alex and Nick, with whom I was able to share my passion and journey into the world of Jazz and grow as musicians and band Subrosa together.

Lastly, an incredible thank you to my family, to my parents Guni and Andres and to my brothers Christoph, Helge and Bene for supporting and encouraging me and for simply always being there for me. I love you all!

Acronyms

A-mode Amplitude mode	16
ADC Analogue Digital Converter	45
CA Cryoablation	xxvii
CT Computed Tomography	12
CUSA Cavitation Ultrasonic Surgical Aspiration	xxvii
CPP Closest Point Projection	xxvii
DC-Net Decoupling Network	xix
DL Deep Learning	3
DOF Degrees Of Freedom	xix
dVRK da Vinci Research Kit	v
ECM Endoscope Control Manipulator	8

EM Electromagnetic	21
EPSRC Engineering and Physical Sciences Research Council	4
ESU Electrosurgery Unit	xxii
ES Electrosurgery	xxi
FNR False Negative Rate	xxvii
FDR False Discovery Rate	xxvii
FSR Force Sensitive Resistor	xx
FBF Fenestrated Bipolar Forceps	xviii
HIFUS High Intensity Focused Ultrasound	v
ICP Iterative Closest Point	51
ICG Indocyanine Green	13
IMU Inertial Measurement Unit	xxi
IR Infrared	v
LDPE Low Density Polyethylene	95

LSTM Long Short-Term Memory	26
LND Large Needle Driver	xviii
MIS Minimally Invasive Surgery	1
MRI Magnetic Resonance Imaging	xvii
MTM Master Tool Manipulator	9
MWA Microwave Ablation	xxvii
OCT Optical Coherence Tomography	13
PCA Principle Component Analysis	25
PI Proportional-Integral	90
PSM Patient Side Manipulator	xvii
PAM Polyacrylamide	93
RAMIS Robotically Assisted Minimally Invasive Surgery	17
RFA Radiofrequency Ablation	xxvii
RICUS Robotic Intracorporeal Ultrasound	21

RL Reinforcement Learning	32
RMSE Root Mean Square Error	27
ROS Robot Operating System	xviii
SIFT Scale Invariant Feature Transform	18
STORM Science and Technology Of Robotics in Medicine	4
SUJ Setup Up Joints	8
TPR True Positive Rate	xxvii
TRUS Transrectal Ultrasound	17
US Ultrasound	v
UART Universal Asynchronous Receiver-Transmitter	45
VAE Variational Auto-Encoder	26

Contents

Declaration of Authorship	iii
Acknowledgements	vii
List of Figures	xvii
List of Tables	xxvii
1 Introduction	1
1.1 Motivation	1
1.2 Contributions	2
1.3 Structure	4
2 State Of The Art	7
2.1 Surgical Robotics	7
2.1.1 The da Vinci Surgical System	8
2.1.2 The da Vinci Research Kit	9
2.1.3 Autonomy in Surgical Robotics	10
2.2 Surgical Ultrasound Imaging	11
2.2.1 Comparison with other Surgical Imaging Technologies	11
2.2.2 Physics of Ultrasound Imaging	13
2.3 Robotic Ultrasound	17
2.3.1 Ultrasound Image Segmentation	18
2.3.2 Extracorporeal Robotic Ultrasound	19

2.3.3	Intracorporeal Robotic Imaging	21
2.4	Robotically Guided Tissue Treatment	28
2.4.1	Clinical Tools and Physical Mechanisms	28
2.4.2	Robotic Resection	32
2.4.3	Robotic Ablation	34
2.5	Summary	35
3	Platform Development for Autonomous Surgery	39
3.1	Requirements	39
3.1.1	Ulsurge Project Requirements	39
3.1.2	Technical Requirements	40
3.2	Robotic Infrastructure	41
3.2.1	Hardware Design	41
3.2.2	Software Infrastructure	43
3.3	Robot Calibration and Registration	47
3.3.1	Encoder Calibrations	47
3.3.2	Arm Co-Registration	48
3.3.3	Ultrasound Hand-Eye-Calibration	49
4	Autonomous Ultrasound Scanning and Navigation	53
4.1	Introduction	54
4.2	Materials and Methods	55
4.2.1	Positional Accuracy Assessment	55
4.2.2	IMU Kinematic Sensor Fusion	56
4.2.3	Vessel Segmentation	60
4.2.4	Visual Coupling Quality Estimation	62
4.2.5	Contact Force Detection	64
4.2.6	FSR Integration and Calibration	65
4.2.7	Planning and Control	66
4.3	Experimental Setup	70

4.4	Results	72
4.5	Conclusions	75
5	Autonomous Marking of Tumour Boundaries	77
5.1	Introduction	77
5.2	Materials and Methods	80
5.2.1	Pick-Up Design and Updated IMU Sensor Fusion	80
5.2.2	Surface Normal Estimation	82
5.2.3	Modified Electrosurgical Unit	84
5.2.4	Ultrasound Tumour Scan	87
5.2.5	Trajectory Generation	87
5.2.6	Control Scheme	90
5.3	Phantom Experiments	91
5.3.1	Metrics	91
5.3.2	Ultrasound Phantom Design	92
5.3.3	Phantom Trajectory Generation	93
5.3.4	Phantom Marking	94
5.4	Ex-Vivo Feasibility Test	96
5.5	Discussion and Conclusions	99
6	Autonomous Ultrasound-guided Tumour Ablation	103
6.1	Materials and Methods	104
6.1.1	HIFUS Physics	104
6.1.2	Requirements for Robotic HIFUS Probe Integration	104
6.1.3	Transducer Design and Interfacing	106
6.1.4	Interaction with the Tissue Surface	106
6.1.5	Membrane Material Characterisation	109
6.1.6	Trajectory Planning	112
6.1.7	Hybrid Position Force Controller Design	113
6.1.8	Pressure Profile Characterisation and Modelling	114

6.1.9	Beam Steering	118
6.2	Experiments	118
6.2.1	Experimental Setup	118
6.2.2	Planar Surface Testing	119
6.2.3	Non-Planar Phantom with Ultrasound Guidance	120
6.3	Discussion and Conclusions	122
7	Conclusions and Future Direction	127
A	Appendix	133
A.1	General Remarks	133
A.2	Nomenclature	133
A.3	Planar Projections	135
A.4	Quaternion Maths	135
A.4.1	Point Set Notation	136

List of Figures

- 1.1 Depiction of the different contributions in relation to the chapters of this thesis. 4
- 2.1 Overview over the dVRK infrastructure and comparison with the clinical mode. Where in clinical mode, the movement commands from the Master Tool Manipulator (MTM) are directly sent to the Patient Side Manipulators (PSMs) or Endoscope Control Manipulator (ECM) for execution, the dVRK provides an intermediary controller and middleware to receive data from and control each component of the formerly clinical system to be directly controlled by an external computer. 8
- 2.2 Mechanical structure of the Patient Side Manipulator (PSM) of the da Vinci surgical system incl. fulcrum point. The structure may be split up into a roll-pitch-insertion mechanism comprised of the first three joints and the detachable instrument comprised of the remaining three joints plus tool open and closure. Image taken from [1] 9
- 2.3 Different levels of autonomy as defined in [2]. Image taken from [3]. 10
- 2.4 **Left:** Liver tumour visible and circled in red on an Magnetic Resonance Imaging (MRI) scan (© 2019 MCC Gastrointestinal Oncology Video Library, Moffitt Cancer Center, Tampa, FL, USA). **Right:** ICG Visualisation of a kidney tumour, (© 2023 Jason Hawksworth, MD) 13
- 2.5 Basic A-Mode US: US signal is sent out and reflected at a tissue boundary, creating the intensity over distance signal that is depicted below. 15

2.6	B-Mode scan of a kidney (© Nevit Dilmen, CC BY-SA 3.0, via Wikimedia Commons)	17
2.7	Left: Ultrasound scan of a kidney tumour. Right: Tumour margin marking on the kidney surface (© 2019 Swedish Hospital, Seattle, WA, USA) . . .	22
2.8	Left: BK Medical X12C4 robotic drop-in Probe (© 2019 BK Medical). Right: Hitachi Aloka L43K robotic drop-in probe (© 2015 Hitachi Aloka Medical America, Inc.)	23
2.9	Da Vinci Canvas concept presented in [4]. Left: US image overlay (left) in the surgical video stream. Right: Needle feature present in the US image. Image from [4].	24
2.10	Force sensor suggested in [5]. Image from [5].	26
2.11	System for autonomous US-guided tissue ablation described in [6]. Left: Outline of the planar phantom structure with curved lines. Center: Waterjet tool for tissue cutting. Right: Optical markers used on US probe and cutting tool	33
3.1	Left: da Vinci ProGrasp TM . Center: da Vinci Fenestrated Bipolar Forceps (FBF). Right: da Vinci Large Needle Driver (LND). (© 2023 esutures.com)	41
3.2	Left: Tool engagement mechanism for standard da Vinci ProGrasp Tool. Image and concept from [7]. Right: Tool engagement mechanism for standard da Vinci Large Needle Driver. Image and concept from [8]	42
3.3	Robotic Pick-Up probe design including integrated sensors.	43
3.4	Robot Operating System (ROS)-embedded system structure showing hardware and software components as well as their interfaces for data interchange.	44
3.5	Benchtop setup used for experiments including the IR-tracking cameras and the tracked frame.	46

-
- 3.6 The different transformations obtained through calibration. Greyed out connections and transformations are either determined by design (e.g. PSM1TT to Tool) or measured (e.g. PSM1 to PSM1TT). More details on the stereo camera and its application can be found in Section 5.2.2. 48
- 3.7 **Top:** Wireframe used for hand-eye calibration. **Bottom:** Point clouds obtained from US scanning the phantom prior to ICP (Init), after ICP (ICP) and ground truth (GT). 50
- 4.1 System Structure: The current US frame is acquired and fed into the U-Net (entire image) and DC-Net (overlapping image slices). The segmentation results of the U-Net are post-processed, and ellipses are fitted around segmentation patches likely to correspond to vessels (upper path). The current vessel center is used to perform in-plane movements ($\mathbf{d}_{x,US}$) to center the vessel within the image. Recognised vessel centers from previous frames are buffered and used to estimate the center line and reorient the image normal $\mathbf{R}_{y,US}$ (rotation around \mathbf{y}_{US} - see also Figure 4.13). The parallel path with the outputs from the Decoupling Network (DC-Net) are compressed into coupling parameters that are used to adapt rotation around the image normal ($\mathbf{R}_{z,US}$) and compression movements ($\mathbf{d}_{y,US}$). If the probe alignment with the vessel and coupling is properly adjusted, the probe is progressed forward in the image plane normal direction ($\mathbf{d}_{z,US}$). 55
- 4.2 Position assumed by the kinematic model based on joint encoders (KIN) and measured by the IR tracking system in x - y -plane (**left**) and x - z -plane (**right**). 56
- 4.3 Position assumed by the kinematic model based on joint encoders (KIN) and measured by the IR tracking system in all six spatial Degrees Of Freedom (DOF)s. 57
- 4.4 Signal flow of the imu sensor fusion scheme. The kinematic pose and measured gravity vector are fused to obtain an updated orientation of the tool tip. Based on the new orientation an updated position is inferred leading to a fully updated pose. 58

4.5	<p>Left: Update of the end-effector orientation and global position \mathbf{T}_{TT} via attitude sensor fusion resulting in fused tool tip frame \mathbf{T}_{TTf}. Based on \mathbf{T}_{TTf}, \mathbf{T}_{US} is updated as well (not depicted for simplicity) Right: Visual representation of the post-processed outputs of the two Deep Neural Networks. The fitted ellipse (blue outline) closely tracks the segmentation results of the U-Net (area in red). The detected coupling quality by the DC-Net is visualised by the coloured bar on the top transitioning from green (good coupling) to red (poor coupling) and the blue circle representing the calculated c_{COM} parameter.</p>	59
4.6	<p>Training graphs of U-Net trained to segment vessel cross-sections</p>	61
4.7	<p>Structure of the DC-Net with four convolutional layers, each directly followed by a leaky ReLu layer and anisotropic max pooling. The flattened output of the first four layers is further processed through two dense layers, including an in-between ReLu and dropout layer ($p = 0.5$) and a final softmax layer for binary classification into coupled (0) and decoupled (1).</p>	63
4.8	<p>Force Estimation results in all three spatial directions using joint torques (KIN), linear regression model (LIN) and neural network (NN) in \mathbf{T}_{tt} coordinates.</p>	64
4.9	<p>Force errors of linear model force estimation on circular trajectory and planar surface with constant normal orientation compared to ground truth</p>	65
4.10	<p>Left: Experimental setup with the pick-up interface fixated and a movable scale pushing on the US transducer surface from below. Right: Force Sensitive Resistor (FSR) calibration results</p>	66
4.11	<p>Coupling adaption of the US probe via rotation around \mathbf{z}_{US} axis (equivalent to image normal vector), shifted into the center of the image probe. To determine the amount and direction of probe angle adaption the condensed c_{COM} parameter is employed (see Eq. 4.6)</p>	67

4.12	Outline of the hierarchical planning routine, employing different tracks for adapting the probe orientation and position with respect to the tissue surface or the reconstructed anatomy. The planner prioritises in the order of coupling over the centering of the vessel and finally the alignment of the vessel center line.	68
4.13	Considered coordinate Frames \mathbf{T}_{US} , \mathbf{T}_{TT} and \mathbf{T}_{PSM} Left: Before adaption of the image plane normal (poor orientation \mathbf{T}_{US} and \mathbf{T}_{TT}), Right: After adaption of image plane normal (ideal orientation), based on projected vessel center line (good orientation $\mathbf{T}_{US'}$ and $\mathbf{T}_{TT'}$)	69
4.14	Setup for the experiments, with a roughly overlaid outline of the vessel structure inside the phantom, the US pick-up probe with integrated Inertial Measurement Unit (IMU) and FSR and the reference block.	71
4.15	Box Plot showing the error distributions of the resulting scans using pure PSM- or IMU-based kinematics. Outliers are considered to be values outside the 1.5-fold interquartile range from each side of the box, demarked by whiskers (n=12596 data points from ten scans).	72
4.16	Resulting scans of the curved vessel branch using pure PSM-based (red), IMU-fused (blue) and IR tracked (green) kinematics. One of the PSM kinematic-based scans with particularly large skips is highlighted in black .	73
4.17	Vessel Scan from [7] showing 3D artifacts that could have been caused by backlash.	74
5.1	Left: Margin marking of a tumour (© 2019 MCC Gastrointestinal Oncology Video Library, Moffitt Cancer Center, Tampa, FL, USA). Right: Liver segment marking (© 2019 Detroit Medical Center, Detroit, MI, USA)	78
5.2	Concept overview: The internal tumour geometry is captured via US, projected onto the surface and eventually marked via an electrosurgical tool. .	79
5.3	Electrosurgery (ES) pick-up probe developed and using for ex-vivo experiments including shielded IMU	80

5.4	Normalised decoupling mean, as obtained from the DC-Net, over the performed fanning motion. Normalisation is obtained by dividing by the threshold value of 0.2.	82
5.5	Left: Plot of the measure signal of the capacitive sensors on either side of the US probe. Right: Capacitive sensor attached to the US probe in an attempt to detect and control the probe orientation relative to the tissue .	83
5.6	Left: Electrosurgery Unit (ESU) with custom built data extraction box Right: Schematic circuit diagram for data extraction box.	85
5.7	Measured output signals over different desired power settings and for contact and non-contact settings.	86
5.8	Comparison between different projection methods. Left: DPP using the same vector to project each point to the surface. Center: CPP using the closest point as surface projection. \mathbf{n}_{CCP} marks the surface normal plane at the surface point closest to the centroid of the tumour. A clear difference can be observed in the size of the different projections both on the surface marked as red contours $\{M_{PCV}\}$, as well as on the projected outline on \mathbf{n}_{CCP} plane. Right: Zoomed in view showing the different point sets and vector quantities involved in the calculation of the margin, in particular the surface normal $\mathbf{n}_i^{(ACV)}$ and surface point $\mathbf{p}_i^{(ACV)}$	88
5.9	Overview over the Pipeline: 1) A surface point cloud is extracted from the real sense and referenced to the robot via Aruco markers 2) Based on the surface information, a scan is acquired 3) The 3D geometry is projected onto the surface using one of the two suggested methods 4) The planned path is executed on a second robotic arm	89
5.10	Different areas used in the calculation of metrics.	91
5.11	Overview of setup and frames used. \mathbf{T}_{PSM1} and \mathbf{T}_{PSM2} sit at the fulcrum point of each PSM, while \mathbf{T}_{PH} is located at the center of the US phantom. \mathbf{T}_{CUT} and \mathbf{T}_{US} are the tooltip frame for the marking tool and US probe respectively, along with the tool-attached IR tracking frames \mathbf{T}_{IRCUT} and \mathbf{T}_{IRUS}	92

5.12	Left: Centroid Projected Scans. Right: Closest Point projection	94
5.13	Execution of the marking on the tissue surface	95
5.14	Experimental setup for ex-vivo trials, including frame with ArUco markers, IR-trackers and defined coordinate reference frames.	97
5.15	Left: Ex Vivo 3D results including point cloud. Right: Marked profile on the liver surface	98
5.16	3D point cloud of ex-vivo liver, overlayed with the different trajectories corresponding to Figure 5.15	99
6.1	HIFUS with tumour in focal region. The transducer, usually a piezo ele- ment is electrically stimulated to resonate in the ultrasonic spectrum. As the waves travel through and out of the lens they are focused to converge on the focal point. An acoustic matching layer between the lens and the tissue surface ensures that these waves are properly induced into the tis- sue and not reflected back towards the transducer. Inside the tissue the waves converge onto the focal point. Through constructive interference, the majority of the energy is focused around the focal point causing the local tissue to heat up, denaturizing cell and eventually leading to coagula- tive necrosis (death of tissue cells). Beyond the focal point the wave front diverges again, spreading the energy over a larger area.	105
6.2	Cut view of the assembled HIFUS probe design including the epoxy-filled casing with integrated water channels, the sealing ring as well as the piezo element.	107
6.3	HIFUS ablation of tumour	108
6.4	Concept of the water filled membrane (left) in its inflated yet unloaded state and (right) when in contact with the tissue exerting pressure profile p_t onto the an area A_I of the tissue, resulting in measured pressure change from p_0 to p_I inside the transducer and a reduction in dome height from d_0 to d_I	109

-
- 6.5 **Left:** Test Setup used to characterise the HIFUS membrane. The probe is mounted onto a load cell that attaches to a linearly movable stage. **Right:** Schematic drawing of the test rig. 110
- 6.6 Membrane Characterisation and subsequent fitting results for membrane pressure (kPa) over force (N) for different materials. Top left shows all data points and fitted curves overlaid, top right, bottom left and bottom right show the data and fitted curves for low, medium and high initial inflation pressure respectively and for different materials. 111
- 6.7 Membrane Characterisation and subsequent fitting results for indentation over pressure. Top left shows all data points. Top right, bottom left and bottom right show the data and fitted curves for rigid, gelatin and chicken respectively and for different initial pressures. 112
- 6.8 Trajectory planning process: **1.** Find the best surface point and project the entire point cloud onto the surface using that point's surface normal (\mathbf{n}_C) and calculation of the convex hull **2.** Shift the convex hull into the centroid of the mass, scale and duplicate it to end up with spiraling trajectory. **3.** Project up to the surface and fine-adjust all points to better match the surface normal. 113
- 6.9 Hydrophone setup at the University of Glasgow used to measure the pressure field. 114
- 6.10 **Left:** Hydrophone pressure field measurements of the HIFUS probe as measured by the research partners at University of Glasgow. The focal point of the HIFUS pressure field can be clearly observed at a distance of 25mm from the transducer. **Right:** 3D representation of the same measured pressure field, overlaid with the fitted curve 115
- 6.11 **Left:** Power drop of the transducer measured over time both for continuous wave (CW) and 50% duty cycle (DC) exposure as acquired by the Ultrasound Group at the University of Leeds via radiation force balance. **Right:** Precision Acoustics Radiation Force Balance used for validation (© 2023 Precision Acoustics Ltd.) 116

-
- 6.12 **Left:** Frame for phantom fixation, IR tracking and load cell measurements.
Right: Close up view of a single load cell element 117
- 6.13 **Left:** Planar trajectory executed on a block of agar **Right:** Experimental setup including robotically guided HIFUS probe and planar agar phantom. 119
- 6.14 **Left:** HIFUS position errors for planar trajectory execution comparing the errors between IMU-fused, IR-tracked and reference trajectory with one another. **Right:** HIFUS position errors for phantom trajectory execution comparing the errors between IMU-fused, IR-tracked and reference trajectory with one another. 120
- 6.15 HIFUS trajectory generated including normal orientation and the connecting vectors between surface and tumour target point. 121
- 6.16 HIFUS force during execution of planar, circular trajectory. 122
- 6.17 HIFUS forces during execution on non-planar phantom targeting concealed mass. 122
- 6.18 **Left:** HIFUS tumour coverage in 3D. **Right:** HIFUS tumour coverage projection in x-y plane, showing full but coarse coverage of the area. . . . 123
- 6.19 **Left:** HIFUS trajectory as with reference, IMU-fused and IR trajectories.
Right: Experimental setup with membrane conforming to surface shape . 124

List of Tables

- 2.1 Comparison of the most common techniques used for tumour visualisation.
 *Minor tissue heating due to US still being debated 14
- 2.2 Overview over the different material properties for human tissue affecting
 US wave speed measured at $1MHz$ [9]. 16
- 2.3 Technical specifications of the different robotic drop-in probes available . . 23
- 2.4 Comparison of different ablation techniques, High Intensity Focused Ul-
 trasound (HIFUS)), Cryoablation (CA)), Radiofrequency Ablation (RFA),
 Microwave Ablation (MWA) and Cavitation Ultrasonic Surgical Aspi-
 ration (CUSA). *Likely physically possible, however, no records yet of
 working miniaturised research or commercial prototypes 31
- 2.5 Comparison of different resection techniques. *Likely physically possible,
 however, no records yet of working miniaturised research or commercial
 prototypes 32

- 5.1 True Positive Rate (TPR), False Negative Rate (FNR) and False Discov-
 ery Rate (FDR) for the two different projection methods: Direct Point
 Projection (DPP) and Closest Point Projection (CPP) 94

Chapter 1

Introduction

1.1 Motivation

The recent decades have seen a significant reduction in surgery-induced trauma, transitioning from open to Minimally Invasive Surgery (MIS) such as laparoscopy starting in the early 1990s. In a similar vein, the rise of more dexterous robotic MIS platforms in the early 2000s has helped to enable this type of procedure to treat an ever increasing range of pathologies that might be difficult to reach and treat with standard laparoscopic tools. While this avenue is promising, the physical separation between the surgeon, who operates behind a distant console, and the operating tools, hidden inside of the patient, signify a drastic loss in fidelity of perception available to the surgeon that would have contributed to making a more informed treatment decision. This may particularly affect oncological surgical procedures which heavily rely on the precise localization and complete removal of all cancerous tissue, all while sparing nerves and other critical healthy tissues around it. During open surgery, it is common practice for the surgeon to further identify the tumour location manually as hardened tissue nodules. However, with the complete loss of tactile perception in laparoscopic and robotically assisted interventions, the main source for tumour localization remaining are preoperative images such as MRI, Ultrasound or CT scans. This process is further complicated by the time gap between pre-operative image acquisition and the surgical procedure, adding uncertainty about the location of the target region. This particularly applies to highly flexible organs such as the liver, where the positioning of the patient during surgery along with CO_2 insufflation may cause significant changes in position and shape of the organ [10]. To acquire real-time images during surgery and closer to the target region, the surgeon may resort to using a laparoscopic

or robotic intracorporeal US probe. So far, however, only very few surgical disciplines have yet turned towards intraoperative imaging [11, 12] as they require extensive training before they can be adequately interpreted by the surgeon [13]. A possible solution to this may be the employment of robotic and automated assistance to aid in acquiring US scans during surgery. While research on extracorporeal US has explored the use of automation, in particular robotics, this has not yet been the case for intracorporeal US settings that employ different manipulators and may rely on reduced sensory inputs due to the spatial constraints inside the patient's body. Aside from aiding the surgeon in acquiring scans, further autonomous assistance may be possible by leveraging the anatomical information extracted from these scans. The following work is set out to investigate both of these avenues.

1.2 Contributions

Motivated by this prospect, this thesis outlines the research around building and assessing a platform and approaches to enable US-guided autonomy during robotic surgery, starting from autonomous scanning over US-guided assistive functionalities towards autonomous tissue ablation. As an initial work in the area it covers and contributes to a range of different topics around enabling technologies for autonomous US-guided surgery (such as sensors and algorithms) as well providing reference for future work.

1. Platform and Approach for Ultrasound-Guided Autonomy

This work presents a platform concept for autonomous, US-guided surgery that shall serve as the basis for further research in this field. Its implementation around a standard surgical robotics platform, the dVRK, ensures that the quantitative results may serve as a benchmark or starting point for future endeavors in this field. The platform concept is developed in Chapter 3 and further extended and adapted in Chapters 4 to Chapters 6.

2. Analysis and Solution Approach for Kinematic Inaccuracies

A crucial aspect in autonomous systems is precision and reliability. Currently, a main obstacle with the da Vinci Research Kit is the huge system backlash. This work addresses this key point by developing and assessing a novel kinematic sensor fusion scheme. Few works so far have looked in more depth at the accuracy of a standard surgical robotics platform under autonomous circumstances, involving several robotic arms. This work is set out to comprehensively study the robotic system's accuracy under realistic circumstances, including loading conditions as they happen during grasping and guidance of

an US probe along a surface. For this purpose the platform integrates an Infrared (IR) tracking system that can provide ground truth positional data. The IMU sensor fusion scheme is introduced in Chapter 4, further adapted in Chapter 5, while the concept is applied and kinematic results analysed in Chapters 4 to Chapters 6.

3. Planning, Navigation and Control in an Intracorporeal Setting

A crucial aspect in autonomy is controlling the interaction between the robot and the tissue. Unlike other areas in robotics, surgical robotics can usually not rely on force sensing being available. For the purpose of US scanning, this work elaborates a Deep Learning (DL) based algorithm for estimating the quality of contact with the tissue, for detecting of the target structures in the ultrasonic image as well as a vessel center line estimation routine to navigate along tortuous vessel geometries (see Chapter 4). It further presents a solution for projecting margined tumour geometries onto the tissue surface (see Chapters 5) and planning of the surface constrained ablation path to reach the internal tumor structure (see Chapter 6).

To enable useful assistance based on the reconstructed US scans, a second robotic arm that can guide a cutting or ablation tool is integrated. A key part of this is finding means to enable interaction control with the surface. Therefore, the electrosurgical tool is characterised for different contact situations, to allow controlling the tool along a surface in the absence of reliable force sensing. An in-depth evaluation is carried out including a feasibility study on an ex-vivo porcine liver (see Chapter 5).

4. Ex-Vivo Feasibility Study

Aside from testing all algorithms on US phantoms, US scanning and tissue marking are translated onto an ex-vivo setup. In an initial feasibility study, this work shows that the developed approach for autonomous tissue marking works in an ex-vivo setting, giving further insights into an eventual translation onto more clinically realistic setups (see Chapters 5).

5. Ultrasound-guided intracorporeal robotic HIFUS

A novel concept for integrating a miniaturised HIFUS transducer into the robotic setup is presented in Chapter 6 and allows US-guided ablation during laparoscopic surgery. Central part of this is the development, characterization and assessment of a novel sensorised water-filled membrane that enables mechanical impedance matching, while also allowing the measurement of contact forces. Integrated into a basic trajectory planning algorithm, a hybrid force position control scheme is introduced that guides the HIFUS probe along the tissue surface while ablating an internal tumour structure.

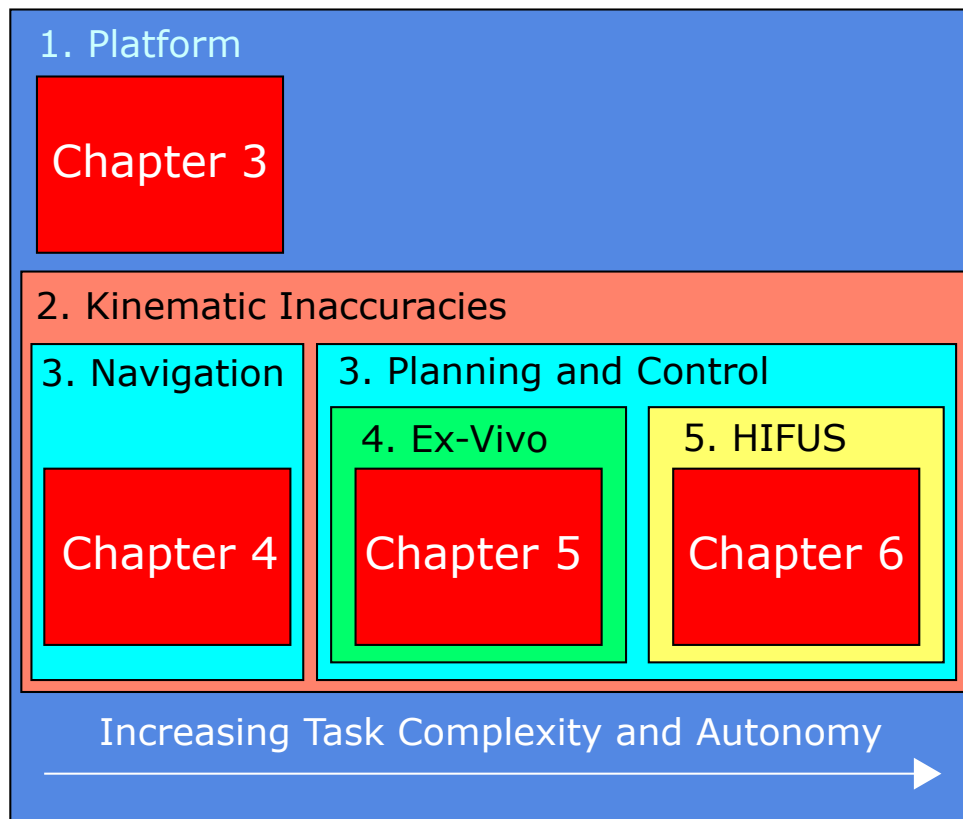


FIGURE 1.1: Depiction of the different contributions in relation to the chapters of this thesis.

Figure 1.1 shows the different contributions in relation to the chapters of this thesis.

1.3 Structure

This thesis presents the work during the course of my PhD project, carried out between May 2019 and October 2023 as part of the Science and Technology Of Robotics in Medicine (STORM) Lab. Its content is strongly associated with the UK Engineering and Physical Sciences Research Council (EPSRC) research project Ultrasurge (see Section 3.1.1). The thesis will proceed with the following structure.

Chapter 2 describes the technical background and the current state of the art in the field of US guided robotic surgery and the relevant parts of autonomy and automation in surgery with a focus on image-guided tissue treatment.

Chapter 3 describes the build up of the robotic platform, including an initial analysis as well as technical modifications, calibration and spatial registration of the different parts that are used to enable further research.

Chapter 4 outlines a novel approach to enable autonomous intracorporeal US scanning and navigation along vascular structures. It further serves as the foundation for image-guided control in the further course of the work.

Chapter 5 shifts the focus towards tumour surgery and assistive functions using a second robotic arm. In particular, a novel concept is devised and assessed, allowing the projection and marking of margined boundaries during hepatic tumour surgery. The final approach is demonstrated on ex-vivo porcine liver.

Chapter 6 expands from the assistive approach, outlining the autonomous ablation of a tumour via HIFUS. Therefore, it outlines the integration of a novel patient-specific device into the robotic setup including a sensorised extension to allow hybrid force-position control along pre-planned surface trajectories.

Chapter 7 as the final chapter in this work, summarises the findings and puts them into the wider context including remaining questions to be investigated in the future.

Chapter 2

State Of The Art

This section will give an introduction into the areas relevant to this work starting with surgical robotics in Section 2.1 and a general introduction of autonomy in this field in Section 2.1.3. Building up on this, Section 2.2 and Section 2.4 explore the state of the art in the field of robotic US scanning and tissue treatment in the context of robotic surgery respectively. Lastly, Section 2.5 summarises and discusses the findings in the context of this work.

Parts of this chapter, in particular Section 2.4.2 and Section 2.1.3, are due to be submitted as part of the following peer-reviewed journal paper:

Jones, D., **Marahrens, N.**, Sarikaya, D. and Valdastrì, P. "Autonomy in Robot-Assisted Minimally Invasive Surgery." *Robotica*, ready for submission.

2.1 Surgical Robotics

The commercial introduction of surgical robots dates back to the early 2000s, when the first systems gained FDA approval. While initially being targeted at heart surgery, the systems were soon redesigned and approved by the FDA as a tool to perform general laparoscopic surgery and gradually entered further surgical disciplines.¹ Particularly in

¹The Da Vinci (Intuitive, Sunnyvale, CA, USA) Surgical System gained FDA-approval in 2000, Source: <https://www.roboticoncology.com/history-of-robotic-surgery/>, accessed on 20/01/2020

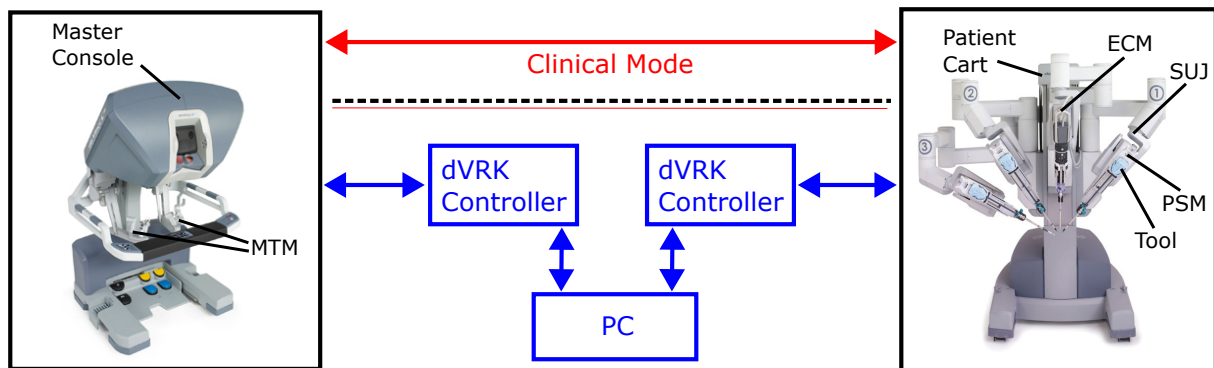


FIGURE 2.1: Overview over the dVRK infrastructure and comparison with the clinical mode. Where in clinical mode, the movement commands from the Master Tool Manipulator (MTM) are directly sent to the Patient Side Manipulators (PSMs) or Endoscope Control Manipulator (ECM) for execution, the dVRK provides an intermediary controller and middleware to receive data from and control each component of the formerly clinical system to be directly controlled by an external computer.

the area of urology, surgical robotics has become the standard means to perform operations, since the area in the small cervix may be difficult to reach by means of conventional laparoscopy. In addition to higher dexterity, these systems may offer improved 3D visualisation of the surgical scene as well as improved ergonomics.

2.1.1 The da Vinci Surgical System

For the last 15 years, the surgical robotics market has mainly been dominated by one particular system, the da Vinci (Intuitive, Sunnyvale, CA, USA) with a total of over 7500 systems in clinical use worldwide today². Despite technical upgrades, the general concept and mechanical structure of the robotic system has stayed the same over the last 20 years and 5 model generations da Vinci "Classic", S, Si, X and Xi.

Since its first conception, the system is composed of two physically separated components in a master-slave structure: the Master Console (master) on the surgeon side and manipulators (slaves) on the patient side. The latter consists of a platform (Patient Cart) with four passive arms referred to as Setup Up Joints (SUJ) that are only manually adjustable. Mounted on each of the four arms is an actively controllable manipulator. Three of them are Patient Side Manipulators (PSMs), equipped with controllable surgical instruments, and one Endoscope Control Manipulator (ECM), integrating a stereo endoscope (see Figure 2.1).

²According to company website <https://www.intuitive.com/en-us/about-us/company> (accessed on 13/07/2023)

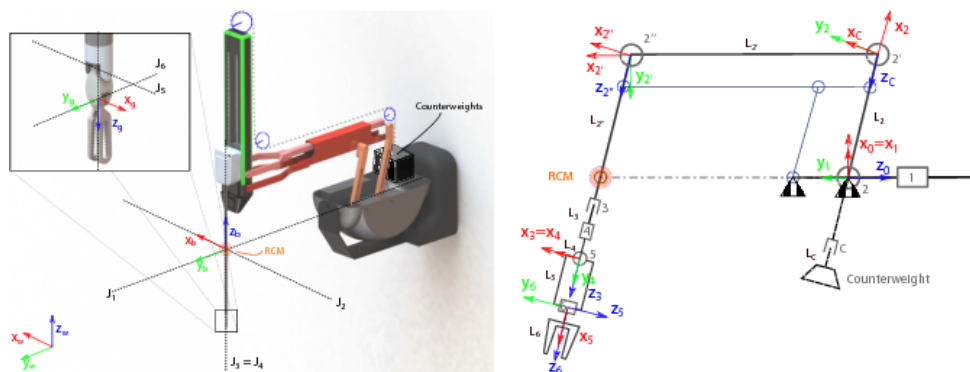


FIGURE 2.2: Mechanical structure of the PSM of the da Vinci surgical system incl. fulcrum point. The structure may be split up into a roll-pitch-insertion mechanism comprised of the first three joints and the detachable instrument comprised of the remaining three joints plus tool open and closure. Image taken from [1]

The console, also referred to as master console, hosts a stationary eyepiece through which the surgeon sees the stereoscopic video image from the endoscope, providing them with a 3D view of the surgical scene. To control any two of the four active manipulators, the console hosts two handpieces, referred to as Master Tool Manipulators (MTMs), which track the surgeon's hand movements for further translation onto the active manipulators on the patient side. Any movements of the MTMs imitated by the PSMs are scalable and filter out the natural tremor of the surgeon by default. By means of a foot pedal, the surgeon may select which of the three PSMs is linked to which MTM. (see Figure 2.1). To enhance intuition, the eye piece is directed downwards, towards the hands of the surgeon.

The PSM's tools are interchangeable during the surgical process and are built with the EndoWristTM technology, allowing the full control of the tool orientation, not possible in conventional laparoscopic surgery. The PSMs are designed to rotate around a fixed fulcrum, kinematically restricting movements and mechanical stresses around the incision point (see Figure 2.2). The structure may be split up into a roll-pitch-insertion mechanism comprised of the first three joints and the detachable instrument comprised of the remaining three joints plus tool open and closure.

2.1.2 The da Vinci Research Kit

To enable computerised control of the robot system, researchers at the John's Hopkins University developed the dVRK in 2014 allowing full control of a first generation da

Vinci robot (da Vinci "Classic"). In doing so, the signals of the MTM and PSM are fed into a custom built control box that can be accessed by a computer (see Figure 2.1). The added support of ROS middleware allows a full integration of these signals into a larger robotic environment. Over the years, as more institutions gained access to this technology, a community of dVRK research labs sharing their code in an open source fashion has emerged [14, 15]. The dVRK allows to directly set target values for the robot servo control loops. It also includes inverse kinematics to allow the specification of target values in Cartesian space.

2.1.3 Autonomy in Surgical Robotics






Full Control		Collaborative Control		Supervisory Control	
Level 0 No Autonomy	Level 1 Robot Assistance	Level 2 Task-Level Autonomy	Level 3 Supervised Autonomy	Level 4 High-Level Autonomy	Level 5 Full Autonomy
Surgeon controls all actions directly	Surgeon provides intention of action	Surgeon maintains control and selects tasks	Surgeon selects best plan and hands over control	Surgeon approves procedure	Level of Robot Control
Level of Human Control	Robot provides assistive feedback	Robot performs tasks and hands back control	Robot performs predefined procedure under oversight	Robot may decide to adjust plans during procedure	
					

FIGURE 2.3: Different levels of autonomy as defined in [2]. Image taken from [3].

Despite the advances in other areas such as dexterity and image quality, commercial surgical robotic systems lack autonomy and are merely used as tools for the teleoperation of surgical instruments [16]. Introducing autonomy into surgical robotics could help solve a plethora of issues, such as the shortage of medical staff, availability of adequately trained surgeons, and could potentially enable them to perform other, more relevant tasks or surgical procedures instead.

Autonomy in surgery is commonly clustered into six different levels (analogous to the six levels in automated driving), ranging from level 0 (no autonomy) to level 5 (full

autonomy). A depiction of this classification including some additional explanations for the different levels can be found in Figure 2.3. With each level, the amount of task the computer takes over increases while conversely the supervision necessary by a human decreases. Automation in medicine, particularly in surgery, is still relatively low compared to other sectors. Some specialised commercial systems such as the former ROBODOC system (currently called TSolution One Surgical System from THINK Surgical, Fremont, CA, USA) already fall under level 3 (conditional autonomy) and even systems of level 4 (high autonomy) such as the Veebot are planned to be commercialised [17]. However, current commercially available general surgical robotic systems operating in soft tissue environments, still fall into level 1 autonomy providing merely functionalities such as tremor filtering or motion scaling. Reasons for this discrepancy may be the complexity of perception, registration and reliable manipulation of soft tissue.

Research on the other hand has produced quite a few systems of autonomous surgical robotic systems up to level 4 autonomy. Examples of these are:

- Level 1: Haptic Feedback [18]
- Level 2: Palpation [19, 20], tissue retraction [21, 22] endoscope guidance [23]
- Level 3: Suturing [24] , knot tying [25]
- Level 4: Debridement and tumour resection [8, 26], suturing [27, 28]

In these works, autonomy is typically enabled using the endoscopic camera image [29] or specialised cameras [27, 28], while only few works such as [30] and [31] have relied on real-time tissue imaging as a reference point for autonomy. Further autonomous applications will be explored in the upcoming section, particularly in the context of US guidance (see Section 2.2) and tissue treatment (see Section 2.4). A broader overview over the topic of autonomy in surgery can be found in [32].

2.2 Surgical Ultrasound Imaging

2.2.1 Comparison with other Surgical Imaging Technologies

Imaging is a widely used tool in medicine to more accurately assess a patient's health condition, as well as plan and execute therapeutic interventions. Around surgical interventions, it may be divided into three types, depending on when it is performed: pre-operative

imaging (before the surgical procedure), intra-operative imaging (during a surgical procedure) and post-operative imaging (after a surgical procedure). Additionally, depending on the imaging technology further distinction can be made regarding where the imaging probe is placed or how it is inserted into the body mainly endoluminal (through orifices), intracorporeally (inside the patient) and extracorporeally (outside of the patient). Note that the term intracorporeally further implies that it is done interventionally or intra-operatively, whereas extracorporeal applications may be done at any stage as they don't require a procedure to gain access to the imaging site.

While pre-operative and post-operative imaging are already routinely performed or even necessary to plan surgical treatment or assess the outcome, intraoperative imaging is not routinely performed, despite the immense benefit of real-time information. Currently, both MRI (see Figure 2.4) and Computed Tomography (CT) scans are routinely performed preoperatively. These imaging techniques, however, may not be suitable for intra-operative imaging, due to their size (e.g. MRI) or their high radiation dose (e.g. x-ray based methods such CT), implying they should only be used when absolutely necessary.

Further aspects to be considered are the achievable resolution and usually tied to that, the achievable imaging depth. Ideally desired is imaging close to the target regions, depths of several centimeters and submillimeter resolution to capture structures within the tissue e.g. subsurface tumours. Note that these may slightly vary depending on the application.

A further consideration towards applying imaging technologies in the context of robotic automation is their possibility to be spatially referenced towards the robotic base frame. Only if spatial reference is warranted, can the robot adequately employ the information extracted from the image towards executing informed actions. While it is technically feasible to calibrate and reference larger equipment such as C-arm x-ray machines with a robotic system (e.g. via prior registration or integration of further robotic arms), this may be largely impractical as it would fixate the setup between calibration and surgical procedure. Therefore, it is much more convenient to rely on technology that is miniturisable and thus integrable directly into a surgical robotic tool for an intracorporeal application.

US is a widespread and versatile, yet still not very commonly used method across surgical disciplines and interventions for intraoperative imaging. US probes are easily customisable to fit small form factors depending on the specific application and required resolution. A main drawback preventing a widespread use of intraoperative US is reported to be the lack of adequate training and general difficulty to interpret the resulting images [11]. The amount of energy transmitted by US imaging probes is relatively low, causing minor

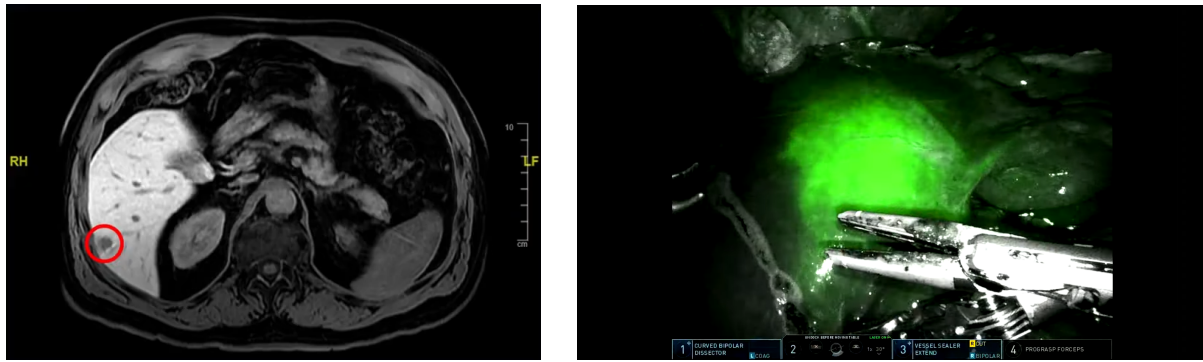


FIGURE 2.4: **Left:** Liver tumour visible and circled in red on an MRI scan (© 2019 MCC Gastrointestinal Oncology Video Library, Moffitt Cancer Center, Tampa, FL, USA). **Right:** ICG Visualisation of a kidney tumour, (© 2023 Jason Hawksworth, MD)

heating of the tissue. The effects of this on the organism are still an ongoing topic of debate [33].

A further technique commonly used in tumour surgery, is fluoroscopic imaging involving dying agents such as Indocyanine Green (ICG), to visualise tissue perfusion and thus highlighting the differing perfusion patterns of tumours compared to healthy tissue [34]. Alternatively, recent works have suggested the use of radio detecting skins that are attached to the surface and change their colour based on beta particle exposure [35]. These methods may also be used in combination with pre-operative data. While this gives the surgeon a good estimation of the tumour's location close to the tissue surface, it does not help outlining the tumour's structure deeper within the organ. A similar issue occurs in surface imaging technologies such as Optical Coherence Tomography (OCT), making a potential application in laparoscopic tumour surgery more constraint.

Table 2.1 summarises the previously outlined findings. Considering the requirements for robotic surgery, the most adequate technology for robotic automation in surgery is US, being miniaturisable, non-ionising, with tuneable resolution and depth and already largely available as commercial medical devices.

2.2.2 Physics of Ultrasound Imaging

The previous analysis justifies looking deeper at US imaging in the context of robotic surgery. Outline the physics behind US imaging (Section 2.2.2) and present an in-depth analysis of existing technology for robotic US guidance both extracorporeally (Section 2.3.2) and intracorporeally (Section 2.3.3). Please note that the following discussion is

TABLE 2.1: Comparison of the most common techniques used for tumour visualisation.
*Minor tissue heating due to US still being debated

Technology	Miniaturisable	Depth	Maximum Resolution	Harms	Further Remarks
US [33]	Yes	Variable	Up to micrometer	None*	Obstructed by air or hard tissues
MRI [36]	No	Variable	Up to micrometer	None	Very large and expensive setup
CT [37]	No	Through	Millimeter	Ionizing Radiation	Clear resolution of soft tissue only with toxic contrast agents
ICG [34]	Yes	Sub-surface	Coarse	Toxicity	Limited to visualising high perfusion
OCT [38]	Yes	Sub-surface	Micrometer	None	Ideally requires very steady and precise positioning

implied to be around minimally invasive (e.g. laparoscopic) procedures, meaning the term surgery or intervention excludes open surgical interventions.

US refers to mechanical waves above $20kHz$ in frequency. For most medical applications it will be in the range of $2-18MHz$. US waves will travel at different velocities depending on the mechanical properties of the material they are induced into. For a given material of density ρ and stiffness k , the velocity of sound c can be calculated as

$$c = \sqrt{\frac{k}{\rho}} \quad (2.1)$$

An important quantity that can further be derived from these quantities is the acoustic impedance z

$$z = \rho \cdot c = \sqrt{\rho \cdot k} \quad (2.2)$$

Boundaries between materials of different acoustic impedances will present obstacles to the waves and cause a fraction of it to be reflected, while the rest of the wave will travel further onwards. The higher the difference in impedance between the two tissues comprising a boundary are, the larger the fraction of the signal that is being reflected back rather than

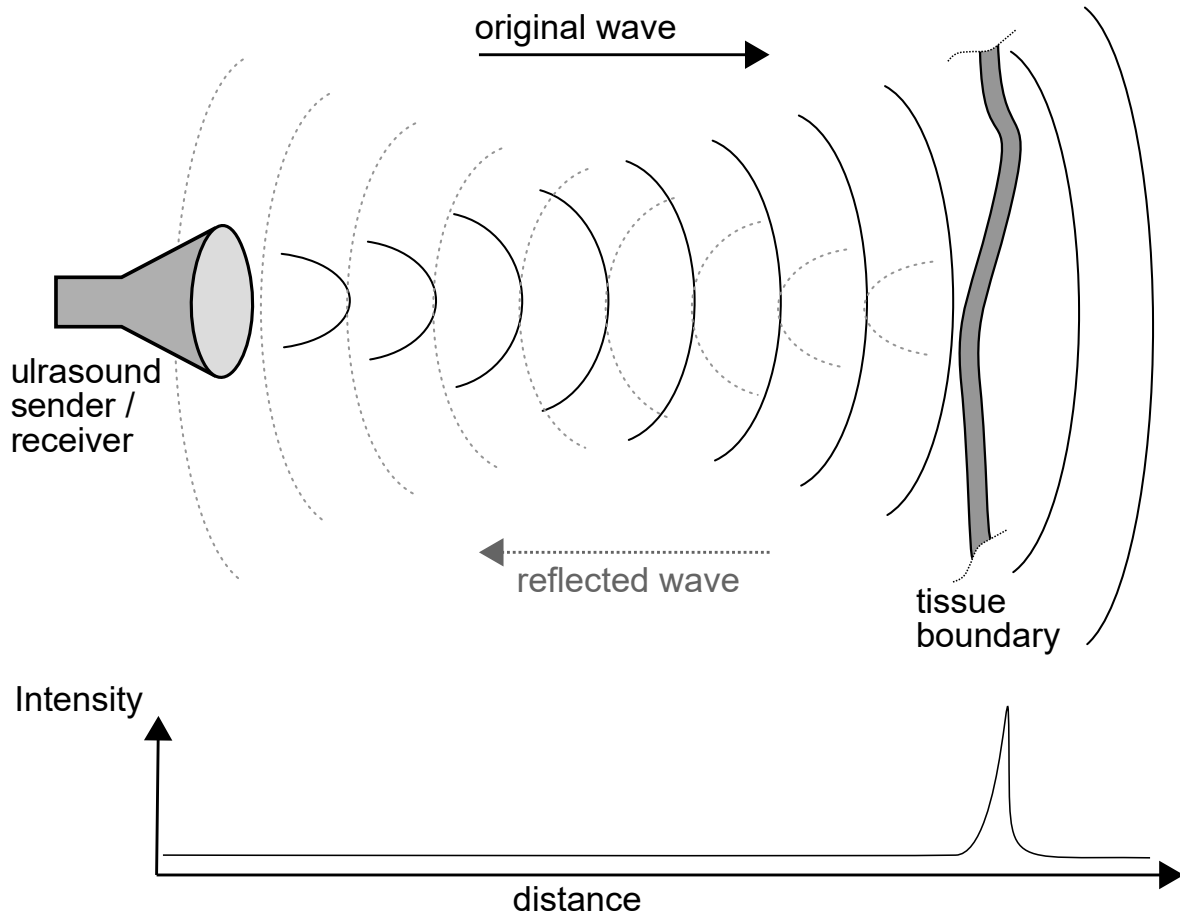


FIGURE 2.5: Basic A-Mode US: US signal is sent out and reflected at a tissue boundary, creating the intensity over distance signal that is depicted below.

transmitted through the boundary. The quotient of intensities between incident (I_i) and reflected (I_r) wave at a boundary between materials of impedance z_1 and z_2 is given by

$$\frac{I_i}{I_r} = \left(\frac{z_2 - z_1}{z_2 + z_1} \right)^2 \quad (2.3)$$

By sending out a known, pulsed signal and subsequently registering the timing and intensity of incoming reflection echos, this phenomenology can be use for imaging purposes. Figure 2.5 shows a schematic drawing of this physical process. Note that we do usually not know the precise mechanical properties of the material e.g. tissue we are imaging. However, we generally assume a mean propagation speed as soft tissues all fall in a similar range between $1460 \frac{m}{s}$ (adipose tissue) to $1610 \frac{m}{s}$ (connective tissue) [9]. The mechanical properties of different tissues is depicted in Table 2.2. The depiction of this

one-dimensional signal is also referred to as Amplitude mode (A-mode). To receive and reconstruct a two-dimensional US image, several US transducer elements, each capable of sending out and receiving an ultrasonic wave, are aligned into an array. By sequentially pulsing segments of the US element array, the subsequently received wave signals of all elements can be reconstructed into a 2D grey-scale image such as the one shown in Figure 2.6. By applying different types of waves and post-processing them accordingly, a variety of physical properties can be measured including tissue stiffness (elastography) or velocity fields (doppler US) [33]. The image resolution and penetration depth of an US probe are directly and inversely proportional to the wavelength of the applied signal as higher frequencies get attenuated more strongly and thus cannot penetrate the tissue as deeply as lower frequency waves. Depending on the application a trade-off between a sufficient penetration depth and resolution has to be made to adequately resolve the structures of interest. [33]

Critical for good US images is also smooth and steady acoustic coupling between the US probe and the tissue surface. To improve coupling and reduce the reflective effects of the boundary, a coupling agent such as water or a gel is usually applied between probe and the outermost tissue surface it is in contact with.

TABLE 2.2: Overview over the different material properties for human tissue affecting US wave speed measured at $1MHz$ [9].

Tissue Type	Density ($\frac{Kg}{m^3}$)	Longitudinal Wave Velocity ($\frac{m}{s}$)	Acoustic Impedance ($10^6 \frac{Kg}{m^2s}$)
Air	1.2	330	0.0004
Lung	400	440–500	0.18–0.20
Adipose tissue	920	1460	1.35
Water	1000	1480	1.48
Liver	1060	1550	1.64
Spleen	1060	1560	1.65
Blood	1060	1560	1.62
Kidney	1040	1560	1.62
Muscles	1070	1590	1.70
Connective tissue	1120	1610	1.80
Cartilage	1100	1665	1.85
Skin	1150	1730	1.99
Bone	1380–1810	2700–4100	3.75–7.3

US imaging in surgery may be divided into three categories depending on the location of their application: endoluminal, intracorporeal and extracorporeal US. In endoluminal US the body is entered through natural orifices to perform scans via luminal organs. A

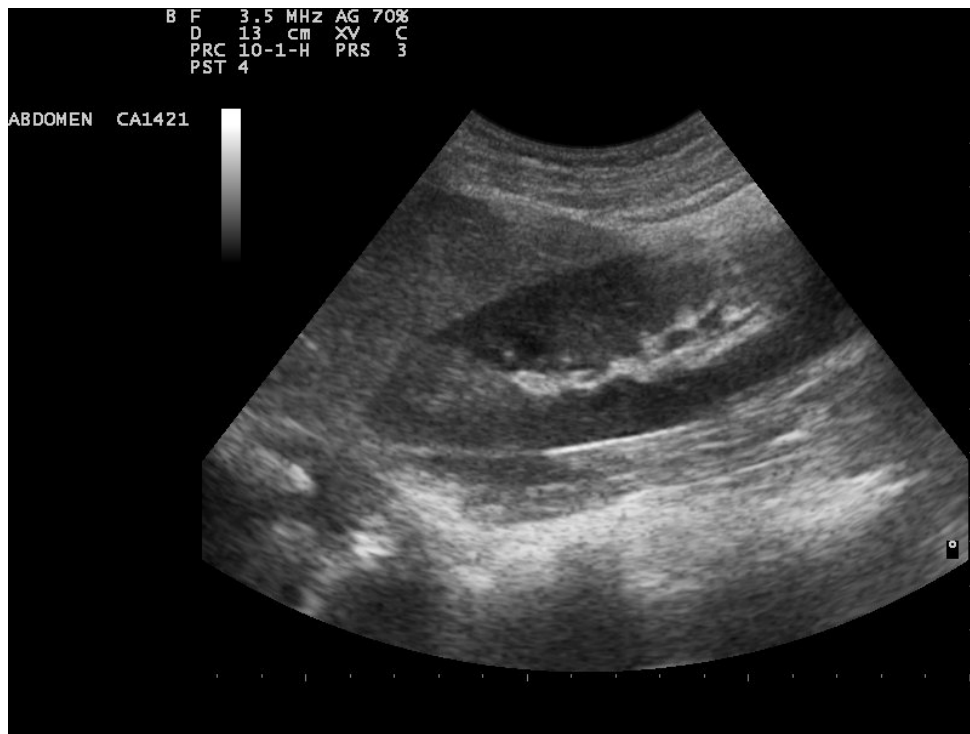


FIGURE 2.6: B-Mode scan of a kidney ((© Nevit Dilmen, CC BY-SA 3.0, via Wikimedia Commons))

commonly used technique of this category is Transrectal Ultrasound (TRUS), where an US probe is inserted into the patient's rectum and used to visualise organs such as prostate or bladder through the bowel wall. In extracorporeal US, on the contrary, the probe is guided along the patient's body externally e.g. to visualise gall bladder or kidneys. Lastly, in intracorporeal US, the probe is directly applied to the organ surfaces inside the patient during surgery. Each category presents its own set of requirements and challenges, resulting in different US systems in particular in terms of the size of the US transducer and the applied frequency to result in the required resolution for the target region and application.

2.3 Robotic Ultrasound

After establishing the motivation and physics of US more generally, a more in depth overview over the research associated with the wider field of robotic US guidance will be given. Whereas the general focus of this work will be intracorporeal US during Robotically Assisted Minimally Invasive Surgery (RAMIS), this literature review will also extend to

robotically guided extracorporeal US, due to their similarity in guiding a probe via a robotic manipulator and for it being a more established field.

2.3.1 Ultrasound Image Segmentation

The foundation of any image-guided robotic systems is the detection of representative features. Over the years many approaches have been suggested to detect single features up to full anatomical structures in the image that can inform automated clinical decisions and guide robotic motions.

De Luca et al. [39] compare four different approaches for feature tracking in 2D liver US employing the 2015 CLUST (Challenge on Liver Ultrasound Tracking) dataset³. The dataset includes scans of healthy livers under free breathing motion, with the goal of tracking landmarks (e.g. vessels) in the image in a sequence of scans. They conclude that the evaluated approach by Makhinya et al. [40] which employs vessel models and optical flow, is the only method applicable in real time while having the second highest tracking accuracy (mean: 1.44mm, standard deviation: 2.80mm). The highest accuracy is achieved by Hallack et al. [41], which builds on a moving window tracking method and Scale Invariant Feature Transform (SIFT) for non-linear image registration (mean: 1.21mm, standard deviation: 3.17mm). Further approaches are documented in the ranking available on the CLUST webpage³. Shepard et al. [42] present an approach (ranked second on the dataset on 18.02.2020), which employs block matching based on normalised cross correlation. With their approach the authors achieve a mean tracking error of 0.72mm and a standard deviation of 1.25mm and were able to show the real-time applicability of their approach.

With the advent of DL based methods, the manual definition of the previously outlined features becomes obsolete. At the same time, however, the demand for sufficient data from which these algorithms automatically learn relevant features, has immensely increased. A comprehensive list of algorithms used for breast, liver and thyroid US image classification can be found in [43]. Common network architectures employed in the classification approaches are VGGNet [44] and GoogLeNet [45, 46], while other approaches have also made use of unsupervised approaches such Boltzmann Machines [47] or Autoencoders [48, 49].

³<https://clust.ethz.ch/>, accessed: 17.02.2020

A Standard approach for many image segmentation task has become the U-Net proposed by Ronneberger et al. [50]⁴. The network comprises of an encoder and decoder. In the encoder the image is passed through the different layers and gradually reduced to a low dimensional feature space. Based on the encoder's low dimensional feature representation, the decoder gradually constructs the image segmentation mask, increasing in size by each layer. Network layers of the same level between the encoder and decoder are connected (skip connections) resulting in an exchange of information on the different compression levels.

Milletari et al. [51] propose an approach based on CNNs combined with Hough-voting to segment US scans from deep brain regions. Another approach for medical image segmentation by the same authors presented in [52], where the popular U-Net structure [50] is extended to 3D.

2.3.2 Extracorporeal Robotic Ultrasound

Robotic US systems for extracorporeal US probe guidance have been a subject of research for more than two decades. Well-cited examples include [53–55]. A collection of the various robotic systems for US can be found in [56] and [57]. [58] summarises important technologies and techniques to enable robotic US scanning and visual servoing. Research work includes both systems for manual teleoperation often integrating force feedback [54] as well as the creation of autonomous systems e.g. [59]. A significant portion of the works on autonomous robotic US systems has focused on visual servoing, which means steering an US probe to track key features (e.g. a section of an organ structure) in the ultrasonic image, subjected to disturbance such as breathing or heart beat.

One of the first works in this area has been published as [60] in which the authors present a image-based control scheme to support the surgeon during the scan of the carotid artery employing the Star Algorithm for detection and a subsequent Kalman filter for temporal tracking of a selected image feature. Others have explored automated tool tracking [61, 62] and robotic tool guidance [63, 64] thereof as well as tracking tumours [65–68] and multi-planar views [69–73] e.g. by matching a desired body cross section. With the uprise of modern probe designs extensions these methods were also extended to 3D US signals [74, 75]. To account for naturally occurring deformations and patient movements, several works have suggested methods for non-rigid tracking [76–79] and motion compensation [80, 81].

⁴Cited over 70.000 times as of 18/10/2023 according to Google Scholar (<https://scholar.google.co.uk/>)

A promising approach for visual servoing schemes is to integrate additional imaging modes such as pre-operative images to improve robotic navigation. The authors of [82, 83] propose and employ visual servoing schemes based on deformable registration. The applied registration scheme, originally outlined in [84], considers calculating the transformation matrix that maximises the normalised cross correlation of intensities between a initial and a current US frame. The initial approach in [82], implements an impedance controller which receives as input the position error calculated from the images as well as the desired contact force. Later work in [83] extends the approach to the multi-modal case. Based on a pre-operative CT scan, a desired needle path is planned and subsequently registered to a robotic US sweep. During the insertion of a needle the robot continuously adapts its position to account for target anatomy movements and and needle guide alignment, employing a hybrid force position control scheme (5-DOF position controlled, 1-DOF force controlled).

Further research work described in [85] proposes a force-based control scheme for the automatic scanning of the abdominal aorta. Prior to the scan they perform a registration between robot and patient via an external RGB-D camera. A pre-operative MRI-scan is subsequently fit to the registered point cloud of the patient and used for path planning. During scanning the authors integrate an US confidence map to improve the scan quality. [86] employ the same system setup for autonomous path planning and execution reporting up to 0.97mm accuracy with an online update of the registration. Further work from [87] deals with the problem of tissue deformation.

A system for extracorporeal US scanning of vessels is described in [88]. The outline of the vessel is detected via a U-Net-based image segmentation. The resulting 3D point cloud from the segmentation masks are buffered and subsequently fed into an optimisation routine to find the best match for the 3D orientation of vessel center line. Finally, the updated center line is then used to reorient the probe optimally towards the vessel and navigate along it.

The cross-national EU-funded MURAB project, running from 2016 to 2020 followed the goal of providing automated breast biopsies based on MRI-scans and robotic US scans⁵. The project has developed several methods to enable autonomous US scans of the breast including deformation tracking [89, 90] and co-registration [91]. This also included a robotic platform and approach to perform autonomous 3D US breast scans based on pre-operative MRI scans [92, 93]. Further work on a spinal navigation platform using a robotically controlled US probe and pre-operative CT and MRI is described in [94].

⁵<https://www.murabproject.eu/>, accessed on 02/10/2023

Overall, the work in extracorporeal US has matured substantially over the past 20 years. While initially a plethora of methods for visual servoing schemes for tool and anatomical feature tracking were devised, more recent work has focused on multimodal approaches. For guidance these systems mainly employ serial manipulators and rigid structures. Force control with the surface is simplified by the force sensors and 3D cameras.

2.3.3 Intracorporeal Robotic Imaging

Robotic systems employed in extracorporeal US such as the Kuka iiwa medical (Kuka AG, Augsburg, Germany) provide easy means to measure applied forces (e.g. joint torque sensors or force torque measurement units on the end-effector) and thus control them. This is not the case for surgical robotic systems that are tendon driven and do not allow precise measurement of the applied forces. Similar arguments can be made for the usage of external tracking methods, such as optical tracking or RGB-D cameras, which are not deployable for intracorporeal robotic settings, making the task of environment perception, reconstruction and localization for autonomous navigation significantly more difficult. Equivalently, the employment of registration algorithms may become quite more challenging than for the external case, since Robotic Intracorporeal Ultrasound (RICUS) deals with tissue that is highly flexible and generally only loosely constraint tissue. Visual perception inside the abdominal cavity is usually limited to a stereo endoscopic camera and even tracking methods such as Electromagnetic (EM) tracking may be disturbed by the presence of the metallic instruments.

Clinical Standard

Although not widely used across disciplines, robotic US has become a standard means to perform some common procedures such as partial nephrectomy (partial removal of the kidney e.g. in case of a tumour). By scanning the probe over the kidney, the surgeon is able to visualise the tumour (also referred to as mass) and mark the margin around the kidney via electrosurgery (see Figure 2.7). Marking the line helps the surgeon to resect at a safe margin around the tumour. Other surgical disciplines, such as thoracic or colorectal surgery have reported only very sporadic use of US [11, 12, 95]

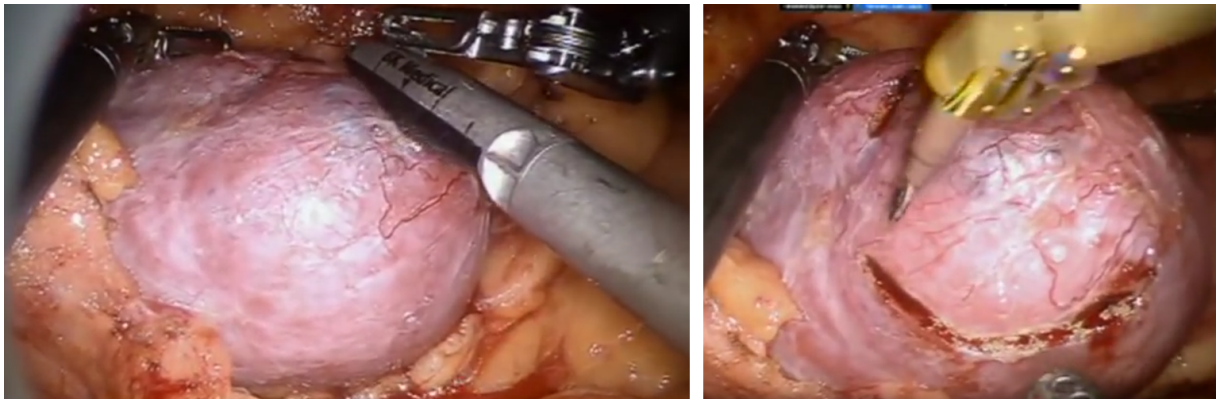


FIGURE 2.7: **Left:** Ultrasound scan of a kidney tumour. **Right:** Tumour margin marking on the kidney surface (© 2019 Swedish Hospital, Seattle, WA, USA)

Probe Design and Integration

Commercially only very few dedicated probes for intraoperative robotic US are available. Robotic US probes differ from conventional laparoscopic probes by including a small fin to be picked up by the robotic instruments [7] or by being fully integrated into a robotic instrument as presented in [96] (not commercially available). The first commercially available robotic US probe was released by Hitachi Aloka Medical (Wallingford, CT, USA) and reported to be used during thoracoscopy as early as 2004 [97, 98]. Whereas the probe itself is still offered as a neurosurgical probe, its usage as a robotic drop-in probe with the appropriate fins does not seem to be marketed anymore.

Currently, there are three probes specifically designed as robotic pick-up devices by two manufacturing companies: BK Medical (Peabody, MA, USA) and Hitachi (Hitachi Healthcare Americas (HHA), Twinsburg, OH, USA)⁶. Hitachi offers two linear array probes (model L51K and LK42K), with small footprint (13mm) and relatively higher frequency (up to 15MHz) and a second one with a significantly larger footprint (26mm) and slightly lower frequency (up to 12MHz) respectively. BK Medical offers a linear curved probe that has a comparable parameters as the LK42K by Hitachi. All available data about the different probes is summed up in Table 2.3. Two common probe by Hitachi and BK medical are shown in Figure 2.8

Additionally a variety of laparoscopic probes exist, most with a slightly lower frequency than robotic probes (up to 10MHz). Quite commonly, laparoscopic probes are also used

⁶Hitachi Healthcare Americas is also formerly known as Hitachi Aloka Medical America Inc. or short Hitachi Aloka

TABLE 2.3: Technical specifications of the different robotic drop-in probes available

Model	Manufacturer	Array	Footprint (mm)	Frequency Range (MHz)	Still marketed
UST-533	Hitachi Aloka	Linear	15	13 - 4	No
L43K	Hitachi Aloka	Linear	26	12 - 2	Yes
L51K	Hitachi Aloka	Linear	13	15 - 3	Yes
X12C4	BK Medical	Linear curved	33.2	12 - 4	Yes



FIGURE 2.8: **Left:** BK Medical X12C4 robotic drop-in Probe (© 2019 BK Medical). **Right:** Hitachi Aloka L43K robotic drop-in probe (© 2015 Hitachi Aloka Medical America, Inc.)

during RAMIS, however, these are manually controlled rather than picked up and manipulated by the robotic instruments.

The literature mentions that the pick-up interfaces in commercial devices do not guarantee a repeatable grasp of the pick-up probe by the robotic tool [7]. This is, however, needed in order to result in a fixed known transformation between robot and probe. Note that this is not the case for probes directly integrated into a robotic tool such as in [96, 99]. To fix this shortcoming, the authors describe an interface design including a custom mechanical interface in which the Da Vinci ProGraspTM tool can engage into in a reproducible way to ensure a fixed mathematical transformation between tool tip and image. An updated version is presented in [100]. A second option for this issue is to integrate visual or electromagnetic tracking to provide external positional tracking of the probe. [30] present a common medical grade grasping clip for their Aloka UST-533 probe (see Table 2.3) as well as a visual tool marker for their US probe. Lastly, a third option is to constrain the probe to the tissue. The designed mechanism presented in [101] and medically assessed

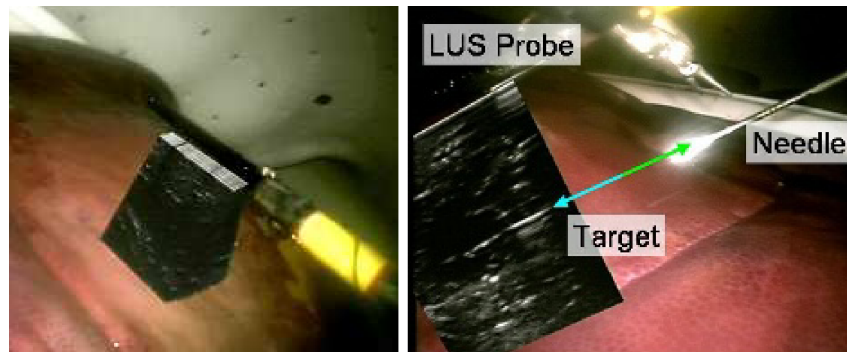


FIGURE 2.9: Da Vinci Canvas concept presented in [4]. **Left:** US image overlay (left) in the surgical video stream. **Right:** Needle feature present in the US image. Image from [4].

in [102] constrains one end of probe to a rail that is pneumatically attached to the tissue surface.

Registration and Visualisation

Enhanced visualisation and a better integration of robotic US into the robotic control console, play a vital role in promoting the benefits of US imaging. A crucial technology to enable visualisation is spatial tracking of the US probe in the coordinate frame of the image (camera coordinate frame). This usually involves a dedicated registration routine that determines the transformation between a spatially tracked position (e.g. instrument tip via robot kinematics) and the camera coordinate frame. For that matter, [4] presents an approach for merging the US image stream onto the instrument visual in the laparoscopic image, calling their system Da Vinci Canvas (see Figure 2.9). Prior to their experiments, they perform hand-eye calibration between instrument arms and camera image using an optically tracked checkerboard. Additionally, [103] suggests the use of custom designed markers to register and visually track the probe in space, achieving an error of $4.4 \pm 3.3mm$ to allow for an overlay of the US image with the laparoscopic camera image. Work in [104] compares three different approaches for probe tracking and registration: robot kinematics, electromagnetic tracking and visual marker on the instrument (also presented in [105]), concluding that the kinematics of the robot's leads to the most accurate results with an average error of $3.2mm$. Electromagnetic tracking on the other hand is assumed to be disturbed by the presence of the metallic instruments close to the tracking probe.

Autonomy in Robotic Intracorporeal Ultrasound

Moving an US device alongside or via the manipulation of surgical tools poses additional workload to the surgeon. An obvious suggestion may therefore be to let the robot automatically control the probe. In literature, different approaches to work towards this goal have been suggested. The approach described in [18] employs one of the robotic arms of the da Vinci to align the US image plane with the tip of the instrument, which is controlled by the surgeon. Another work suggests a control of the US probe via eye gaze and voice control [106]. The algorithm takes into account head movements that naturally occur during eye gaze to enhance the robustness of the control scheme. [107] describe a system for autonomous motion compensation during US scans. The system extracts the frequency of the motion signal based on the stereo endoscope image via stereo matching and optical flow. Subsequently, the main frequency components are extracted from the signal via Principle Component Analysis (PCA). During scanning they base their compensation on the main frequency component, while adjusting the phase based the visually estimated tissue motion signal. A similar motion compensation scheme is also suggested in [108].

Further Intraoperative Imaging in Robotically Assisted Minimally Invasive Surgery

As an alternative to robotic US, some interventions allow the usage of external or endocavitational probes. This particularly applies to prostatectomy (the full removal of the prostate e.g. in case of a tumour), where a TRUS probe may be used to scan the prostate and the surrounding areas [109, 110]. Literature also outlines approaches for 3D reconstruction of the prostate and the surrounding vessel during RAMIS and via TRUS e.g. [111], which involves a custom built robot that rotates the TRUS probe producing a series of 2D scans. In [112] and [113], the authors develop and evaluate a tool registration procedure that allows it to reference the instruments in the US image of a robotically controlled TRUS probe during prostatectomy. Therefore, they make use of the tissue air boundary of the prostate to register the instrument on different points along the prostate. In their final experiment they achieve a target registration error (TRE) below $5mm$ in different tissue materials. Their approach has been extended into an augmented reality system outlined in [114]. Recently, [31] presented an alternative approach to TRUS that uses an external US probe to produce a transperineal view on the prostate. With their

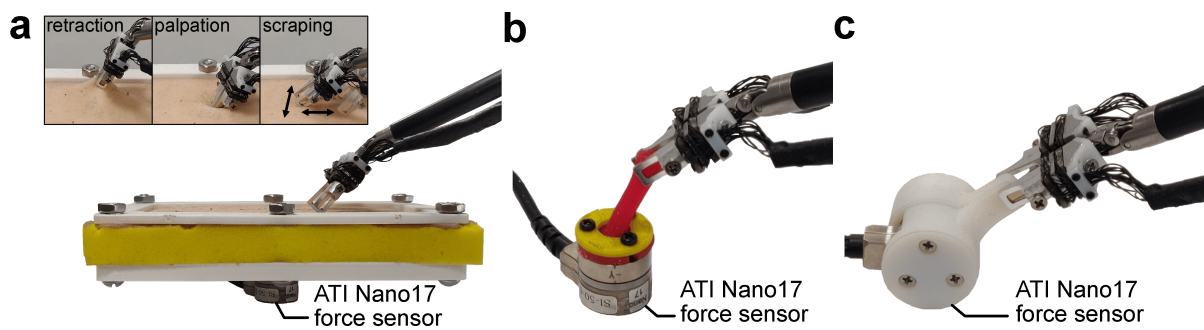


FIGURE 2.10: Force sensor suggested in [5]. Image from [5].

described registration mechanism they are capable of tracking the surgical instruments with a registration error of $0.84mm$.

Force Estimation and Control

Force measurement and control are further relevant areas for an autonomous probe guidance as they provide an essential mean to validate the contact with the tissue boundary and estimate the magnitude of its deformation. Both are quite large research areas in the surgical robotics community, particularly in the light of haptic feedback [18] and palpation [26, 115–117]. Approaches may be classified into two groups depending on if they add additional sensors to the system or make use of existing sensors (e.g. joint torques) to estimate the forces algorithmically.

Force sensing in surgical robotics has been an active area of research for over a decade e.g. [115]. Integrating force sensing into a surgical robotic system poses several challenges such as sensor miniaturisation and placement. Various attempts were made to integrate sensors at various locations on the manipulator such as the tip of an instrument [118] or inside the trocar tube [119]. More recently [5] presented a force sensor design for integration into the dVRK that is attached as a prolonged tip of a Large Needle Driver instrument. While generally small in size, it still significantly bulks up the instrument setup (see Figure 2.10).

With the uprise of DL, approaches have appeared in literature that estimate the force field of a surgical scene based on the visual information recorded by four video cameras. An approach combining a Variational Auto-Encoder (VAE) with a Long Short-Term Memory (LSTM) is described in [120] and extended in [121]. However, practical considerations on how four cameras are meant to be placed in the abdominal cavity before or during

surgery remain unmentioned. Similarly, [122, 123] have explored multimodal neural network based force estimation from stereo image and robotic state data, showing that the multimodal approach provides significantly better estimates compared to a purely visual input data. The neural network, running at $60Hz$, is able to provide good force feedback in a teleoperation setting, despite the frequent induction of oscillatory artifacts.

In recent years, the surgical robotics community has come up with several approaches to estimate the forces on the end-effector based on the measured motor torque measurement in combination with an adequate dynamics model of the robot. The challenges in coming up with an adequate description are the strong non-linear effects of friction due to the pulley-tendon mechanism driving the manipulator. The first source to present a force estimation based on a dynamical model for the Da Vinci surgical system has been presented in [124]. The applied forces in their experiments are fairly low ranging only between $-0.8N$ and $+1.5N$. The predictions of their model result in a normalised Root Mean Square Error (RMSE)⁷ of less than 3.5%. [1] extends the previous work from [124] by calculating optimal excitation trajectories, resulting in an improved estimation of the dynamics parameter. [125] performed further experiments with the same approach using a force torque sensor and a custom made coupling device that can be grasped by the robot's instruments and the application of more realistic forces ranging between $+10N$ and $-5N$. In this setting, the paper reports normalised RMSE of less than 9% between estimated and sensed force. Further work has already employed these estimated forces to perform collaborative impedance control [126]. Recently, [127] further adapted and improved the estimation of the da Vinci's dynamical parameters originally presented in [1] by using convex optimisation and enhanced modeling of the robot. All of the three papers working on this approach apply non-causal filtering, restricting their direct application for real time. Filtering in the approaches is mainly applied to smoothen the joint velocity derivatives and therefore result in more steady estimations of the joint accelerations.

Similarly, more recent works have looked at neural networks to directly learn the inverse dynamics of the system [128, 129]. A crucial aspect in this is the creation of a holistic data set that cover as much of the robotic configuration space as possible to ensure a generalised force estimation regardless of the the robotic pose.

⁷RMSE were normalised with the difference between maximal and minimal force

2.4 Robotically Guided Tissue Treatment

Goal of a surgical intervention is usually the treatment of diseased tissue in the body to prevent further inflammation or spreading of a disease or tumour. Hereby, a main distinction can be made between tissue resection and ablation. In resection, a piece of tissues is cut out and extracted from the body. In many cases this signifies a subsequent reconstruction of the surgical site e.g. performing anastomosis (reattachment) of the two bowel segments on each side of the cut. In tissue ablation on the contrary, no tissue is extracted from the body. In this either extremely high or extremely low temperatures are usually employed to denature the tissue. This method can be particularly suitable for tumours in vital organs in which a tissue extraction is a less favourable option e.g. in the case of large or late stage liver tumours or metastases [130].

Based on the initial analysis of both resection and ablation techniques (see Subsection 2.4.1 are analysed in an robotically automated context (Subsection 2.4.2 for resection and Subsection 2.4.3 for ablation) with the goal of identifying the right technology and application.

2.4.1 Clinical Tools and Physical Mechanisms

The following sections will first outline common resection and ablation techniques, organised by their primary physical principles. Note that this means that tools such as MWA or RFA, which sometimes are also referred to as thermal ablation methods, are categorised under electromagnetic methods, as the primary source is electromagnetic with secondary thermal effects on the tissue. Furthermore, the requirements may vary depending on the application.

Mechanical

Arguably the simplest method for resection is directly cut tissue via a scalpel, scissors or using other mechanical methods such as high pressure waterjets [131]. A major disadvantage of tools can be their lack of providing hemostasis, the control of bleedings. This is particularly crucial when operating on highly perfused internal organs such as the liver, lung or kidney. In particular scissors are useful when cutting a blood vessel that has previously been clamped and thus detached from the blood flow.

Thermal

To provide hemostasis, electrocautery can be used. Hereby, a tool is heated up electrically. Please note that the term electrocautery is sometime also used to falsely refer to electro-surgery. These, however, work on a different physical principle and will be treated later on in this section. Contrary to electrosurgical tools, electrocautery tools mainly coagulate tissue but do not support tissue resection. Therefore, they may serve as an additional tool to provide supplementary hemostasis for tools that do not include this functionality on their own such as scissors .

Tools employing thermal phenomenon are, however, very commonly used to ablate tissue, in particular CA. During CA repeated local tissue cooling and thawing, reaching temperatures as low as $-20^{\circ}C$ to $-40^{\circ}C$, will cause ice crystal formation within the tissue and eventual necrosis of the tissue. For this Liquid nitrogen and argon gas are commonly employed [132]. Possible complications include haemorrhage and ‘cryoshock’ syndrom [133].

Electromagnetic

Today, the most widely used technique and gold standard for tissue resection is ES that can provide hemostasis while also being tunable to cut through tissue by breaking the cell bondage. In this, a high frequency ($0.3 - 5MHz$) electric signal is induced into the tissue breaking the local cell structure apart and denaturising tissue, the latter being important for hemostasis. On the downside, inducing electricity into the patient, always comes at a risk of harming the patient including severe internal and external burns, electrocution or affecting active implants such as pace makers. ES may be applied in two different way, monopolar or bipolar. In monopolar eletroctrosurgery, the electricity runs between the two ends of the tool tip e.g. two sides of a forceps, while in monopolar ES the electricity flows through the patient to an electrode that is attached to the patient across a larger surface area.

Similar to ES, Radiofrequency Ablation and Microwave Ablation devices employ electromagnetic frequencies in the range of $300-500kHz$ and $900-2,450MHz$ respectively for local ablation of tissue [133]. Therefore, the target region is accessed via an inserted needle. By inducing the electromagnetic signal into the tissues, the tissue heats up and is finally destroyed via coagulative necrosis. In MWA, the frequency is tuned to align with natural frequency of water causing the water molecules in the tissue to heat up as

the electromagnetic field rapidly changes direction [133], resulting in a lower complication rate of compared to RFA and CA [134]. For RFA charring and uneven ablation are also reported to be potential issues [133].

During its upbringing, laparoscopic laser tools were a commonly used tool [135, 136] before ES became fully established as the means of choice for tissue resection. Laser systems may be driven externally and the laser beam transmitted via a flexible small diameter fibre, usually around 0.2–0.8mm in diameter [137], allowing, in theory, their miniaturization and integration into robotic tools [138].

For ablation the laser light may be delivered to target locations via a needle or catheter. Full ablation of a tumour may be realised via several incisions through which small fibres transmit the laser onto the target region causing localised heating of the tissue and eventual cell death. Alternatively, a single larger incision and fibre may also be used [139].

Ultrasonic

The recent years have seen an uprise in the use of ultrasonic cutting tools. Hereby, Ultrasonic energy is locally induced into the tissue causing a detachment and denaturation similar to electrosurgery. In robotic surgery, this was previously realised via an unwristed instrument containing a bladed rod which is excited by an ultrasonic transducer sitting at the top of the instrument outside the patient. This was mainly done due to the difficulty of miniaturising the ultrasonic transducer to fit at the tip of the instrument. As these instruments don't induce any electricity, they are the method of choice for patients with pace makers.

Particularly in liver surgery a further tool that is commonly used for dissection as well as ablation is CUSA. The device also uses US but employs a needle tip and liquid medium to cause cavitation at the tissue surface that in turn dissects, however, does not coagulate tissue, for this purpose they may be coupled with a coagulation technique such as ES. By tuning the frequency, CUSA can be set to be selective towards specific tissues and reduce the risk of puncturing blood vessel [134]. For ablation, rather than touching the tissue surface with the CUSA device, the needle of the instrument is inserted into the tissue to directly target the ablation region with the ultrasonic energy [134].

A further technology for ablation relying on US is High Intensity Focused Ultrasound (HIFUS). It employs a focused US beam that is directly induced into the tissue with waves converging onto the target region. This means that as opposed to most other

TABLE 2.4: Comparison of different ablation techniques, High Intensity Focused Ultrasound (HIFUS)), Cryoablation (CA)), Radiofrequency Ablation (RFA), Microwave Ablation (MWA) and Cavitational Ultrasonic Surgical Aspiration (CUSA). *Likely physically possible, however, no records yet of working miniaturised research or commercial prototypes

Technology	Energy Source	Miniaturisable	Incision Required	Further Remarks
HIFUS [140, 141]	US	Yes	No	Obstructed by air or hard tissues
CA [133]	Thermal	No	Yes	Can lead to 'cryoshock'
RFA [133, 134]	Electromagnetic	(Yes)*	Yes	Potential Charing
MWA [133]	Electromagnetic	(Yes)*	Yes	Ideal for small target area such as blood vessels
CUSA [134]	US cavitation	(Yes)*	Yes	Not yet available for robotic wristed instrument (only laparoscopically)
Laser [139]	Electromagnetic	Yes	Yes	Subsurface ablation via heat diffusion

ablation techniques, HIFUS can be applied completely remotely, without the need of accessing the target location via a needle. HIFUS transducer can be manufactured in two types, depending on how many elements they include. The first type, referred to as single element transducers, is driven by a single element that connects to a lens (usually hyperbolic) focussing the beam. This means that the focus of the beam is relatively fixed. The second type includes multi-element transducers, usually arranged on a hyperbolic lens. Since all elements can be driven individually, the focus of the beam is highly tuneable. A further advantage of HIFUS probes is that they can directly integrate an imaging probe placed at the center of the lens, allowing a direct and spatially registered observation of the target region and its treatment [142].

All identified techniques for tissue resection and ablation are summarised in Tables 2.5 and 2.4 respectively.

TABLE 2.5: Comparison of different resection techniques. *Likely physically possible, however, no records yet of working miniaturised research or commercial prototypes

Technology	Energy Source	Hemo-stasis	Miniaturisable	Further Remarks
Scissors	Mechanical	No	Yes	Most suited for cutting clamped vessels or less perfused structures
Waterjet [131]	Mechanical	No	(Yes)*	-
ES	Electrical	Yes	Yes	Potential risk of electrocution and severe burns
US [143]	US	Yes	(Yes)*	Miniaturization theoretically possible yet not fully realised
CUSA [143]	US cavitation	No	(Yes)*	Selective cutting possible, sparing blood vessels or in combination with ES for coagulation
Laser [135]	Electromagnetic	Yes	Yes	Provides only superficial ablation of tissue

2.4.2 Robotic Resection

Manipulating and removing tissues has been a core part of the research around autonomous surgery. In this, several approaches have been proposed to enable robotically automated cutting and resection of tissues e.g. for tumour removal.

Work by [144] proposes a deep Reinforcement Learning (RL) framework to learn tissue tensioning for automated tissue cutting. By training the RL agent on a finite difference simulation of a stretchable sheet, the approach achieves improved accuracy in cutting various patterns out of the sheet, when compared to fixed or analytically calculated tensioning.

The authors of [8] propose a set of three pick-up tools for the dissection of tumours. The first tool enables the palpation of the tissue surface, detecting harder elements right below the surface. The second tool with an integrated scalpel is then used to cut open the tissue surface to reveal a piece of debris that is picked up. The resulting wound is then sealed via the third tool that integrates a needle and releases surgical glue. Out of ten total runs, the authors report five failures due to different incorrect estimates or executed actions. On a practical level, it remains unclear how the tumour would be precisely located and

referenced. It is further questionable to what degree the application of surgical glue accounts for the complexity encountered during a real surgery.

Recently, [145] demonstrated fully autonomous large bowel anastomosis. While the results are convincing, the system heavily relies on previously injected optical markers containing toxic ICG and Cyanoacrylate. Furthermore, it is unclear how the results, performed on bowel tissue, could be used for improved tumour resection as they lie below the tissue surface. Work by the same group has further focused on autonomous electrosurgery, enabling linear cuts on planar surfaces [146, 147]. Similar to the group's previous work in [145], the system relies on injected markers and is built on a proprietary platform rather than a full surgical robotic system.

More rarely, approaches have also integrated imaging techniques, in particular US to guide tissue cutting. [30] demonstrates autonomous cutting on a planar phantom enabled by a parallel US scan. Custom visual markers are used to track the US probe as well as a high velocity waterjet to perform tissue cutting based on the US image. In a bench top trial using a custom designed PVA cryogel phantom, the system is able to dissect a modeled tumour at a margin with mean difference of 0.77mm over multiple experiment runs (see Figure 2.11).

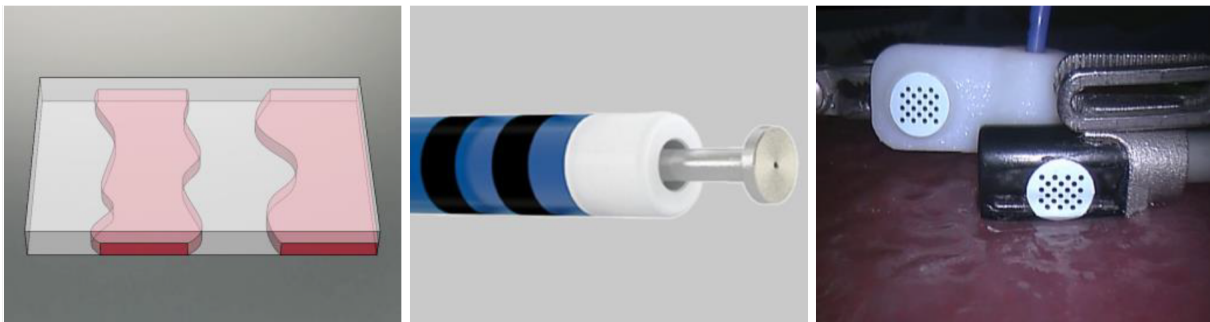


FIGURE 2.11: System for autonomous US-guided tissue ablation described in [6]. **Left:** Outline of the planar phantom structure with curved lines. **Center:** Waterjet tool for tissue cutting. **Right:** Optical markers used on US probe and cutting tool

In terms of autonomous cutting, a major focus has been on learning methods or on tool development to enable automated cutting. Most of these have involved an endoscopic camera feed or a specialised camera setup to enable autonomy. Only a single work could be linked with using in corporeal US imaging as a guiding source. Further investigation would be needed to see its application under more complex non-planar surface geometries, without visual instrument tracking and with a ground truth referencing such as EM or IR tracking.

2.4.3 Robotic Ablation

Robotic ablation devices have been the focus of research for several decades. There is a multitude of systems for robotic needle placement including CT or MRI guidance with further systems being commercialised at the moment such as Micromate (Interventional Systems, Kitzbühel, Austria). Looking at the clinical motivation a comparison presented in [148] found improved accuracy of robotic systems compared to hand-held systems for out-of plane targeting, while also finding a significant increase in procedure for robotically assisted interventions. Similar results were found in the meta-study presented in [149] find robotic systems to have superior accuracy to stereotactic systems.

Work presented in [130] assesses a concept for a robotically assisted RFA system for liver surgery that uses pre-operative imaging and an stereo-tracking system to enable the robot to insert the needle. The systems efficacy is shown in an animal study showing a 13.43mm ablation on the liver. No further quantitative information is provided. Similarly, [150] present a 4-DOF robotic system for laser ablation of a liver tumour using MRI guidance. The system is conditionally MRI compatible meaning it does not affect the MRI imaging. The results suggest a target error of 5mm and a time reducing compared to manual insertion.

There is also a plethora of robotic systems employing extracorporeal HIFUS system. As opposed to needle guidance systems they operate completely remotely. The review [142] mentions ablation systems for tumours of varying types, locations and pathologies including Pancreas, Breast, Brain, Lungs, Liver, as well as urological and gynecological applications. While the authors mention laparoscopic HIFUS, none of the systems they outline implements image-guided, robotically assisted laparoscopic HIFUS ablation.

While HIFUS is already commonly used in medical practice to treat specific diseased tissue such as liver or kidney tumours [140], it has been a very active area of research in the last decade. A particular interest lies in the combination of HIFUS with robotic guidance [151, 152] that can use use to precisely place and orient the probe. Ablation trajectories can further ensure that the target location is reached from different angles, further sparing the surrounding tissues. Further research effort has been put into the development of phantoms for device testing Coupling [153] and the assessment and improvement of coupling quality [154, 155] between probe and tissue. Current commercialisation efforts of robotic HIFUS devices such as HistoSonics (HistoSonics, Inc., Plymouth, MN, USA) and Soundsafe Care (Soundsafe Care SRL, Milan, Italy) further underline the importance of this technology. Another recent trend is the miniaturisation of HIFUS probes into

minimally invasive devices [141, 156–158]. A key difference to extracorporeal devices is that minimally invasive devices do not include imaging at the center of the lens due to the size constraints. In its inception, the miniaturisation of HIFUS devices allows a more localised treatment of tumours rather than needing to penetrate the abdominal and layers of fat tissue that can further stretch across the target regions and dampen the ultrasonic waves induced [141]. Recent research efforts have also included the development of robotic gamma-ray drop-in probes that can be used for targeted tumour treatment [159].

Further literature presents a system and approach for brain tumour ablation on a RAVEN II surgical robot [160]. The setup includes a custom built stereo camera system, a planar simulated tumour and a suction device, emulating an ablation tool. The stereo camera is used to both detect the tumour in a high contrast bench top setting as well as track the location of the robotically guided dummy ablation device. The system automatically calculates two ablation paths [161] that the surgeon has to select from. The eventual control error of the system was found to be around $0.318mm$ RMSE, comparing robot kinematics with the custom built stereo vision system. No further referencing to a ground truth tracking system such as IR tracking has been reported.

Research outlined in [156] employs a previously presented continuum robot [162] to carry a miniature HIFUS probe (ceramic element diameter of $20.15mm$). In their extended abstract, they describe their setup including the interfacing with the robot, the addition of a coupling balloon along with qualitative results. Ex-vivo experiments on chicken breast reveal a manually measured lesion of $6 \times 7mm$ at $3mm$ below the tissue surface.

A main and critical distinction needs to be made whether the method requires inserting a tool e.g. a needle into the tissue to reach the target region. The requirement for a needle injection into the tumour bears the risk of harming additional tissue and further spread out cancerous cells outside the tumour region [141]. Concerning the integration into a robotic setup a major point to consider is the possibility to miniaturise ablation devices. While laparoscopic systems exist for CA [163], RFA [164] and MWA [165], it may not be possible to fully miniaturise these systems.

2.5 Summary

This chapter presented the state of the art around robotic and autonomous US guidance. It further presented common tissue resection and ablation techniques and their integration into robotic and autonomous systems.

Comparing the area of intracorporeal US guidance with the previously analysed area of extracorporeal US, several observations can be made. While the latter has matured over the past 20 years, few applications of intracorporeal US guidance have so far been investigated, in particular not in the context of autonomy. A major difference to extracorporeal US are the employed robotic systems, usually compliant and thus less precise, as well as the restricted workspace, limiting the application of sensors. Both of these aspects need further consideration in broader research context to allow translating some of the research of extracorporeal over to intracorporeal robotic US scanning. Additionally, due to the multiarm structure of surgical robotic systems, a direct integration and further usage of the acquired US information into the surgical workflow should be explored.

These differences between intracorporeal and extracorporeal US, provide sufficient reason to justify further investigation and extend research results from the more established area. While previous research in surgical robotics has touched upon autonomy and the outlined challenges in this context, further research is needed to investigate means to autonomously acquire anatomical information via intracorporeal US and further use that information to provide informed assistance to the surgeon. This includes, research to enable interaction of the US probe as well as further operated instruments. Equally important, navigation schemes have to be extended to allow robust planning and adaption of scanning paths based on the US image sequence.

Concerning tumour treatment and resection, few works have looked at a collaborative approach that combines intracorporeal US imaging to support the resection of tumours. Most approaches have rather explored learning methods to enable tissue cutting [144] or involved specialised equipment such as injected IR markers. In terms of resection the only notable work is [6] using US, relying on external optical markers for robot guidance. Similarly, robotically integrated ablation devices have been built but have not yet been employed in an automated or collaborative setting that involves further US image guidance.

Analysed in the context of robotic automation, specific tools were identified that could be used to investigate US enabled autonomy. The most suitable technologies for tissue resection in particular with respect to a robotic setting seem to be ES and US based cutting tools. These technologies are already widely used in laparoscopic surgery, provide good hemostasis and precise localised induction of energy into the tissue. The main challenge remaining with US cutting tools is the integration of this technology into a dexterous robotic tool, which is currently being pursued as part of an early stage commercialisation effort by Nami Surgical (Glasgow, UK). All remaining technologies either provide no

hemostasis (mechanical approaches), are not straight forward to miniaturise (CUSA) or provide only surface level tissue treatment (lasers).

For robotic tissue ablation, given the physical background as well as the identified literature works, it seems reasonable to conclude that HIFUS seems to be the most adequate technology to be integrated into a minimally invasive robotic setting. Firstly, it is easily miniaturisable and highly customisable to the specific application (e.g. ablation depth). Secondly, it is the only technology that does not require perforating the tissue surface, while still being able to reach deep inside the tissue. Lastly, it has not yet been thoroughly integrated and researched in a surgical robotic setting, making it a interesting area for US-guided automation.

Overall, there remain several open issues:

1. US-guided autonomy is a largely unexplored realm. Aside from autonomous US scanning, this includes enabling further surgical assistance and autonomous applications based on information acquired through intracorporeal US.
2. Most works on autonomous US scanning rely on visually tracking the US probe and further surgical tools rather than improving the kinematic measurements themselves [30].
3. There are very few works that have assessed the dVRK's accuracy in an autonomous context more rigorously using gold standard tracking techniques such as EM- or IR-tracking. The only notable work with this rigor is [100], it however is limited to US scanning alone and does not include further robotic arms and instruments that use the acquired information for further assistance.

Considering these findings, this work will explore three areas of increasing autonomy. Firstly, analagous to extracorporeal US autonomous methods for scanning and reconstructing anatomical structures are developed. This will constitute Level 2 autonomous function, performing the step of acquiring information before handing control back to the surgeon. Subsequently, assistive tissue resection based on autonomously acquired US information will be investigated, also constituting a level 2 functionality, however, in the much more complex setting of a two arm collaborative setup. Lastly, with the exploration of autonomous US-guided ablation, a level 3 functionality will be explored with goal of fully automating the tumour removal.

Chapter 3

Platform Development for Autonomous Surgery

This chapter outlines the preparatory work of developing an autonomous surgical platform, including an initial analysis as well as technical modifications, sensor calibration and spatial registration necessary before the subsequent chapters dive into more detail of further research around autonomous functionalities and their scientific evaluation.

3.1 Requirements

3.1.1 Ultrasurge Project Requirements

This PhD was part of the larger UK EPSRC funded research project Ultrasurge that started in 2018 and will run until 2024 and is a collaborative effort of the University of Glasgow, University of Edinburgh, University of Birmingham, University of Southampton and the University of Leeds. Furthermore, the project was advised by several industrial partners. The overall goal of this project is the holistic investigation of US and ultrasonic applications in surgery, ranging from dentistry and orthopedics to soft tissue surgery. This includes the scientific evaluation of US's effect on cell cultures and tissues as well as the development of new ultrasonic devices for the aforementioned medical disciplines as well as their integration into surgical robotic systems. Hereby, a particular focus was set on using the developed tools in an autonomous surgical setting, including the development of a robotic setup and algorithms to enable US-guided surgery. In terms of robotic platforms,

three options were considered: a serial robotic arm for hard tissue cutting, a surgical robotic platform, more specifically the dVRK, and, lastly, soft tentacle robots, with this work exclusively focussing on the dVRK. While initial efforts were set on developing a novel imaging probe by our project partners, it was decided to opt for commercially available solutions and put a stronger focus on the development of novel resection and ablation devices. As in many collaborative research projects, a major challenge was that these devices were in development in parallel with the robotic development. This meant that for the sake of efficiently completing the common endeavor, the project firstly resorted back to using dummy devices or substitute technologies that would allow an easy transition towards US devices once these were fully developed and ready for robotic integration.

3.1.2 Technical Requirements

Building a robotic platform for autonomous surgery included considering different requirements that needed to be fulfilled to allow the system to perform in an autonomous setting. Initially given were the architectural concept of two PSMs, one holding the US probe and another one operating a tool for dissecting or ablating tissues. This led to the definition of several requirements. that will be treated in upcoming sections.

Arm Co-Registration: The two robotic arms need to be able to reference one another in a common coordinate frame. This requirement is addressed in Section 3.3.2.

Hand-Eye Calibration: Information from the US image shall be directly relatable to the robotic base frame Section 3.3.3.

Ground truth reference: The system shall integrate means to accurately verify the systems performance in reaching specific goals. See Section 3.2.2 for details.

Modular Software Infrastructure: The system shall enable the easy integration of different software and sensor components. See Subsection 3.2.2 - *IR tracking* for details.

Modular Hardware Design: The system shall enable the easy integration of and switch over to different devices. See Subsection 3.2.1.

3.2 Robotic Infrastructure

In the following the robotic software and hardware infrastructure is explained in further detail.

3.2.1 Hardware Design

In order to adequately integrate the US probe and further US tools into the robotic setup two main options presented themselves. The first one being, the redesign of the entire instrument with inclusion of the respective tool or probe and the second one, being the design of an appropriately shaped pick-up interface. The main advantage of direct tool integration would allow a more slender design and more robust and reliable attachment. It would, however, have made changes to the tool tip difficult and would have meant the need to redesign the entire tool for a different element. Therefore, I decided to work on designing an appropriately shaped pick-up interfaces.



FIGURE 3.1: **Left:** da Vinci ProGrasp™. **Center:** da Vinci Fenestrated Bipolar Forceps (FBF). **Right:** da Vinci Large Needle Driver (LND). (© 2023 esutures.com)

As previously mentioned the project would not focus on building a custom robotic US probe but rather adapt an industrial probe. After researching US probe suitable for robotic surgery, a Philips L15-7io probe driven by an iU22 US machine (Philips, Amsterdam, NL) was chosen and integrated into the setup. In its original form the US probe is intended to be hand-held during open surgery. The imaging specifications of the US probe are identical to those used in commercially available surgical robotic US probes with a frequency range of $7 - 15\text{MHz}$ to make the results and conclusions directly transferable to conventional RICUS.

Therefore, the designs from [7], presenting a pick-up US probe, and [8, 26], presenting an exchangeable set of pick-up tools were assessed in further detail. Both works have

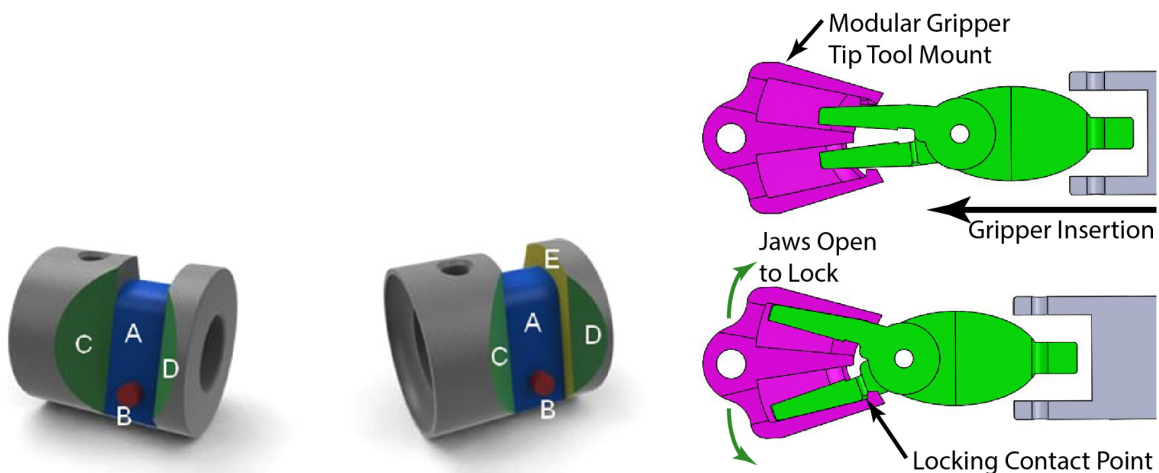


FIGURE 3.2: **Left:** Tool engagement mechanism for standard da Vinci ProGrasp Tool. Image and concept from [7]. **Right:** Tool engagement mechanism for standard da Vinci Large Needle Driver. Image and concept from [8]

integrated novel devices into their setup by designing them as pick-up tools that can be grasped by a robotic tool with an appropriate tool tip and stay in place via shape locking. The designs of [7] and [8] differ in the shape of their locking mechanisms. [8] uses a standard LND tool with relatively short (roughly 10mm) pin-like tips and a locking mechanism that relies on opening the instrument inside an enclosure, shape locking the tool tip within. Both concepts are depicted in Figure 3.2. [7] on the contrary uses a standard da Vinci ProGrasp Tool, with a longer (around 25mm), wider and fenestrated tool tip. All three tools are depicted in Figure 3.1. The tool engages with the pick-up interface by closing the instrument around a groove placed on the outside. An additional pin inside the groove is placed to fit inside the fenestrated tool tip of the instrument, providing full shape locking.

After the initial scoping, it was concluded that a big advantage of [7] is that it has a smaller footprint as it does not require a full enclosure. Furthermore, by employing a wider instrument tip it is able to provide improved support against moments at the tool tip. The in-depth assessment in [7] further confirmed good repeatability of the grasp. For this reason [7] was chosen to be further investigated. Rather than designing the pick-up interface around a ProGrasp tool it was designed around a similarly shaped Fenestrated Bipolar Forceps (FBF) tool. This tool essentially employs the same fenestrated tool tip as the ProGrasp, however, has slightly different kinematic mechanism at the tool tip making it slightly shorter.

As no CAD model of the US probe was available, the pick-up interface was iteratively

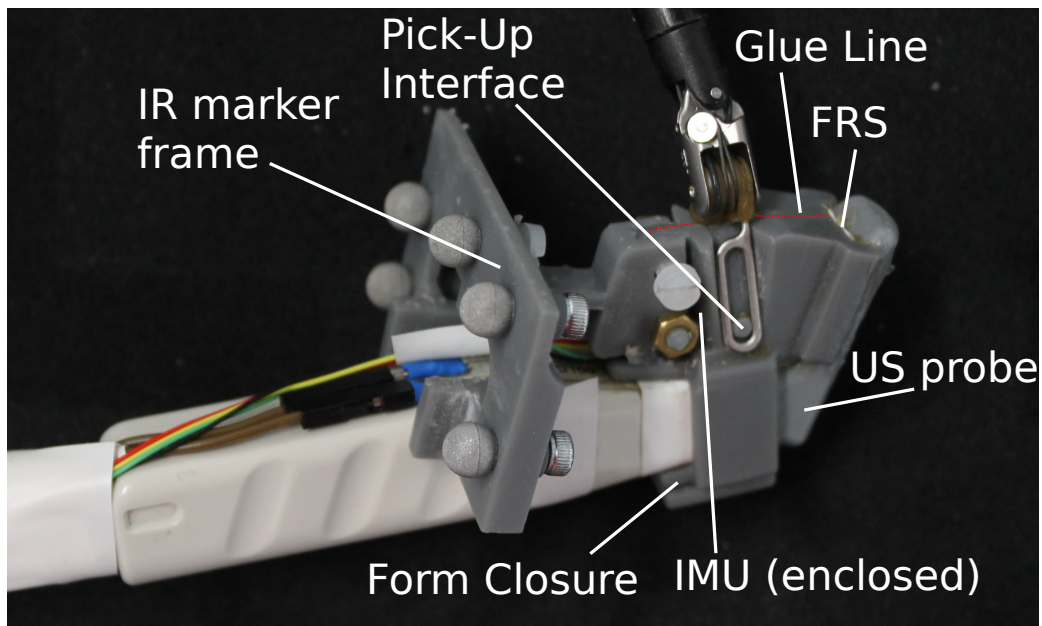


FIGURE 3.3: Robotic Pick-Up probe design including integrated sensors.

designed to fit on the probe. The probe and all further 3D printed tools were printed using a Formlab 3 SLA printer (Formlabs, Somerville, MA, USA) with Grey v4 or Clear v4 resin. The pick-up interface is locked in place around the tool handle via form closure. It is produced in two parts that engage at the back of the handle and are glued together in between the two grasping surfaces. Additionally an IR marker frame can be screwed on for external reference. See Figure 3.3 for a depiction of these different elements.

3.2.2 Software Infrastructure

Starting off from the dVRK as a base for further automation, the task at hand was to find a suitable software infrastructure that could support the addition of the various input signals defined from the beginning as well as future additions that might occur. Figure 3.4 shows the software structure of the developed system, including all interfaces used to exchange data along with their update frequencies. Each surgical use case explored within the upcoming chapters contains their separate main program routine that performs the inference and sends the robot control commands. Within this program, the most recent values for each data source are received via ROS and combined to ensure synchronicity between the signals. More details on each interface will be given in the following.

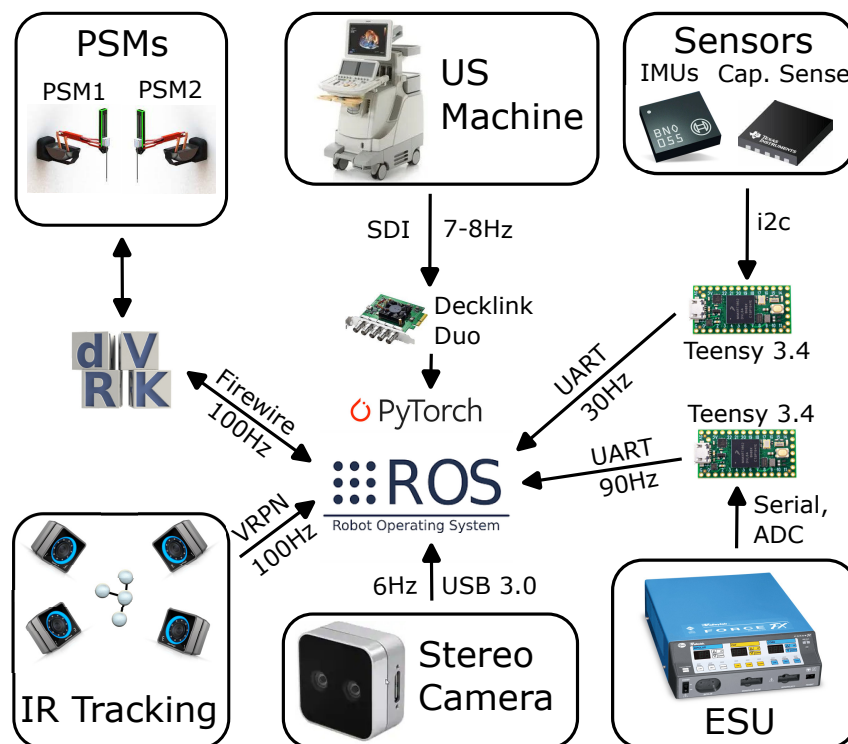


FIGURE 3.4: ROS-embedded system structure showing hardware and software components as well as their interfaces for data interchange.

PSMs

Since the dVRK integrates ROS support and is widely used within the surgical robotics research domain, it was natural to integrate any further devices within this framework. ROS acts as a middleware to exchange data between different nodes in a network. This means that the code for a project can be split up into a micro service architecture in which each node runs as a separate program and data is seamlessly interchanged via the network and defined messages. In order to realise this endeavour the main tasks were to integrate all further devices into the ROS framework. To keep the control of the robot independent of the computational load, the dVRK code was run on a separate PC and all other ROS nodes on a second PC. All ROS code is written in Python (version 2.7).

US machine

Starting with the US machine, the US signal feeds into a Decklink Duo Capture Card (Blackmagic Design Pty Ltd., Pout Melbourne, VIC, AUS) via SDI. To integrate the video stream into ROS employing the publicly available library `decklink_ros` by NEARLab

of Politecnico di Milano.¹ To enable image processing the software framework integrates PyTorch into a standalone ROS package.

Sensors

Lastly, an essential aspect was the integration of sensors to increase robotic perceptual capabilities. Initially, the subsystem was based on a BeagleBone Black (BeagleBoard.org Foundation, Rochester, MI, USA) for this purpose. The BeagleBone ran a Linux distribution and ROS to allow a direct integration into the network as a separate ROS node. This, however, came with the disadvantage of only having a single i2c line available that soon become too restrictive for the project, as there were at least four different sensor board that needed an i2c interface to be read. These included two IMUs, one for the US probe and one for the active, a capacitive sensor board for contact simulation and a pressure sensor for the HIFUS device. Therefore, the setup was transitioned to using a Teensy 3.6 (PJRC.COM LLC, Sherwood, OR, USA), which offers up to four i2c ports and 25 Analogue Digital Converter (ADC) signals. All signals from the Teensy are then fed via USB cable as Universal Asynchronous Receiver-Transmitter (UART) to the main computer running all ROS nodes. For this purpose, a custom UART message was devised that is read by a Python script and then published on corresponding ROS topics with added local time stamp.

ESU

ESU integration was accomplished via a custom built interface box that communicates with the device via serial. Further details of this will be explained in detail in Chapter 5.2.3.

Stereo Camera

Further integration of cameras was performed using standard protocols and publicly available ROS packages. Please see Subsection 5.2.2 in Chapter 5 for more details on the implementation.

¹available under: https://gitlab.com/Polimi-dVRK/decklink/decklink_ros, accessed on 03/10/2023

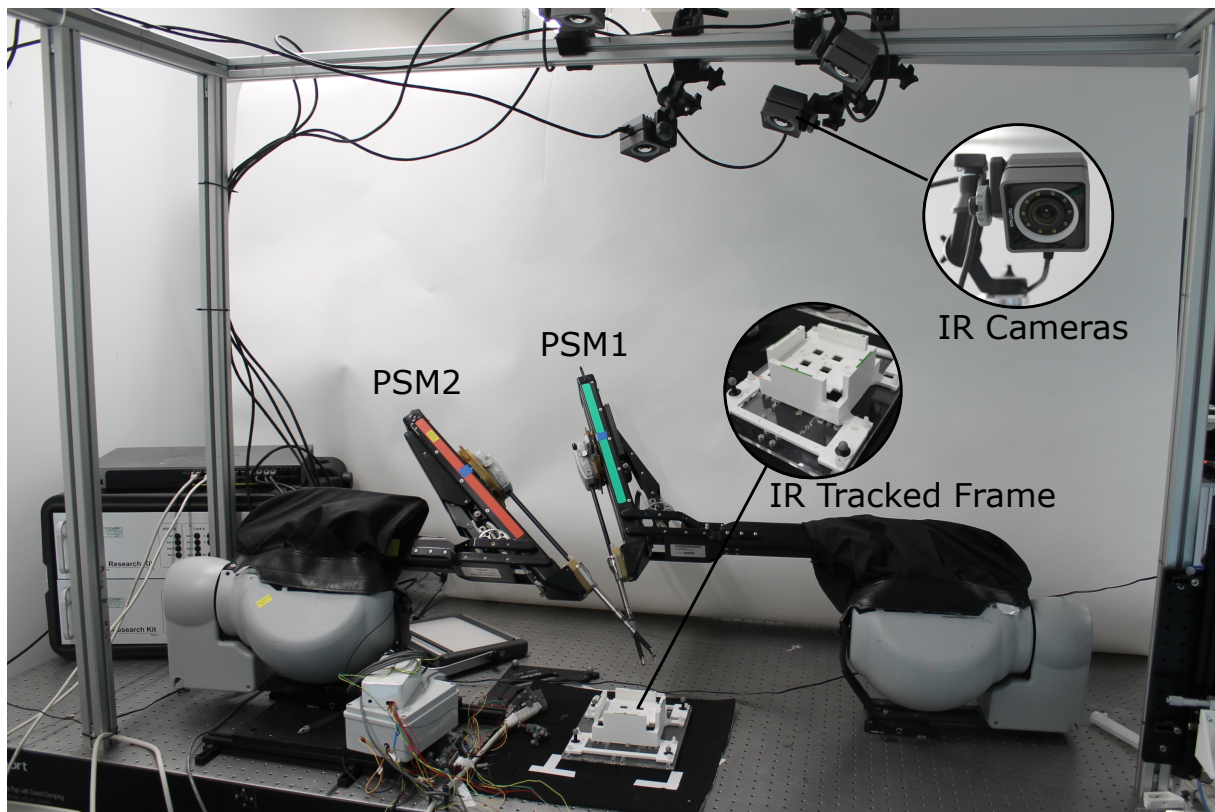


FIGURE 3.5: Benchtop setup used for experiments including the IR-tracking cameras and the tracked frame.

IR tracking

A crucial point in the scientific evaluation of autonomous systems is its accuracy to perform actions, normally carried out by human. While the human surgeon combines a plethora of sensory inputs in a complex manner, particularly sight and touch (predominantly in the case of open surgery), a technical system is far more limited. A particularly crucial aspect is referencing any image data that may arise from the laparoscope or an US probe to the robot's spatial reference frame. Only in this way is it possible to the feedback loop and let the robot perform actions based on features in the image. Additionally, the problem arises that a precise evaluation of the accuracy of a system requires a ground truth positioning system that allows precise tracking over the course of an experiment. While a relative quantification may be made relatively easily, it becomes far more complex to absolutely quantify the arising spatial error.

There are several methods which can be used to spatially track an object over time. Most commonly, EM, binocular and IR tracking are used. EM tracking has the big disadvantage that it is negatively affected by the presence of metal. This has also been

confirmed in [100] in the case of the da Vinci Robot. Binocular tracking on the contrary is quite restricted with respect to different viewpoints and, depending on the marker, a lot lower in accuracy than the other two methods. Finally, IR-tracking is very precise, however, may be negatively affected by other light sources emitting in the IR spectrum. Additionally, reflective surfaces in the visual field of the cameras may create noise. While IR markers, similar to markers for binocular tracking, require a lot more space than electromagnetic trackers, they can be made very precise and are thus ideal for evaluation the accuracy of the robotic setup in an image-guidance context and may further be used for image registration. It is for this reason that the setup was evaluated with an IR tracking system, giving a theoretical accuracy of below $0.1mm$. A similar setup has also been used in [100] for absolute global referencing. An IR tracking system works by employing several spatially calibrated cameras with different views on the scene. By emitting IR light outwards while filming in a similar spectrum, markers can be picked out as they are highly IR reflective. Using triangulation, the precise location of the tracker in space can be determined. By combining at least three markers, the spatial pose (position and orientation) of an object can be tracked over time. For the purpose of the robotic system, custom markers to fit onto the different devices and relevant objects were designed and 3D printed, allowing precise spatial referencing of the overall scene, setup and system. Figure 3.5 shows the robotic setup including the integration of IR tracking cameras.

3.3 Robot Calibration and Registration

3.3.1 Encoder Calibrations

Both robotic manipulators this work employs were calibrated using the methods provided by the dVRK software framework. As described in the dVRK wiki, the last four joints were fixated using the recommended 3D printed fixator. To ensure adequate levelling the robotic setup was placed on top of a floating table. To along the trocar tubes with the table the IR tracking system was employed. This made sure that the z -axis of the robot was normal to the table surface for both robots and thus parallel with the gravitational axis. This will become import in Chapter 4 when the system will be enhanced with attitude sensing. Furthermore, it ensured consistency between the frames of both robots. Additionally, the recently added routine to calibrate the third, prismatic joint via a web cam was run.

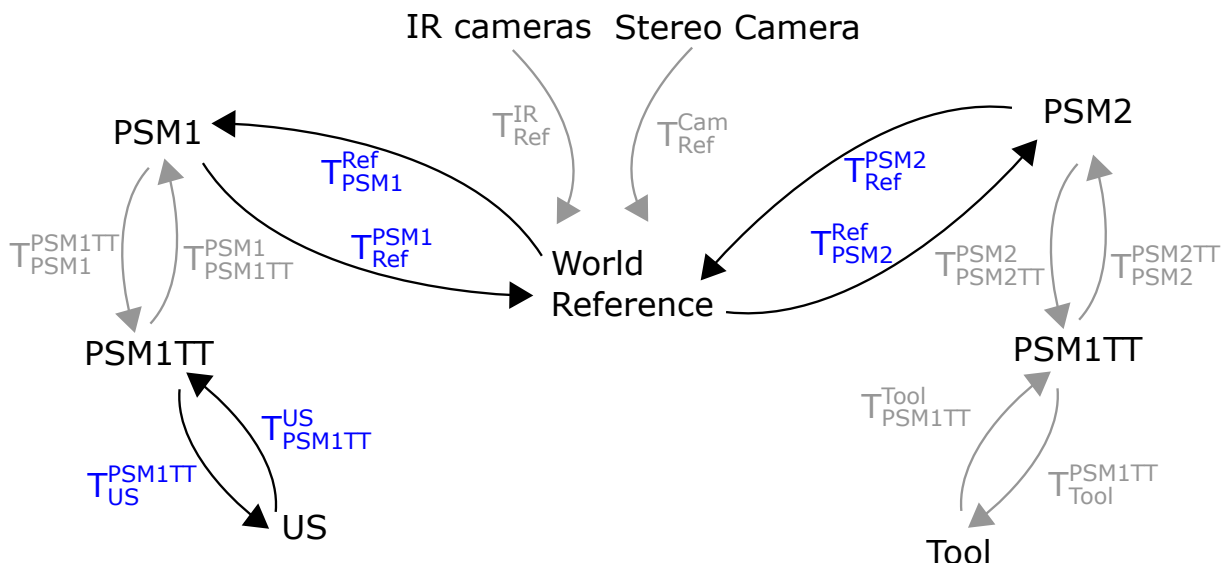


FIGURE 3.6: The different transformations obtained through calibration. Greyed out connections and transformations are either determined by design (e.g. PSM1TT to Tool) or measured (e.g. PSM1 to PSM1TT). More details on the stereo camera and its application can be found in Section 5.2.2.

3.3.2 Arm Co-Registration

Since the platform included two independently placeable robotic arms, it was of paramount importance to establish a common coordinate frame for the two arms to allow spatial referencing between them. Figure 3.6 shows the relation between the different transformations obtained via registration / calibration, in particular arm co-registration and the US hand-eye calibration outlined in the upcoming section.

Arm co-registration is a major challenge in collaborative applications on the dVRK platform. Normally, the PSMs sit on a patient cart that kinematically connects the two robots. With the recent introduction of the SUJ, these can be measured. However, since the resulting accuracy lies in the range of centimeters, the two arms had to be corregistered in a different manner.

Please note that this may not be necessary for more modern versions of the da Vinci, such as the Xi that possess more accurate setup joints that allow global referencing in sub-millimeter scales while being unloaded [166]. These, however, do not yet have an open-sourced API that allow their control, although the da Vinci S and Si are planned to be more widely integrated into the dVRK framework in the upcoming years and eventually replace the current dVRK, using the first-generation da Vinci robotic System.

To enable arm co-registration, spatial landmarks are touched with the robotic tool tips. The landmarks are equally spread around the target region with two landmarks on each side of the square frame that was holding the phantom (see Figure 5.11). Opposing spatial landmarks were aligned with \mathbf{x}_{REF} and \mathbf{y}_{REF} and consequently used to calculate the \mathbf{T}_{PSMi}^{REF} by inferring \mathbf{z}_{REF} (see Figure 3.7).

To account for minor errors in the axes calculation and ensure a resulting right-hand orthogonal system, the angles between the calculated axes are slightly adjusted by first calculating the offset from 90° or $\frac{\pi}{2}$ for the initially calculated axes $\mathbf{x}_{PSMi}^{REF,tmp}$ and $\mathbf{y}_{PSMi}^{REF,tmp}$ equivalently

$$\Delta\theta = \frac{\pi}{2} - \arccos\left(\frac{\mathbf{x}_{PSMi}^{REF,tmp} \cdot \mathbf{y}_{PSMi}^{REF,tmp}}{|\mathbf{x}_{PSMi}^{REF,tmp}| |\mathbf{y}_{PSMi}^{REF,tmp}|}\right) \quad (3.1)$$

and subsequently updating both axes with half the angle

$$\begin{aligned} \mathbf{x}_{PSMi}^{REF} &= \cos\left(\frac{\Delta\theta}{2}\right) \mathbf{x}_{PSMi}^{REF,tmp} + \sin\left(\frac{\Delta\theta}{2}\right) \mathbf{y}_{PSMi}^{REF,tmp} \\ \mathbf{y}_{PSMi}^{REF} &= -\sin\left(\frac{\Delta\theta}{2}\right) \mathbf{x}_{PSMi}^{REF,tmp} + \cos\left(\frac{\Delta\theta}{2}\right) \mathbf{y}_{PSMi}^{REF,tmp} \end{aligned} \quad (3.2)$$

To calculate the translation for a full homogeneous transform, a minimization of the squared error between all spatial landmarks is considered. This is achieved by calculating the mean overall offsets between the known locations on the phantom

$$\mathbf{p}_{PSMi}^{REF} = \frac{1}{n} \sum_{j=0}^n (\mathbf{p}_{PSMi}^{(j)} - \mathbf{T}_{PSMi}^{REF} \mathbf{p}_{REF}^{(j)}) \quad (3.3)$$

with $\mathbf{p}_{PSMi}^{(j)}$ and $\mathbf{p}_{REF}^{(j)}$ denoting the position of the j^{th} spatial landmark \mathbf{T}_{PSMi}^{REF} and \mathbf{T}_{REF} respectively. In total, a fiducial registration error of $0.65 \pm 0.21mm$ is observed.

3.3.3 Ultrasound Hand-Eye-Calibration

In addition to registering the two robotic arms, hand-eye calibration was necessary to register the US probe with the robotic tool tip and thus the robot's base frame. This is

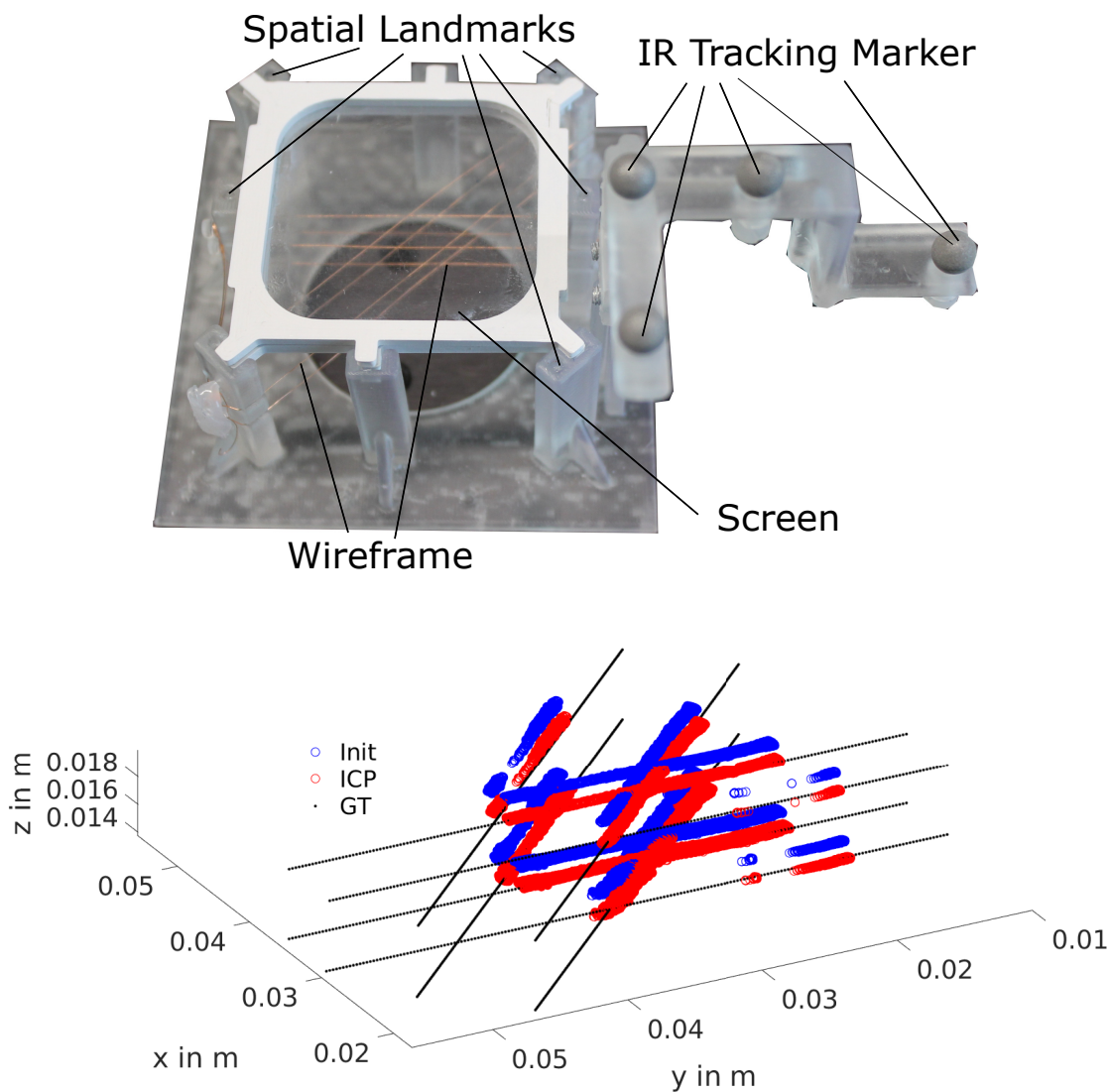


FIGURE 3.7: **Top:** Wireframe used for hand-eye calibration. **Bottom:** Point clouds obtained from US scanning the phantom prior to ICP (Init), after ICP (ICP) and ground truth (GT).

usually achieved by scanning an US phantom with known geometry and feature position with respect to the robot and calculate the transformation necessary to overlay the two. For this matter, a custom wire phantom similar to [167] was designed that consists of two layers of four intersecting wires ($10\mu m$ copper wire). Figure 3.7 shows the designed frame holding the intersecting wire. The wires are spanned across four poles. A frame with a thin, transparent plastic sheet was added to provide a rigid scanning surface, while not obstructing the scan. Additionally the frame was used to spread the poles, further tensioning and straightening the wires.

Due to the robot's large compliantness and the resulting uncertainty in its kinematics, an

IR tracker with known position on the phantom was integrated. This made it possible to reference the scan from the US probe's own IR tracker to the fixed frame attached to the phantom. The image dimensions were given by the manufacturer. Whereas the probe width is fixed at 22.9mm , the depth can be set in the US machines menu. Using the point clouds from the IR tracking data, an Iterative Closest Point (ICP) routine was applied to determine the transformation between the assumed ground truth point and cloud and the final point cloud. The process of scanning and ICP was repeated several times until reaching 0.33mm root mean square error. The resulting point cloud overlay is depicted in Figure 3.7.

Chapter 4

Autonomous Ultrasound Scanning and Navigation

This chapter presents the research carried out along the track of autonomous US navigation along vascular structures. It identifies the specific challenges to be solved to transfer autonomous US scanning into an intracorporeal setting. As a core part of this endeavour, a method for fusing IMU data with robot kinematics is introduced (see Section 4.2.2), aiming to solve the robot’s kinematic inaccuracies in 3D space and to enable a more precise and reliable anatomic reconstruction from the US scans. Additionally, a deep learning pipeline is outlined to detect anatomical features in the image (see Section 4.2.3) as well as estimating the acoustic coupling quality with the tissue surface (see Section 4.2.4). Furthermore, a Force Sensitive Resistor (FSR) is integrated into the setup to ensure that the applied forces stay below a given threshold and allow the dealing with non-planar surfaces (see Section 4.2.5). Based on the extended platform, a planning and control routine is developed and outlined (see see Section 4.2.7) and evaluated on a commercial US liver vessel phantom (see Section 4.3 and 4.4).

This chapter was published as the following peer-reviewed journal paper:

Marahrens, N., Scaglioni, B., Jones, D., Prasad, R., Biyani, C.S. and Valdastrì, P. "Towards Autonomous Robotic Minimally Invasive Ultrasound Scanning and Vessel Reconstruction on Non-Planar Surfaces." *Frontiers in Robotics and AI*, vol. 178, 2022.

4.1 Introduction

A critical point in enabling autonomy in surgery is the knowledge of the patient's specific anatomy to adequately define resection margins for extracting diseased tissues and safely manipulate anatomical structures. While pre-operative imaging can help gain useful insights, the exact mapping of these images to the surgical site is unknown under general circumstances, both to the human or the computer. This particularly applies to highly flexible organs such as the liver, where the positioning of the patient during surgery along with CO_2 insufflation may cause significant changes in position and shape of the organ [10]. In this and other surgical scenarios, intraoperative US scanning is often adopted to acquire knowledge of the anatomy [168].

While many research efforts have been dedicated to exploring automated scanning on the patient's skin (see Section 2.3.2), scanning inside the patient during minimally invasive surgery poses several unaddressed challenges. Extracorporeal US systems adopt serial manipulators that greatly simplify precise and reliable spatial movements and force measurements.

In the context of improving robotically assisted surgery, prior works mostly employ extracorporeal [31] or endoluminal probes (inserted through natural orifices), particularly TRUS, controlled via an external robot [112, 169] to visually track robotic instruments and target regions. Due to their increased distance to the operating region, extracorporeal probes lack the details of a more close-up scan of the surgical site under general circumstances. Endoluminal US, on the other hand, is restricted to target regions that lie close to orifices (e.g., prostate) or luminal organs (e.g., esophagus) accessed via flexible endoscopes.

Minimally invasive surgical systems, on the contrary, are built compliantly, commonly with tendon-driven instruments as their end-effectors, making both precise kinematics and force measurements inherently difficult [170]. Moreover, the visual information acquired through US must be spatially mapped to the guiding robot for it to be meaningfully applied in an assistive or autonomous application. To this end, previous research identified in Chapter 2 involving surgical robots mainly resorted to optically tracking the US probe such as [6]. This is a feasible approach in the presence of a stereo endoscope, but lens distortion and the short disparity between the two lenses of the endoscope reduces its accuracy and applicability, and the markers need to be visible in the scene, posing a set of restrictive assumptions. The use of alternative technologies such as electromagnetic tracking are limited by the presence of metallic instruments [7] or metallic elements in

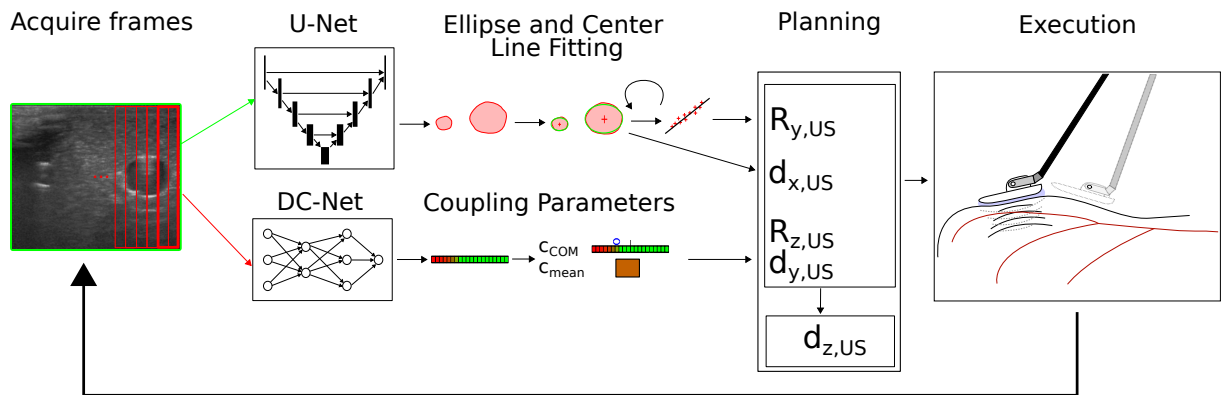


FIGURE 4.1: System Structure: The current US frame is acquired and fed into the U-Net (entire image) and DC-Net (overlapping image slices). The segmentation results of the U-Net are post-processed, and ellipses are fitted around segmentation patches likely to correspond to vessels (upper path). The current vessel center is used to perform in-plane movements ($\mathbf{d}_{x,US}$) to center the vessel within the image. Recognised vessel centers from previous frames are buffered and used to estimate the center line and reorient the image normal $\mathbf{R}_{y,US}$ (rotation around \mathbf{y}_{US} - see also Figure 4.13). The parallel path with the outputs from the DC-Net are compressed into coupling parameters that are used to adapt rotation around the image normal ($\mathbf{R}_{z,US}$) and compression movements ($\mathbf{d}_{y,US}$). If the probe alignment with the vessel and coupling is properly adjusted, the probe is progressed forward in the image plane normal direction ($\mathbf{d}_{z,US}$).

the surgical table and the potential disruption to the surgical workflow, requiring setting up and placing the field generator near the surgical site on the patient. Additionally, the aspect of non-planar surfaces remains largely unaddressed in previous work in the field of RICUS.

Given these shortcomings, this chapter investigates approaches to implement autonomous US navigation in the context of surgical robotics and intracorporeal US. Thereby, it takes inspiration from [88] working on autonomous US navigation along vascular structures to develop and assess a new approach for autonomous scanning in the context of RICUS.

4.2 Materials and Methods

4.2.1 Positional Accuracy Assessment

Aside from adequate imaging, the robot's positional accuracy plays a crucial role in accurately reconstructing the 3D spatial geometry of anatomical structures. As reported in

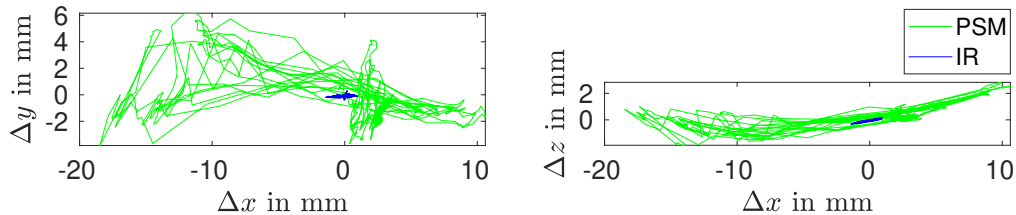


FIGURE 4.2: Position assumed by the kinematic model based on joint encoders (KIN) and measured by the IR tracking system in x - y -plane (**left**) and x - z -plane (**right**).

literature, the tendon-driven, compliant structure of the PSM causes a significant backlash [171]. To verify and further quantify the presence of this effect, an initial manual experiment was performed. To allow IR tracking and thus a ground truth reference of the robotic tool tip position, a 3D printed pick-up tool was engaged into the surgical tool and employed to provide ground truth data of the robotic tool tip pose over time.

To simulate external loading, the tool tip was then subjected to manually induced oscillatory perturbations, resulting in movements between the different extremes in the mechanical play, particularly those of the last three joints of the PSM. Figures 4.2 and 4.3 show the resulting movement pattern. As it can be observed, the PSM trajectory hardly reacts to the movements, while the IR tracking sees clear changes up to 17mm and up to 20° from the starting position.

While the first three joints of the robot were found to be relatively spatially fixed without major backlash, the three joint of the instrument, aside from the jaw, were found to cause a majority of the play observed in cartesian position.

4.2.2 IMU Kinematic Sensor Fusion

Justified by the experimental finding of significant backlash, methods to allow for improved kinematic accuracy were investigated. As opposed to most previous works that have resorted to visual markers, this work was set out to investigate more practical means to improve kinematic accuracy, without relying on the visibility of markers.

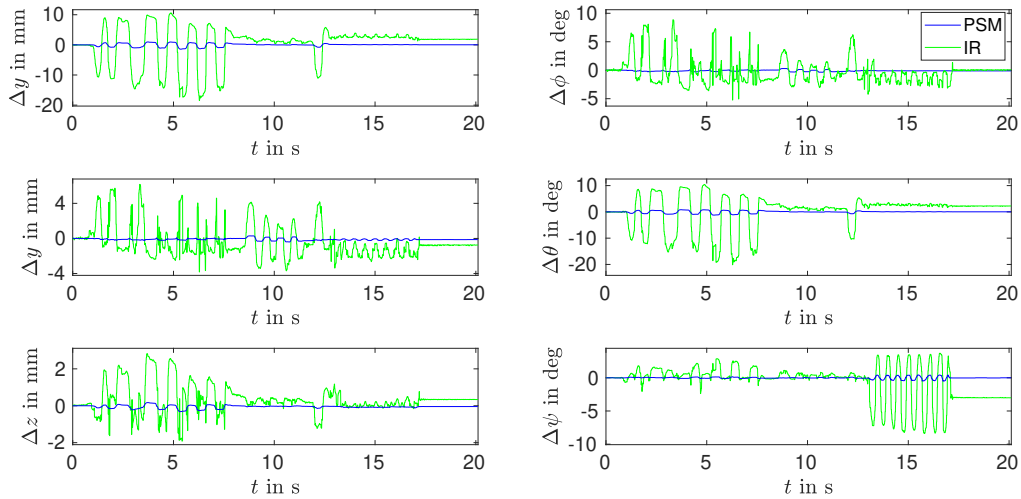


FIGURE 4.3: Position assumed by the kinematic model based on joint encoders (KIN) and measured by the IR tracking system in all six spatial DOFs.

Considering a sensor-based solution integrated into the probe, the idea arose to measure the attitude at the tip of the instrument and fuse it with the rest of the kinematics. Compared to visual approaches extracting the 3D point cloud of the instruments [172] or tracking visual markers [30] these may have the advantage of not requiring hand-eye calibration and the instruments to be visible in the endoscopic image at all time that may not always be feasible during a clinical routine. Additionally, the instrument and markers may get covered up with blood or other bloodily liquid, deteriorating the detection quality. To pursue this avenue further, the US pick-up probe was developed to integrate an IMU (Bosch BNO055, Bosch GmbH, Stuttgart, Germany) measuring gravity and thus the attitude of the probe or equivalently the robotic tool tip. The internal algorithm on the IMU performs constant recalibration to minimise drift. To make an application under realistic surgical circumstances more likely, the available magnetometer readings are ignored as clinical settings may pose widely varying magnetic conditions, including the presence of large metallic objects (e.g. surgical operating table) and the potential proximity to large electro-magnetic fields (e.g. caused by electrosurgery). While the former could be calibrated for, the latter may restrict its application and prevent translating the fusion approach to active surgical tools. Additionally, the magnetometer would have required further calibration prior to each procedure that may have increased the complexity of the system and the integration into the surgical workflow. Further ignored were the measured accelerations and rotational velocity readings, as these measurements were found to be too noisy with up to $0.3^\circ/s$ and $190\mu g/\sqrt{Hz}$ for accelerometer and gyroscope respectively

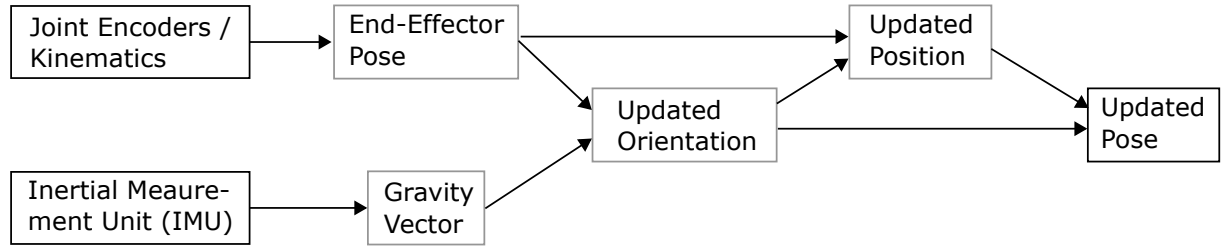


FIGURE 4.4: Signal flow of the imu sensor fusion scheme. The kinematic pose and measured gravity vector are fused to obtain an updated orientation of the tool tip. Based on the new orientation an updated position is inferred leading to a fully updated pose.

according to the manufacturer. At the same time, the movements were performed at a relatively low velocities (maximum of $5 \frac{mm}{s}$) and only occasional slow rotation (maximum of $2.5^\circ/s$) during center line or coupling quality adaption the system performs and thus practically unusable.

Rather than designing a recursive fusion approach, which would have continuously updated the fused results from the previous iteration and equally considered both measurement sources, it seemed more adequate to separate the kinematics and IMU sensor measurements and reduce a filter-induced time-delay by only including the current measurements. The routine thus fully relied on the measured attitude from the IMU where possible, since the backlash would have caused blind spots deteriorating the fused results. To fuse the robot kinematics and the IMU in this way, the proposed scheme starts by considering the spatial orientation determined by the robot kinematics as well as the gravity vector from the IMU (see Figure 4.4). Following the logic of a Mahony filter [173], it calculates the update in orientation in the following way:

$$\Delta\omega_{US}^{US,fused} = \mathbf{z}_{US}^{PSM} \times \frac{\mathbf{g}_{US}}{\|\mathbf{g}_{US}\|} \quad (4.1)$$

where \mathbf{z}_{US}^{PSM} is the z-axis of the global frame \mathbf{T}_{PSM} , expressed in \mathbf{T}_{US} , and \mathbf{g}_{US} , the gravity vector expressed in \mathbf{T}_{US} . Employing the quaternion product, $\Delta\omega_{US}^{US,fused}$ is then mapped into a quaternion velocity and used to update the orientation of \mathbf{q}_{PSM}^{US} to acquire $\mathbf{q}_{PSM}^{US,fused}$

$$\Delta\mathbf{q}_{US}^{US,fused} = \frac{1}{2} \mathbf{q}_{PSM}^{US} \otimes \left(0, \Delta\omega_{US}^{US,fused} \right) \quad (4.2)$$

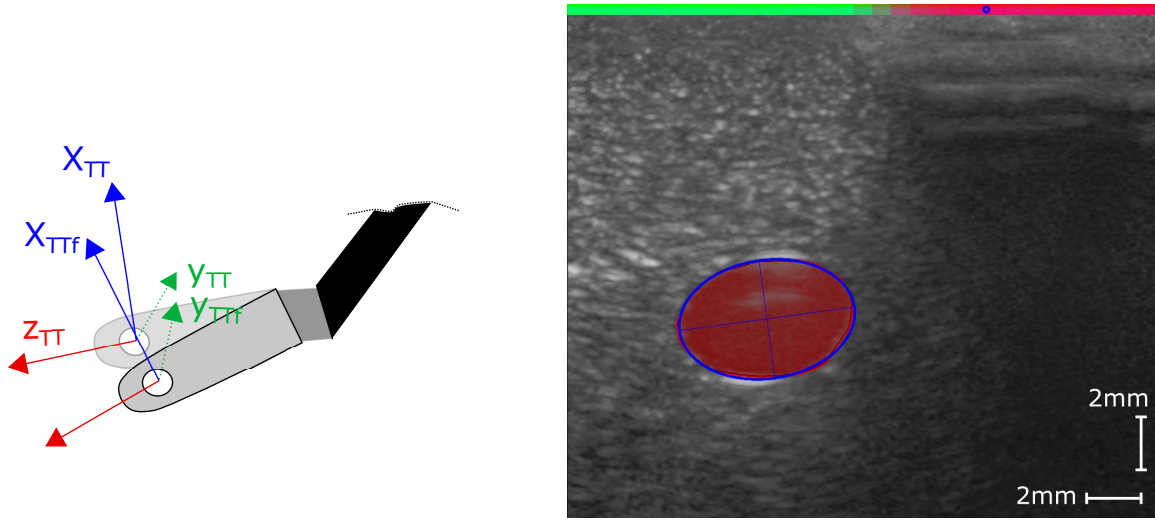


FIGURE 4.5: **Left:** Update of the end-effector orientation and global position \mathbf{T}_{TT} via attitude sensor fusion resulting in fused tool tip frame \mathbf{T}_{TTf} . Based on \mathbf{T}_{TTf} , \mathbf{T}_{US} is updated as well (not depicted for simplicity) **Right:** Visual representation of the post-processed outputs of the two Deep Neural Networks. The fitted ellipse (blue outline) closely tracks the segmentation results of the U-Net (area in red). The detected coupling quality by the DC-Net is visualised by the coloured bar on the top transitioning from green (good coupling) to red (poor coupling) and the blue circle representing the calculated c_{COM} parameter.

$$\mathbf{q}_{PSM}^{US,fused} = \frac{\mathbf{q}_{PSM}^{US} + \Delta\mathbf{q}_{US}^{US,fused}}{\|\mathbf{q}_{PSM}^{US} + \Delta\mathbf{q}_{US}^{US,fused}\|} \quad (4.3)$$

where \otimes is the quaternion product (see Equation A.11). A more detailed definition of the quaternion maths used can be found in Section A.4 in the appendix.

Assuming the backlash to be mainly present on the instrument as opposed to the roll-pitch-insertion mechanism (see Figure 2.2) and significantly larger than other potential sources of backlash such as gears or mechanical rotational joints, the orientation can be used to imply a different tool tip position. This may be reasonable assumption as the instrument is actuated via a significantly longer tendon causing larger effects of friction and elasticity. This process is depicted in see Figure 4.5. Therefore, the approach goes back in the kinematic chain along the end-effector link to the ultimate joint and updates the end-effector position based on the updated orientation.

$$\mathbf{x}_{PSM}^{TT,fused} = \mathbf{x}_{PSM}^{TT} + \mathbf{R}_{PSM}^{TT} \mathbf{z}_{TT}^{PTCHL} - \mathbf{R}_{PSM}^{TT,fused} \mathbf{z}_{TT}^{PTCHL} \quad (4.4)$$

where \mathbf{z}_{TT}^{PTCHL} is the length of the pitch link or equivalently, the vector connecting the tool tip with the last joint ($\mathbf{z}_{TT}^{PTCHL} = [0, 0, -l_{TT,PTCHL}]$) on the robotic instrument. Also see eq. 5.1 for an updated version used in for the ES and HIFUS tools in the upcoming chapters.

Note that while the approach is inspired by the logic of a Mohony filter, the scheme applies the full update in each step ($K_p = \frac{1}{\Delta t}$) and breaks the recursiveness by newly starting with the measured \mathbf{z}_{PSM}^{US} from the robot's kinematics in each time step. In the following, this approach will be referred to as IMU-fused kinematics, as opposed to the pure PSM kinematics obtained from joint encoder reading and forward kinematics.

4.2.3 Vessel Segmentation

Aside from improving the kinematic accuracy of the system, a reliable segmentation algorithm was needed to enable spatial awareness of the system and the desired navigation along anatomical structures. Therefore, in line with previous works such as [88] and [174], a U-Net [50] was adapted and trained to segment out vessel cross-sections from the US image frames. The network was trained with manually collected and labeled data from two anatomically different US vessel phantoms, BLUEPHANTOM Branched 2 Vessel Ultrasound Training Block Model (CAE Healthcare, Saint-Laurent, Quebec, CA). As loss function the model uses the sum of binary-cross entropy and dice loss in the following form

$$\begin{aligned} \mathcal{L}(y, \hat{y}) = & -\frac{1}{MN} \sum_{k=0}^N \sum_{i=0}^M (\mathbf{y}_{i,k} \log(\hat{\mathbf{y}}_{i,k}) + (1 - \mathbf{y}_{i,k}) \log(1 - \hat{\mathbf{y}}_{i,k})) \\ & + \left(1 - \frac{1}{N} \sum_{k=0}^N \left(\frac{2 \sum_{i=0}^M (\mathbf{y}_{i,k}^T \hat{\mathbf{y}}_{i,k}) + \epsilon}{\sum_{i=0}^M (\mathbf{y}_{i,k} + \hat{\mathbf{y}}_{i,k}) + \epsilon} \right) \right) \end{aligned} \quad (4.5)$$

$\hat{\mathbf{y}}_{i,k}$ and $\mathbf{y}_{i,k}$ being the flattened predicted and ground truth outputs respectively, with index k selecting the batch and i selecting the element of the flattened output. The variable $\epsilon = 10^{-6}$ is further added to prevent potential division by zero. Contained in the dataset are a total of 697 labeled images (non-augmented), splitting up into 592 (85%) for training and 105 (15%) for evaluation. Each image contains up to three vessel cross-section labels, with the majority containing a single one. For training and prediction the images were scaled down to 384×384 pixels.

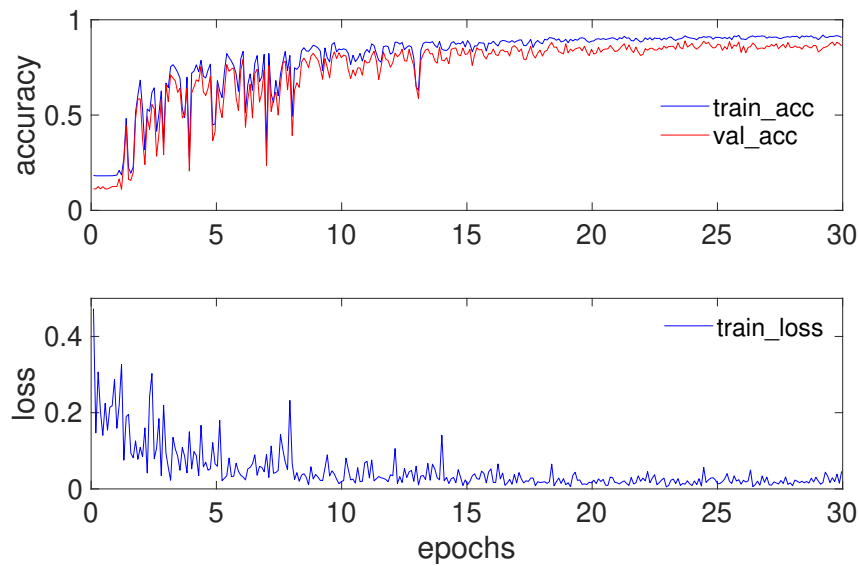


FIGURE 4.6: Training graphs of U-Net trained to segment vessel cross-sections

The model was trained for 30 epochs using a starting learning rate of 0.001 that was successively adapted by a factor of 0.2 when the prediction results plateaued. The starting value was identified to lead to larger scale network adaptations while still leading to a stable training behaviour that didn't diverge. The batch size, meaning how many images were fed to during a single training iteration, was set to 5 as larger batch sizes would fill the GPU memory to much. The final model after training has a validation Dice score of 0.887 (see Figure 4.6). The network runs on a NVIDIA Quadro RTX5000 leading to final inference speeds of 7-8fps.

In its raw form, the U-Net represents segmentation masks as binary pixelated images. Further processing is therefore needed to compress the data into more meaningful vessel features. Therefore, the extracted contours from the filtered image are fitted with ellipses using OpenCV, allowing a differentiation between several vessel instances (instance segmentation). By assuming a lower threshold vessel diameter of 20 pixels (corresponding to a vessel diameter of around 0.45mm) for the navigational task at hand, the approach sorted out potential erroneous or irrelevant vessel detections. Figure 4.5 shows a typical result of a detected vessel after post-processing the segmentation. The image processing routine starts by applying initial filtering (erosion, dilation, thresholding) to eliminate small noisy patches that are unlikely to correspond to actual vessels.

4.2.4 Visual Coupling Quality Estimation

Additional essential information that can be extracted from the image is the quality of acoustic coupling between the US probe and the tissue surface. Having a good contact is paramount to ensure adequate imaging of the structures below the surface and proper working of the segmentation algorithm in detecting anatomical structures. Therefore, common approaches in the literature include the usage of US confidence maps [175] and entropy [176]. Both methods, however, rely on hand-tuning parameters to fit with the current US settings. Furthermore, using entropy was found to be particularly sensitive to the blood vessels of our phantom, detecting them as artefacts. Both methods are also quite computationally intensive. Therefore, it was decided to investigate data-driven approaches, using neural networks. While not being realised eventually, the further intention of this was to integrate this network into the U-Net structure already implemented for vessel detection.

For quantification of the coupling quality and the detection of a decoupled probe, the system integrates a convolutional neural network, in the following referred to as Decoupling Network (DC-Net). Due to the wave-nature of US, a poor coupling between the probe and tissue in a location on the sensor will affect the whole image slice along the propagation direction of the US wave (depth of the image). Based on this observation, the idea arose to split the task up into various image slices. Rather than processing an entire image at once and solving the regression task of estimating the coupling quality across the image's width, the network is hence fed fully overlapping slices, including half of the information from each neighboring slice. This vastly reduces the size of the network and simplifies it to a binary classification task (good/poor coupling) on each separate slice. Furthermore, this approach additionally increases the number of available data samples for training and evaluation as each image splits up into several slices. Making the slices overlap is meant to increase the robustness of the system due to the inclusion of partly redundant visual information seen in different contexts. Each image is split into 32 slices, which were chosen to be a compromise between resolution and performance.

The final network is comprised of four convolutional layers with depths 32, 32, 64, and 64, respectively, followed by two dense layers. Between each of the convolutional layers, the output passes through a leaky ReLU activation ($\alpha = 0.05$) function followed by anisotropic max pooling (4 in depth and 2 in width dimension). The latter accounts for the large pixel ratio of 8:1 between the depth and width of the extracted slices. Following the convolutional layers, the flattened output is processed through two dense layers with

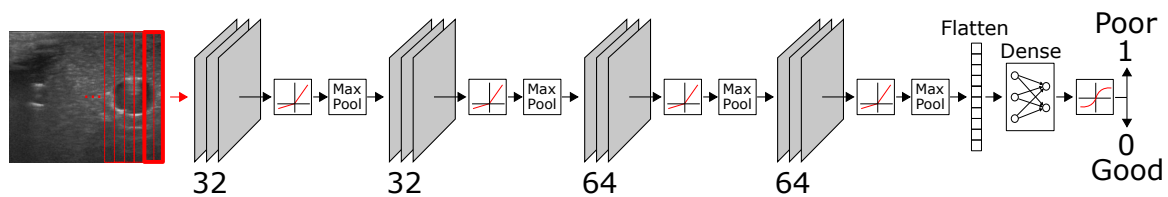


FIGURE 4.7: Structure of the DC-Net with four convolutional layers, each directly followed by a leaky ReLU layer and anisotropic max pooling. The flattened output of the first four layers is further processed through two dense layers, including an in-between ReLU and dropout layer ($p = 0.5$) and a final softmax layer for binary classification into coupled (0) and decoupled (1).

an in-between ReLU activation function and dropout of 0.5. The final classification result is generated via applying a softmax activation to the output of the last dense layer (see Figure 4.7), resulting in values between 0 (coupled) and 1 (decoupled). The data set is comprised of a total of 6634 image slices with 40% of samples labeled poorly coupled and 60% well coupled. After 250 training epochs on 85% of data samples, the DC-Net reach an overall validation accuracy of 0.99 on the remaining 15% of samples.

To reduce the number of classified slices into parameters that give meaningful indications for probe adaptations, two parameters are proposed that summarise the coupling over the width of the image and are used to adjust the probe orientation and position. A similar approach is also used in [92]. As a first control parameter, the center-of-mass (CoM) equivalent of the classified coupling quality is determined as follows

$$c_{COM} = \frac{\sum_{i=0}^n (c_i d_i)}{\sum_{i=0}^n d_i} \quad (4.6)$$

with n being the number of slices in the image, c_i the coupling quality of slice i , and d_i the distance of the center of the slice to the center of the image. The network is trained to classify slices as strictly 0 or 1; however the final approach employs the floating-point values given by the ultimate softmax layer to result in values between 0.0 (good coupling) and 1.0 (poor coupling) for further calculation of coupling quality parameters. While the values might seem counter-intuitive at first glance (higher value equals lower coupling quality), they were chosen to represent 0 as the default state (good coupling) compared to in-equilibrium as any offset from 0 (poor coupling). If all slices are near 0 (e.g., smaller than 0.1), c_{COM} is expected to be in or very close to the center of the image. Running on a NVIDIA Quadro RTX5000 in parallel with the U-Net for vessel segmentation, the network inferred at in less than $1ms$, causing minimal overhead to the costly segmentation of the image.

4.2.5 Contact Force Detection

As previously outlined in Section 2.3.3, several approaches have been investigated to deal with estimating force at the tool tip of the robotic instrument. The two main approaches identified were either based on a mechanical model [127] or neural network-based [128]. The first approach that was implemented, is based on [127]. It therefore considers a mechanical model of the robot including link masses, tendon elasticity and friction. By rearranging the equations a linear relationship between joint states and external forces through the robot parameters is obtained. Since joint states (angle, angular velocity, effort) can be measured and external force kept zeros, a convex optimisation routine can be employed for its solution. The code available from github¹ was adapted and run with the optimised trajectories. Secondly, the approach from [128] based on neural networks inverse dynamics identification was implemented. In this a separate dense neural network is trained to predict the projected forces from the tool tip based on measured joint states (angle, angular velocity, effort) [128]. I created a dataset covering a wider range of the configuration space, as suggested in original publication.

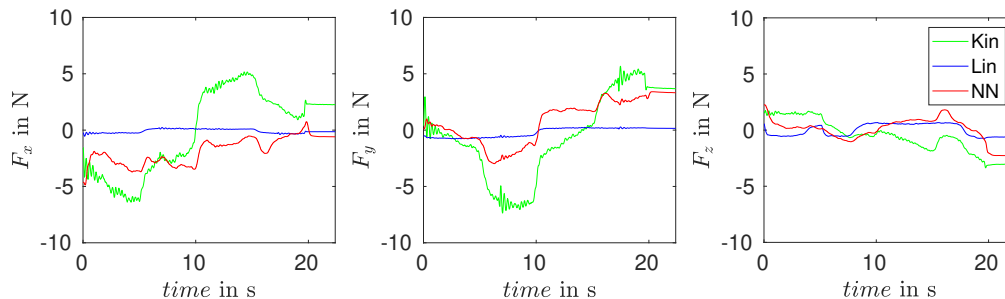


FIGURE 4.8: Force Estimation results in all three spatial directions using joint torques (KIN), linear regression model (LIN) and neural network (NN) in \mathbf{T}_{tt} coordinates.

As Figure 4.8 shows, the methods perform significantly differently, moving the end effector without loading. Unsurprisingly, the kinematic mapping of the joint encoders performs the worst as it does not account for robot dynamics. However, even the neural network introduces significant errors. The linear model is the only one that performs reasonably well. However, when applying this approach to a load situation it was found to also be unfit for providing realistic force measurements. Figure 4.9 shows the results of a circular trajectory of pick up tool interacting with a soft surface. While the ground truth force stays relatively constant around 1N, the force predicted by the model changes along the trajectory and with changes in its joint angles.

¹https://github.com/WPI-AIM/dvrk_dynamics.identification

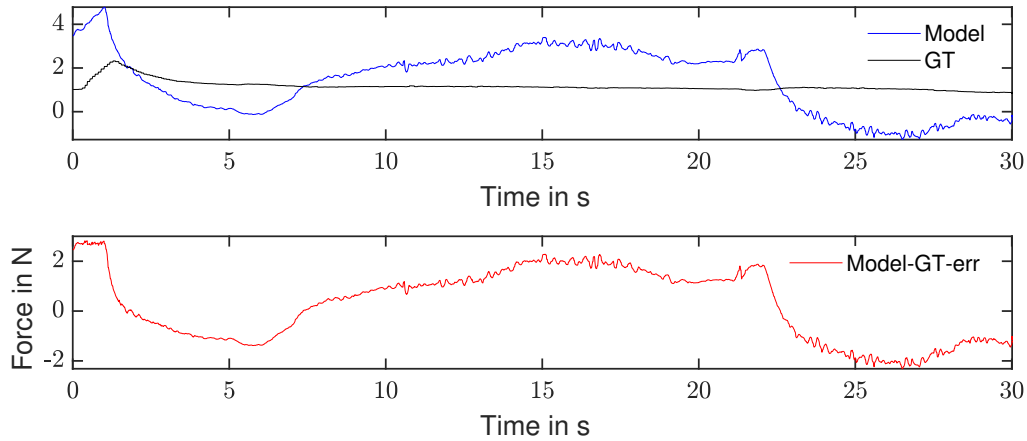


FIGURE 4.9: Force errors of linear model force estimation on circular trajectory and planar surface with constant normal orientation compared to ground truth

4.2.6 FSR Integration and Calibration

As the previous analysis, assessing force estimation algorithms in the context US probe scanning, showed that no method was capable of dealing with typical force loadings induced during robotic US probe guidance, it was decided to move forward with a sensorised option. The most suitable option for this was identified to be a Force Sensitive Resistor (FSR), located between the pick-up interface and the top of the US probe. While not ideal in terms of adding an additional sensor to the setup, the sensor is relatively easy to integrate and calibrate. As a flat, plastic-laminated sheet, it has a small footprint (e.g. compared to a load cell), easily fitting between the probe and the pick-up interface, and could in theory be easily sterilised with isopropyl alcohol or other chemical sterilisers.

Mapping from voltage readings to force magnitudes, required the calibrating of the FSR readings to know forces. After the FSR had been placed and the pick-up interface assembled around the US probe with a preload onto the FSR, the setup was fixated around the pick-up interface. A scale on a raisable platform was placed below. By increasingly lifting the platform towards the fixated pick-up interface a contact of increasing magnitude was simulated. The platform was manually lifted to achieve force increments between $0.5N$ and $2N$. Figure 4.10 shows the resulting data points that were obtained, outlining a clear linear behaviour. Therefore, the conversion factor and bias of the FSR voltage with respect to an applied normal force to the probe were calculated. The resulting R^2 for the linear model was 0.992.

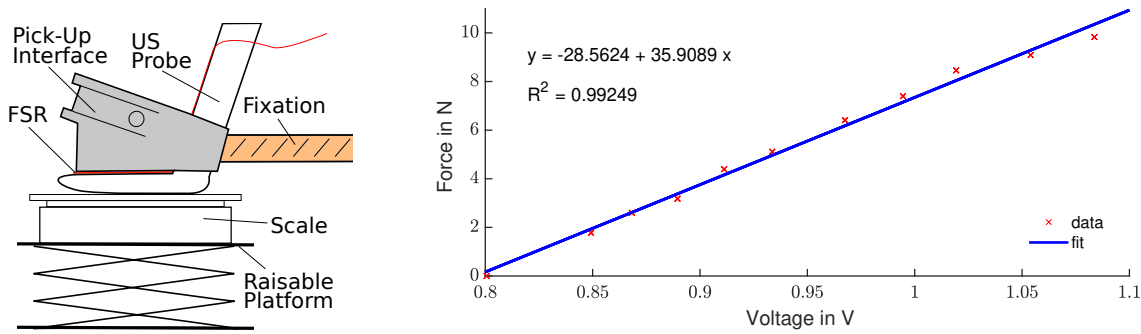


FIGURE 4.10: **Left:** Experimental setup with the pick-up interface fixated and a movable scale pushing on the US transducer surface from below. **Right:** FSR calibration results

4.2.7 Planning and Control

With the basic hardware and software infrastructure developed, a main task was to provide an intelligent planning and control framework that would allow scanning and navigating along the vessel structure. To simplify the control problem, the probe manipulation is split up into four independent movements: orientation matching with the projected center line of the vessel (rotation around y_{US} -axis), vessel centering (in-plane movement in x_{US} -direction), forward movement along the vessel (out-of-plane movement in z_{US} -direction) and coupling optimization (in-plane movement in y -direction and rotation around x_{US} -axis). The only direction not considered for adaption is rotation around x_{US} , which for now is assumed to remain nearly constant. Each control cycle starts with a check of the coupling quality; further movements are considered in case of good coupling quality. Otherwise, the coupling is adjusted until reaching an acceptable level. A good value was found to be $|c_{COM}| < 0.1$. This is to ensure that the feature is not suddenly lost due to the poor coupling of the probe. Assuming the coupling is adequate, the planner continues with a proportional controller to keep the detected vessel centered in the image frame. In the subsequent layer, the planner checks for deviations of the image plane normal with respect to the estimated vessel center line projection. If no orientation adaptations are needed, meaning the probe is well coupled, with the vessel centered and the image plane normal z_{US} orientated in accordance with the current center line estimate, the probe is propagated forward in image plane normal direction (in direction of z_{US}). All routines further include a limited proportional controller to keep the vessel centered in the image.

If one of the sides of the probe decouples, c_{COM} is expected to shift toward the decoupled side (see Figure 4.11). As a result, the planner tilts the probe towards the respective direction to re-establish coupling. This process is depicted in Figure 4.11, where the

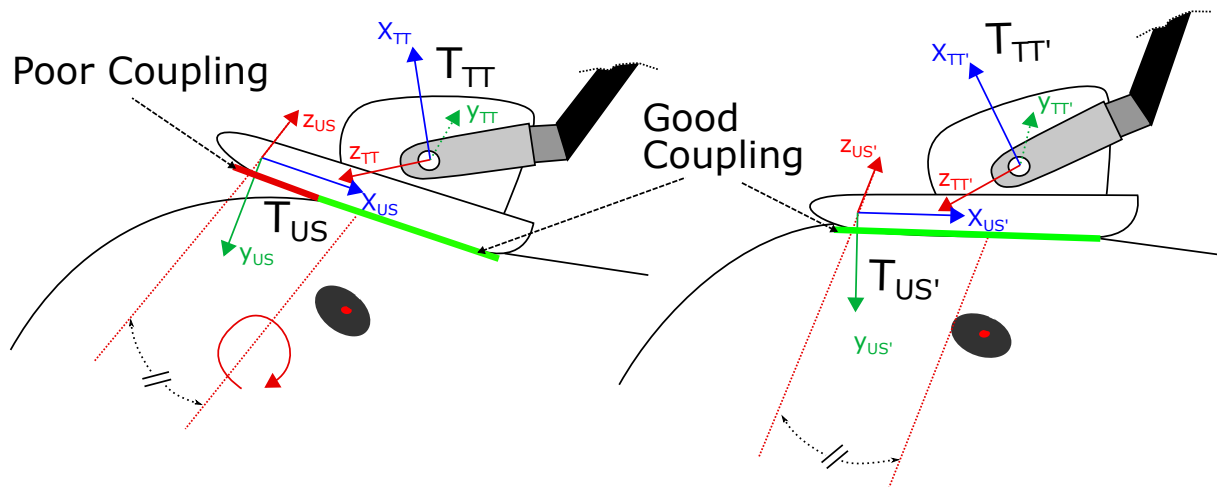


FIGURE 4.11: Coupling adaption of the US probe via rotation around \mathbf{z}_{US} axis (equivalent to image normal vector), shifted into the center of the image probe. To determine the amount and direction of probe angle adaption the condensed c_{COM} parameter is employed (see Eq. 4.6)

probe is rotated around \mathbf{z}_{US} shifted into the middle of the probe (half a probe width into \mathbf{x}_{US} direction). In addition to c_{COM} the scheme considers the overall mean as well as the mean of the left, central and right third of the image to allow downwards probe movements in the case that the entire probe is not well coupled.

To prevent excessive forces from being applied, the FSR was used to control the probe away from the surface if necessary. To account for signal drift in the FSR, the probe was zeroed before each scan, e.g., while holding it slightly above the tissue surface to be scanned. In the current setup, the force is set not to exceed $3.5N$. In case $3.5N$ are exceeded, the probe is lifted off in direction of \mathbf{y}_{US} until the value is below the threshold to the optimise potential further decoupling on the sides of the probe. Furthermore, this was found to be a good value for ensuring proper coupling on the given phantom, while preventing noticeable deformations. The precise value may differ for softer phantoms or tissue.

A further assumption made is that sufficient liquid is present on the scanning surface. As opposed to the patient's skin the inside of the abdominal cavity is sufficiently moist, and additional water is usually added via an irrigation rod prior to scanning.

Looking at Figure 4.12, the planner has thus far ensured adequate coupling, via the parameters extracted from the image and the FSR measurements. Next, the vessel is centered in the frame. This achieved via calculating the relative distance of the vessel center to the center of the image

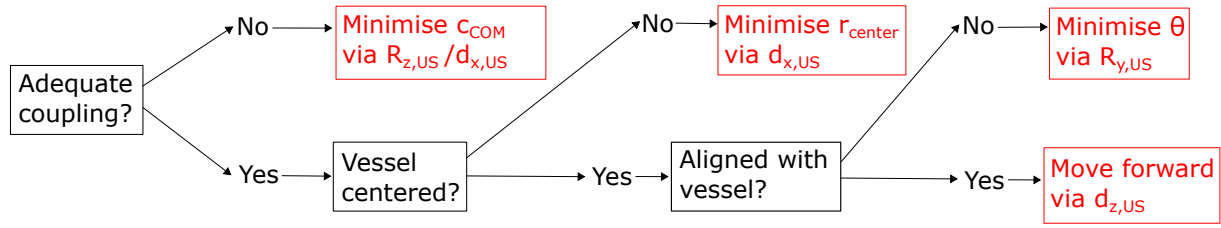


FIGURE 4.12: Outline of the hierarchical planning routine, employing different tracks for adapting the probe orientation and position with respect to the tissue surface or the reconstructed anatomy. The planner prioritises in the order of coupling over the centering of the vessel and finally the alignment of the vessel center line.

$$r_{center} = \frac{i_c}{n_x} - 0.5 \quad (4.7)$$

with i_c being the pixel id of the vessel center in image width direction (x_{US}) and n_x being the total number of pixels. The control target is thus to minimise r_{center} . The remaining task to be solve is to adapt the out-of-plane probe orientation. To get an optimal cross section of the vessel, the center line of the vessel should be aligned with the image normal axis. In order to estimate the vessel center line and eventually adapt out-of-plane movements with respect to the vessel, the algorithm considers the last 30 detected vessel center points in globally fixed PSM coordinates. The point cloud is assessed to be only valid if around 90% of samples include a detected vessel and are not acquired during probe orientation adaption, which was empirically determined to be a good value for stable estimation of the center line. If this criterion is not fulfilled, the current orientation is kept as the best estimate. Thereby, the potentially high amounts of noise from the kinematics during rotational movements to affect the estimated center line orientation is minimised and thus the image normal adaption. Additionally, the algorithm imposes a minimal distance covered between the points in the current point cloud to ensure that a line fitting is feasible and accurate. While the point cloud sets obtained from non-normal scan movements are ignored, they are still included for the final reconstruction of the vessel. Two separate least-square line fittings determine the slope of the center line for all three spatial dimensions. The resulting slope is then transformed into the US probe frame and project the center line onto the \mathbf{x}_{US} - \mathbf{z}_{US} -plane (see right of Figure 4.13). This ensures that the probe only rotates around assumed surface normal y_{US} and does not lift off or push further into the surface, altering the coupling in unexpected ways. The approach can be summarised with the following formula:

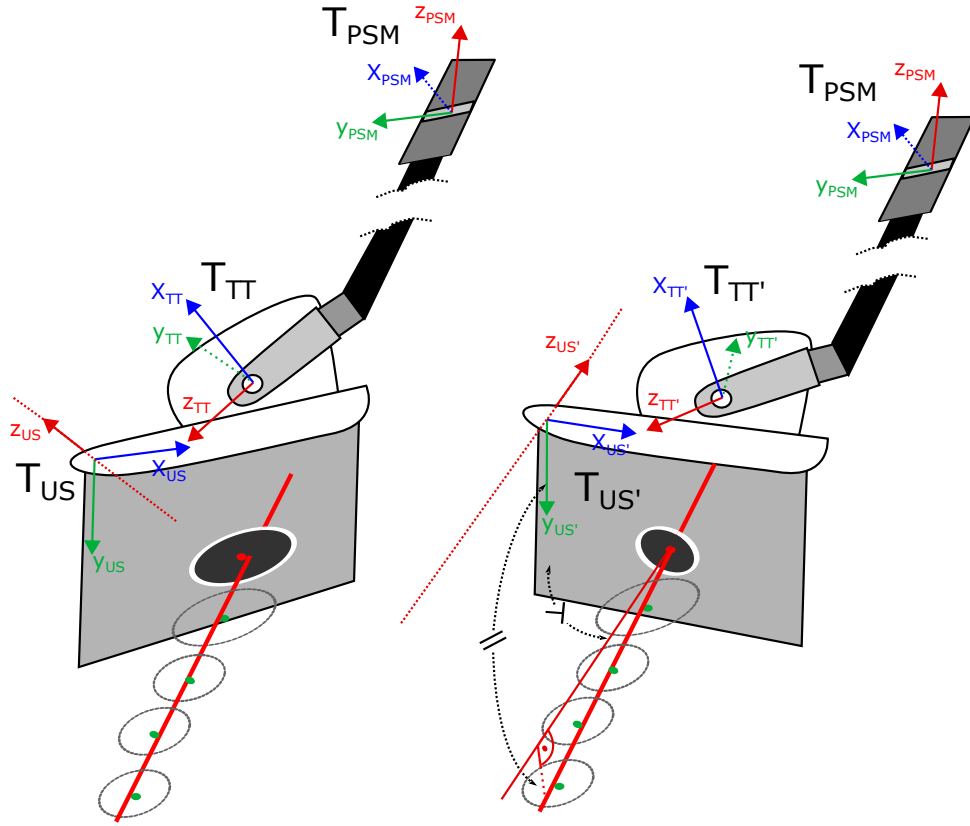


FIGURE 4.13: Considered coordinate Frames \mathbf{T}_{US} , \mathbf{T}_{TT} and \mathbf{T}_{PSM} Left: Before adaption of the image plane normal (poor orientation \mathbf{T}_{US} and \mathbf{T}_{TT}), Right: After adaption of image plane normal (ideal orientation), based on projected vessel center line (good orientation $\mathbf{T}_{US'}$ and $\mathbf{T}_{TT'}$)

$$\mathbf{z}_{PSM}^{US,des} = \mathbf{R}_{PSM}^{US} \cdot \frac{\mathbf{I}_{xz} \cdot (\mathbf{R}_{PSM}^{US})^{-1} \cdot \mathbf{t}_{PSM}^{cl}}{\|\mathbf{I}_{xz} \cdot (\mathbf{R}_{PSM}^{US})^{-1} \cdot \mathbf{t}_{PSM}^{cl}\|} \quad (4.8)$$

$$\mathbf{I}_{xz} = \begin{bmatrix} 1 & 0 & 0 \\ 0 & 0 & 0 \\ 0 & 0 & 1 \end{bmatrix} \quad (4.9)$$

where $\mathbf{z}_{PSM}^{US,des}$ is the new desired orientation of the \mathbf{z}_{US} -axis expressed with the PSM coordinate frame \mathbf{T}_{PSM} , \mathbf{R}_{PSM}^{US} is the rotation component of the homogeneous transformation between PSM and US probe coordinates, \mathbf{I}_{xz} a selector matrix to filter out the y -component in the US probe's coordinate frame, as the probe rotates around this axis, and \mathbf{t}_{PSM}^{cl} the orientation vector of the fitted center line. Put in other words, this minimises the angle θ between \mathbf{z}_{US} and the calculated \mathbf{t}_{PSM}^{cl}

$$\theta = \arccos \left(\frac{\mathbf{z}_{US}^T \cdot \mathbf{t}_{PSM}^{cl}}{|\mathbf{z}_{US}^T| |\mathbf{t}_{PSM}^{cl}|} \right) \quad (4.10)$$

constrained by rotating only around \mathbf{y}_{US} . To set up a consistent right-hand coordinate frame, the remaining \mathbf{x}_{US} -axis in PSM coordinates is determined as

$$\mathbf{x}_{PSM}^{US,des} = \mathbf{y}_{PSM}^{US} \times \mathbf{z}_{PSM}^{US,des} \quad (4.11)$$

where \mathbf{y}_{PSM} is the current y -component of the Rotation matrix \mathbf{R}_{PSM}^{US} that describes the y -axis of the US probe coordinate frame in PSM coordinates. The final desired probe rotation $\mathbf{R}_{PSM}^{US,des}$ is built by combining all axes

$$\mathbf{R}_{PSM}^{US,des} = \left[\mathbf{x}_{PSM}^{US,des}, \mathbf{y}_{PSM}^{US,des}, \mathbf{z}_{PSM}^{US,des} \right] \quad (4.12)$$

4.3 Experimental Setup

To mimic the setting of a hepatectomy, all scanning experiments were performed on a Branched 2 Vessel Ultrasound Training Block Model (CAE Healthcare, Saint-Laurent, Quebec, CA), depicted in Figure 4.14. The vessel phantom resembles vessels similar to those found in the liver with diameters between 4 – 6mm. The phantom consists of a straight main vessel with a second vessel branching off around 45mm down the length of the vessel at a 60° – 70° angle. This vessel slowly curves until it runs roughly parallel to the straight vessel (see Figure 4.14), finally bending downwards at a roughly 15°. Since the exact vessel location and orientation in 3D space is unknown, IR trackers were added to the experimental setup that is used to acquire ground truth data (accuracy of 0.1mm). However, the tracking system is not intended as part of the setup used during a potential future surgical application. To acquire a mapping between the IR tracking system and the PSM end effector, a 3D printed frame was designed that is tracked via the IR tracking system. On the side of the PSM the frame is spatially registered to the \mathbf{T}_{PSM} via touching spatial landmarks and calculating the resulting transformation. All robotic and US data, including the segmentation results and extracted vessel ellipses, are published on ROS topics for further processing and exchange between the several program routines.

The experiments are comprised of scans of the curved vessel as a non-trivial geometry for probe orientation. The scan starts from the vessel's straight section (roughly parallel to

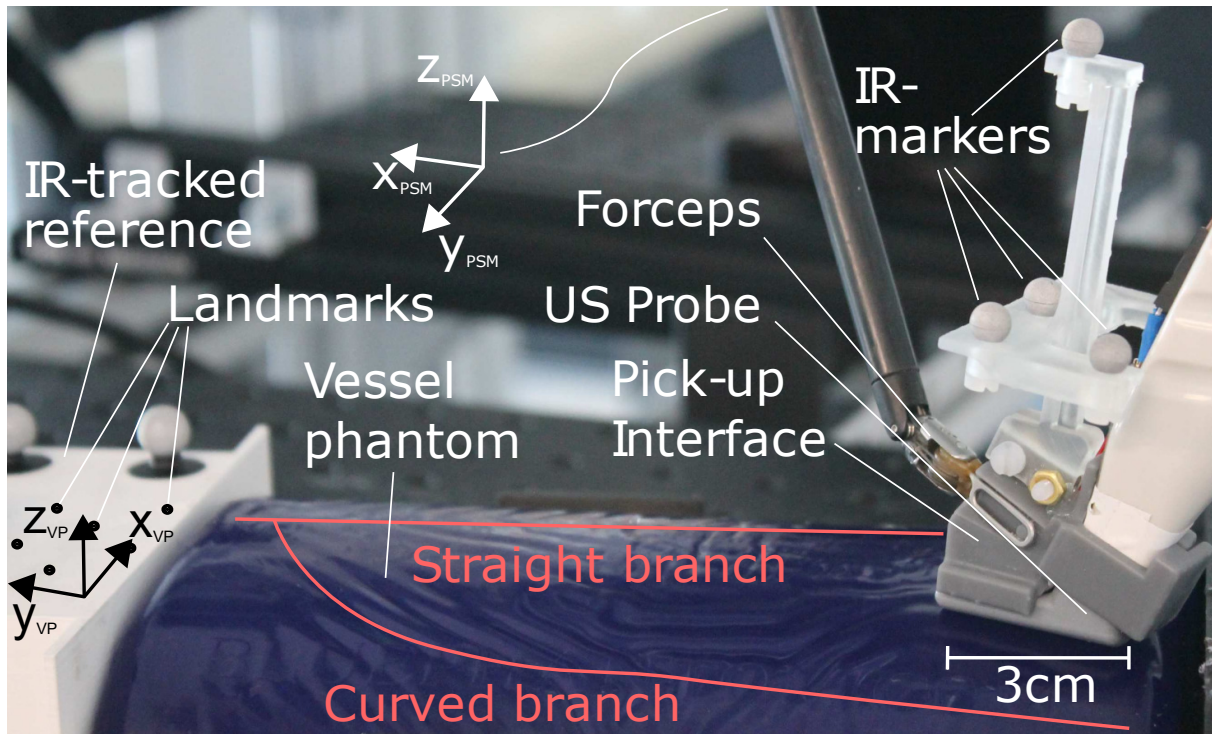


FIGURE 4.14: Setup for the experiments, with a roughly overlaid outline of the vessel structure inside the phantom, the US pick-up probe with integrated IMU and FSR and the reference block.

y_{VP} on one end of the phantom), over towards its turn, and until it merges with the main vessel towards the other end of the phantom. Due to the turn and the varying starting angles, it is practically impossible to fully scan the vessel without stable probe orientation adaption that ensures an image normal approximately parallel to the projected center line of the vessel. Each scan starts in close proximity to one end of the phantom with the probe partly decoupled from the tissue surface (similar to Figure 4.5) and with an image normal orientation clearly deviating from the center line of the vessel. The first five scans started with a rotational deviation of the center line turned towards one side, while the other five were started with a rotational deviation towards the opposite side. During the scans, the robot's position along with the detected vessel centers and axes are logged. All scans in the evaluation are extracted from runs using IMU-fused kinematics for control.

To assess the resulting scans and compare them, the root squared error (euclidean distance) between the reconstructed vessel center points using IR tracking with that of pure PSM or IMU-fused kinematics is considered for each time step i

$$e_{tot,PSM,i} = \sqrt{(p_{PSM,i} - p_{IR,i})^T (p_{PSM,i} - p_{IR,i})} \quad (4.13)$$

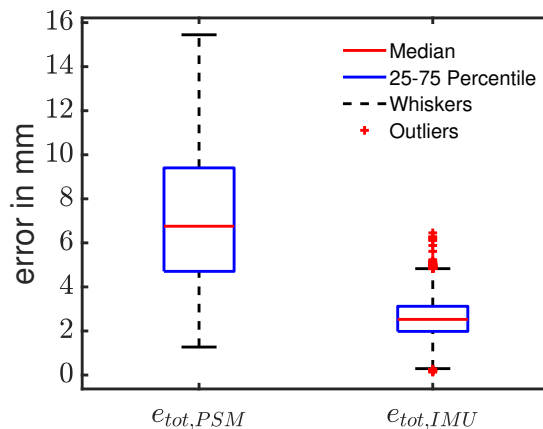


FIGURE 4.15: Box Plot showing the error distributions of the resulting scans using pure PSM- or IMU-based kinematics. Outliers are considered to be values outside the 1.5-fold interquartile range from each side of the box, demarked by whiskers ($n=12596$ data points from ten scans).

$$e_{tot,IMU,i} = \sqrt{(p_{IMU,i} - p_{IR,i})^T (p_{IMU,i} - p_{IR,i})} \quad (4.14)$$

The final analysis is reduced to the estimated center points, as the detected radius of the vessel will be the same for all methods and does not add any comparative meaning between the different methods. Furthermore, the mean difference in orientation between the IR tracking and both kinematic methods is calculated for validating and quantifying the kinematic improvements made by the addition of the IMU.

4.4 Results

Over ten runs, a mean error of $7.19mm \pm 3.12mm$ for pure PSM-based kinematics and $2.58 \pm 0.85mm$ for IMU-fused kinematics can be observed. The maximum errors observed were $15.45mm$ and $6.45mm$ for PSM and IMU-fused kinematics, respectively. The medians and quantiles of the error that are depicted in the box plot in Figure 4.15 are $6.76mm$ (median), $4.71mm$ (25% quantile) and $9.4mm$ (75% quantile) for PSM kinematics and $2.57mm$ (median), $1.98mm$ (25% quantile) / $3.1mm$ (75% quantile) for IMU-fused kinematics. The plot includes zero outliers for PSM-based kinematics and 66 outliers for IMU-fused kinematics from a total data 12596 data points.

Comparing the trajectories depicted in Figure 4.16, all scans obtained via IMU-fused kinematics appear to be closer to the true scans obtained via IR tracking. Trajectories

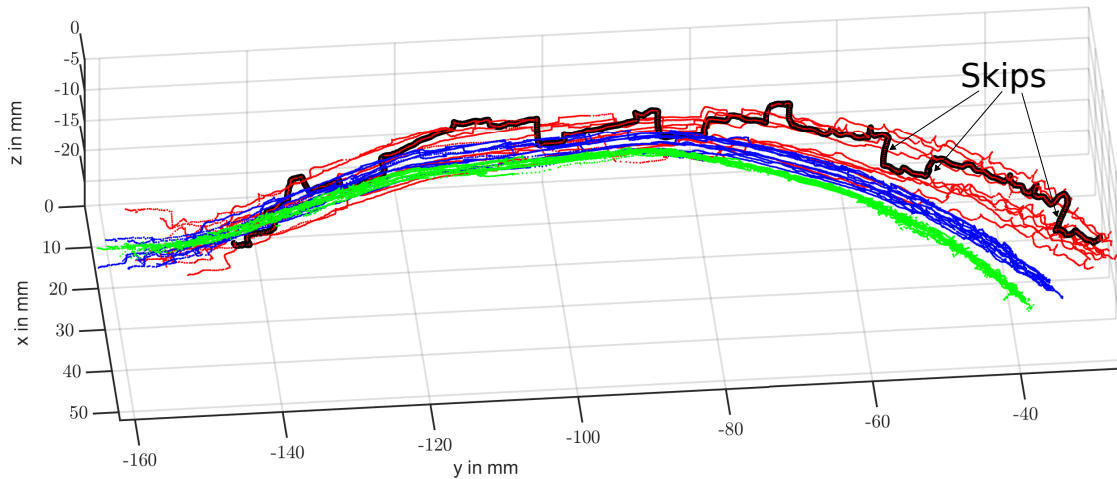


FIGURE 4.16: Resulting scans of the curved vessel branch using pure PSM-based (red), IMU-fused (blue) and IR tracked (green) kinematics. One of the PSM kinematic-based scans with particularly large skips is highlighted in black

obtained with pure PSM kinematics can also be observed to end at largely varying positions and heights (\mathbf{z}_{VP}). This is not the case for IMU-fused kinematics. This may be largely explained by the play in the joints and the compliant structure that is not accounted for in the PSMs kinematics. Secondly, the applied correction of the tool tip position in the IMU-fused kinematics is able to substantially reduce skips and positional drifts, which are strongly pronounced in the trajectories for pure PSM kinematics (see highlighted trajectory in Figure 4.16). The skips are most likely caused by play in the joints. They express the most during probe orientation of adaption, which strongly involves the two joints with the longest tendons, located near the end-effector. While the robot assumes it is moving and changing its end-effector orientation and position, it actually stays static until the joint properly engages and the joint movement is starting to be transmitted along the full kinematic chain. Along with the ten scans performed using IMU-fused kinematics, a total of ten scans was executed using pure PSM kinematics for control but found that only four out of the ten scans were completed successfully (reaching the bifurcation point), since the skips caused the vessel center line estimation to drift off.

While not being directly reported in the work, the image from the publication [7] depicted in Figure 4.17 clearly shows a similar geometric phenomenon with a curvy geometry along the vessel branch that is not observed in the ground truth point cloud.

The overall observed inaccuracy of the system may have several causes. Firstly, the scans included many rotations of the tip, which is prone to give more inaccurate results and showed to cause a lot of the skips that will increase the error mean, median, and variance.

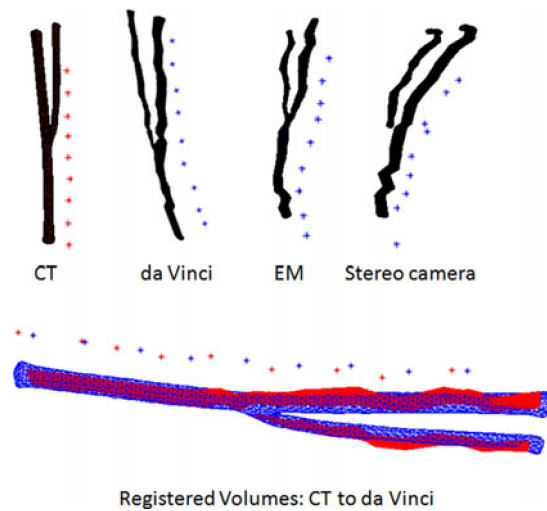


FIGURE 4.17: Vessel Scan from [7] showing 3D artifacts that could have been caused by backlash.

As the attitude signal used for the kinematic fusion still has a blind spot, as it only measures and thus updates the orientation of a single axis (measured gravity axis) but not the rotation around this axis. Secondly, due to the geometry of the probe and its attached cable coming out of the top of the handle, the probe will create a larger pull on the end-effector causing more variation. Further potential sources are tool age and usage, and the potential remaining errors due to robot calibration or mechanical backlash. To quantify the angular error of both methods, without inclusion of the reconstructed vessel, the angle difference between the obtained coordinate axes for each method and the assumed ground truth IR-tracked axes is calculated. While a strong reduction of the mean angular error and its variation from $5.48 \pm 4.64^\circ$ for pure PSM kinematics to $2.60 \pm 0.82^\circ$ for IMU-fused kinematics is notable when compared with IR-tracked orientation of z_{VP} . For the other axes, which are not directly corrected for by the fusion routine, the mean errors and double standard deviations stay in a similar range. The results for y_{VP} and less pronounced also for x_{VP} , show an improvement in mean angular error while simultaneously posing a slightly higher variation (x_{VP} : $5.81 \pm 6.13^\circ / 5.08 \pm 6.97^\circ$ - y_{VP} : $7.76 \pm 4.77^\circ / 5.90 \pm 5.94^\circ$). All three reconstruction methods, including IR-tracking, use the same visual information from the US probe and hence also the same hand-eye calibration. Therefore it makes sense to achieve kinematic errors similar to those reported for the reconstruction with $6.27 \pm 6.28mm$ for PSM-based kinematics and $3.17mm \pm 1.96$ for IMU-fused kinematics.

4.5 Conclusions

The experiments demonstrated that the proposed system for autonomous intracorporeal US scanning is capable of repeating several scans within the range of a few millimeters. The addition of an IMU proved to be valuable in determining the orientation and position with more stability, showing fewer deviations and less heavy outliers on a straight vessel scan. This is particularly apparent in the steep jumps of the trajectory using PSM-based kinematics, which disappear entirely or appear strongly smoothed with IMU-fused kinematics. The developed deep learning based method for the detection of probe tissue coupling showed to be robust and useful in adapting and maintaining a well coupled US image on a convex surface. While the results are encouraging, they still rely on the probe being placed in an initial pose in which the vessel is visible in the US image.

Concerning the integrated FSR, more rigorous tests its reliability is particularly crucial to prevent excessive forces from damaging the tissue. More experiments may also need to be carried out to assess the behaviour under different surface shapes tissue characteristics. These parameters, representing the diverse characteristics found in real tissue, are expected to have an influence on the measured contact force and thus the coupling behaviour between tissue and probe. These in turn are expected to affect the reliability of the presented approach, implying that the current conclusions are for now limited to the presented simplified bench top scenario.

From a design standpoint, however, it was ensured that the employed technology is straightforward to integrate into a realistic surgical scenario and workflow, employing vision-based solutions and only additions of small sensors with low setup requirements. In its current state, the navigation and planning is limited to a single vessel and disregards potential bifurcations and several vessel cross sections present in the US image, despite the segmentation routine already enabling the distinction between several vessel instances. The concept study compared both tested kinematics method with an IR-tracked reference assumed to be the ground truth. According to the calibration software the system imposes errors of less than $0.1mm$ after calibration. Assuming a centered vessel and good contact conditions, the mean in-plane detection of the vessel center was found to be around one millimeter accurate (95-percentile of $1.1mm$). For a more in depth evaluation of the reconstruction accuracy, particularly the influence of the image-plane to end-effector registration error, will require to perform a CT scan of the phantom with integrated fiducial markers that allow for CT-US co-registration (see [7]), which was outside of the current scope of this work.

For now this work has ignored roll adaptations in our algorithms. A good starting point for this could be the orientation with respect to the vessel center line as well. It is, however, likely that smaller vessels may not always run parallel to the surface. This problem will further be addressed in the upcoming chapters, where more anatomically realistic surface shapes will be explored.

Concerning a translation towards a clinical setup, a miniaturised probe would become necessary to allow fully minimally invasive access. In the meantime, ex-vivo experiments could give insights into potential issues and help assess the algorithms on more complex surfaces. This may eventually also involve the integration of a camera system for surface information as it will be explored in the upcoming chapters.

Chapter 5

Autonomous Marking of Tumour Boundaries

After the last chapter explored autonomous US scanning, this chapter extends the usage of the acquired anatomical information to autonomous assistance during tumour surgery. Section 5.2 outlines the technical details of the developed approach for autonomous tissue marking. Section 5.3.2 outlines experiments, starting with an US dummy with anatomical surface structure (Section 5.3.2) and subsequent feasibility experiments on an ex-vivo porcine liver (Section 5.4). Finally, the conclusion in Section 5.5 summarises the finding and puts the results in a broader context.

This chapter was submitted as the following peer-reviewed journal paper:

Marahrens, N., Jones, D., Murasovs, N., Biyani, C.S. and Valdastrri, P. "An Ultrasound-guided System for Autonomous Marking of Tumor Boundaries during Robot-assisted Surgery." *IEEE Transactions on Medical Robotics and Bionics*, under review.

5.1 Introduction

The most crucial element in resecting a tumour is isolating the entirety of cancerous tissue while sparing as much healthy tissue around it as possible. As outlined in Chapter 2, intra-operative imaging, in particular US may be used to assist in this process and alleviate some of the effects caused by the physical separation between the surgeon and the surgical site.

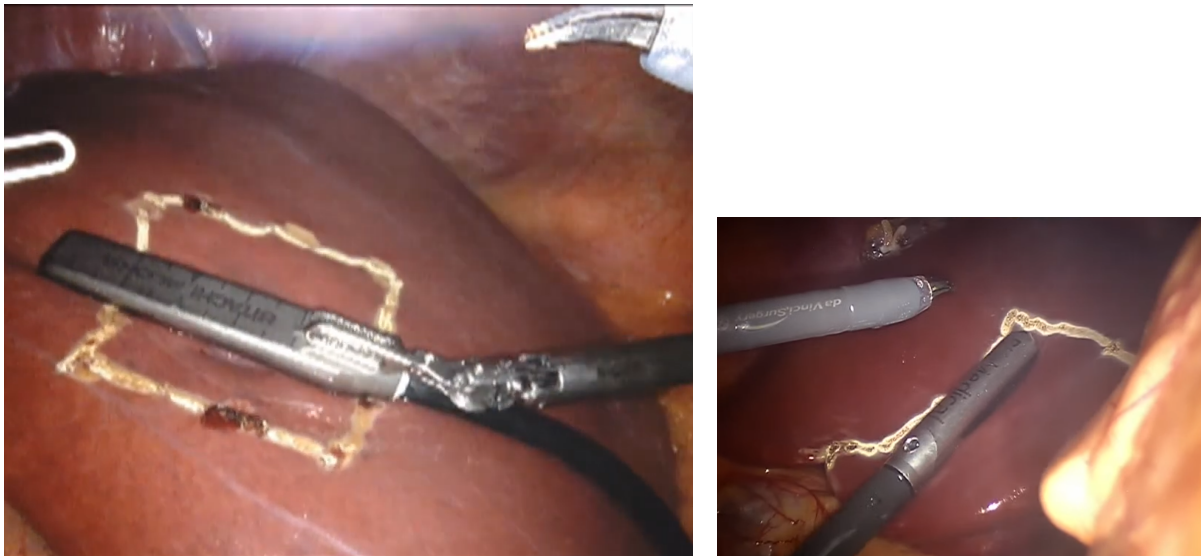


FIGURE 5.1: **Left:** Margin marking of a tumour (© 2019 MCC Gastrointestinal Oncology Video Library, Moffitt Cancer Center, Tampa, FL, USA). **Right:** Liver segment marking (© 2019 Detroit Medical Center, Detroit, MI, USA)

Despite these improvements, the intermediary process of mapping the cross-sectional US image through the visually estimated probe location with respect to the surface is bound to be imprecise since the surgeon has no exact knowledge of where the US scan lies with respect to the physical probe and its 3D location. A typical process of outlining the tumour boundary identified in the US image on the tissue surface via ES is shown in Figure 5.1. This, however, is precisely where robotic systems could excel, as they are designed to reach specific, predefined locations, conceivably even through an US scan. After performing the US scan and subsequently marking the projected margined tumor geometry onto the tissue surface, the control for the robotic system would be handed back to the surgeon for further execution of the full resection of the diseased area and further steps of the surgical procedure.

The goal of the work presented in this chapter is to realise a comprehensive approach to assisting during tumour resection and implementing the first steps towards autonomous execution, thereby providing means for improved results with smaller tumour margins. Liver surgery was chosen as a target application as ultrasound is already widely used for open surgery in this discipline and can benefit from robotic minimally invasive resection of smaller tumour masses such as very early-stage hepatocellular carcinoma [177]. It is the first to attempt this with a non-planar surface geometry in an intracorporeal, surgical robotic setting.

Recapitulating the results from Section 2.2.1, the current best alternative to intraoperative

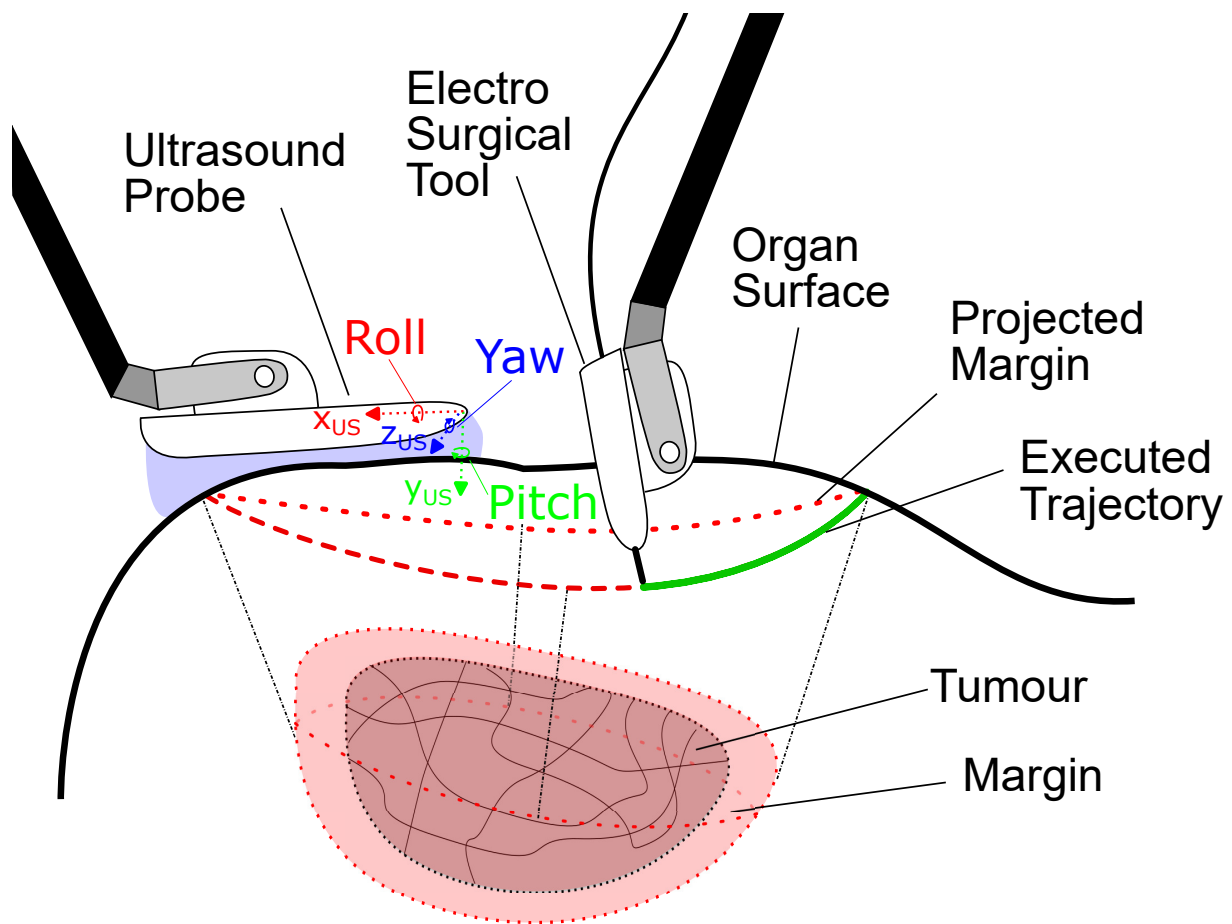


FIGURE 5.2: Concept overview: The internal tumour geometry is captured via US, projected onto the surface and eventually marked via an electro-surgical tool.

US scanning is the use fluorescent dyes such as ICG or pre-operative imaging. While dyes only provide a subsurface projection of highly vasculated areas such as the tumor, pre-operative images suffer from a potential change in the shape of the target region between pre- and intra-operative setting as well as the problem of referencing the image data to the endoscopic scene and the robotic instruments. Intracorporeal US on the other hand could solve all three of these shortcomings. As further identified in the literature review in Chapter 2 current state of the art works on autonomous intracorporeal US scanning use a planar surface, employing visual US probe and tool tracking markers and a water jet for tissue resection that does not directly contact the tissue surface. Contrary to this previous work, the method this work intends to devise employs standard ES tools and requires no visual feedback aside from the initially extracted surface point cloud, in particular, no extensive visual tracking of the tool position over time. In addition to assessing the accuracy of the approach on a phantom representing a controlled, replicable environment, the work is translated to ex-vivo tissue as the first of its kind in intracorporeal US scanning.

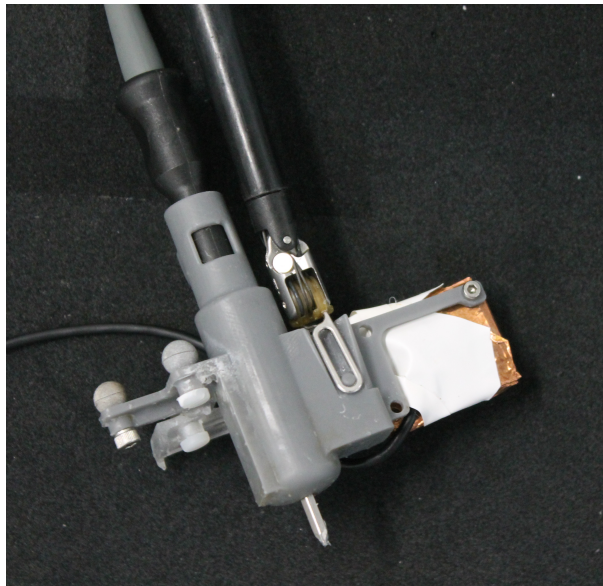


FIGURE 5.3: ES pick-up probe developed and using for ex-vivo experiments including shielded IMU

An overview over the system concept is depicted in Figure 5.2.

5.2 Materials and Methods

5.2.1 Pick-Up Design and Updated IMU Sensor Fusion

Similar to the US probe the backlash in the robotic instrument required additional consideration for any type of cutting tool that interacts with the surface and is thus exposed to external loads. Based on the previous pick-up interface designed for the US probe a robotic end-effector tool was devised that was capable of performing electrosurgery. Another reason to justify the usage of a pick-up tool was that it enabled the integration of an IR tracker, which was crucial for assessing the system's accuracy in marking the tumour projection for evaluation purposes. When doing initial testing using the ES pick-up device with integrated IMU it became obvious that the electro-magnetic fields created by the ESU were strong enough to cause the IMU signals to be disturbed and even fully interrupted. For that reason, it became necessary to fully electrically shield the IMU board (see Figure 5.3). The shielding fully prevented the adverse effects the electro-magnetic field had on the sensor and connecting cable.

With the integration of further robotic tools with IMU sensors, the IMU-PSM-kinematic fusion algorithm was further refined. To recapitulate, the approach uses the attitude sensing acquired from an IMU and updates the tool tip orientation fully based on the measured attitude. The position was, subsequently, updated by reorienting the last link of the kinematic chain.

To extend this scheme, the first three joints are now assumed to be accurately read by the kinematics, whereas the other three joints on the instrument are assumed to fully account for play and thus the need update in the fusion scheme.

The motivation for this is the fact that the first two degrees of freedom (azimuth and polar angle around the fulcrum point) are actuated in close proximity to the motor, reducing tendon length and thus complex tendon elasticity and friction. The third degree of freedom (tool insertion), in turn, is actuated by a longer tendon but sits before the coupling plate with the instrument. Since this joint, however, has no influence on the orientation of the tool tip, it will not appear in the IMU's orientational measurement. Therefore, the updated version of the previously described fusion scheme is designed to only update the last three joints of the robot, on the robotic tool.

Based on the results of Equation 4.3, the transformation of the last three joints is calculated as

$$\mathbf{R}_{l4}^{TT,fused} = (\mathbf{R}_{PSM}^{l4})^{-1} \mathbf{R}_{PSM}^{TT,fused} \quad (5.1)$$

Subsequently, this rotation's Euler angles (ZYX rotation order) are calculated. The Euler angles are set up specifically to match the three joint angles at the tip of the robotic instrument

$$\mathbf{q}_{l4-l6,fused} = \begin{bmatrix} \arctan(r_{2,1}, r_{1,1}), \\ \arctan(-r_{3,1}, \sqrt{1 - (r_{3,1})^2}), \\ \arctan(r_{3,1}, r_{3,3}) \end{bmatrix} \quad (5.2)$$

where $r_{i,j}$ is the element in row i and column j of $\mathbf{R}_{l4}^{TT,fused}$. Lastly, the three fused joint angles replace the originally measured joint angles from the kinematics in the following manner

$$\mathbf{q}_{fused} = \left[q_{l1}, q_{l2}, q_{l3}, q_{l4,fused}, q_{l5,fused}, q_{l6,fused} \right] \quad (5.3)$$

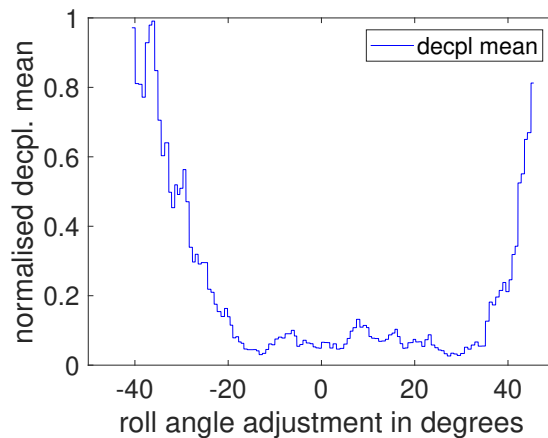


FIGURE 5.4: Normalised decoupling mean, as obtained from the DC-Net, over the performed fanning motion. Normalisation is obtained by dividing by the threshold value of 0.2.

where \mathbf{q}_{l1} to \mathbf{q}_{l3} are the joint angles of the first three joints, directly obtained from the robot joint measurements, and $\mathbf{q}_{l4,fused}$ to $\mathbf{q}_{l6,fused}$ are the fused joint angles from the previously presented update rule. Plugging these newly obtained, fused joint angles into the direct kinematics equations

$$\mathbf{x} = f(\mathbf{q}_{fused}) \quad (5.4)$$

to obtain the updated forward kinematics pose (tooltip position and rotation) from the updated joint angles. The updated position allows us to account for the PSMs mechanical play and compliant design, enabling more precise US scans.

5.2.2 Surface Normal Estimation

Navigation along a non-planar surface structure is not trivial. Previously, roll adaptations were ignored for Chapter 4, the transition towards an anatomical surface structure that was curved in various directions made it necessary to treat this further. While position, pitch, and yaw can all be determined through the US image, this is not the case for the roll angle (see Figure 5.2 for roll, pitch, and yaw correspondence). Adapting the roll angle usually requires knowing the surface normals to move the probe tangentially to the surface.

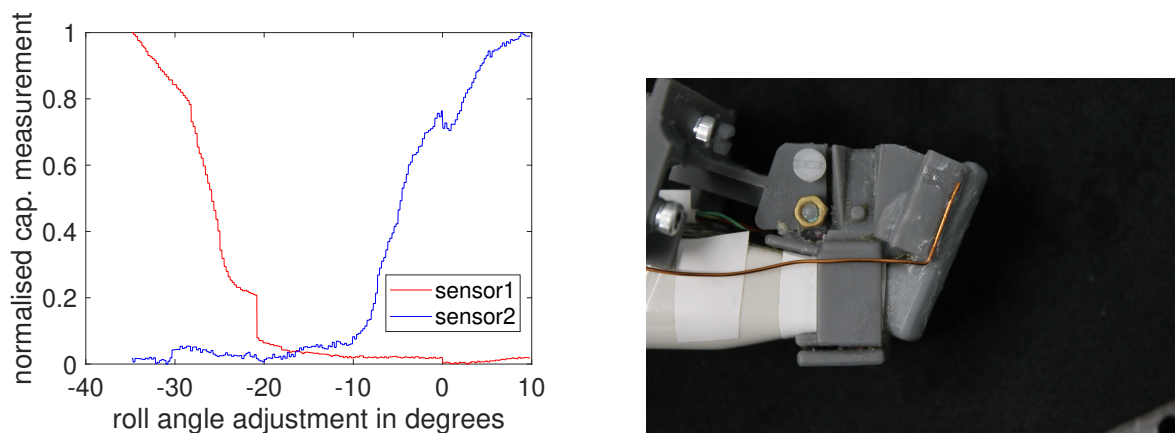


FIGURE 5.5: **Left:** Plot of the measure signal of the capacitive sensors on either side of the US probe. **Right:** Capacitive sensor attached to the US probe in an attempt to detect and control the probe orientation relative to the tissue

Initially Investigated Concepts

Initially, the idea was to assess approaches relying on the US image and potentially simple sensor solutions to ensure adequate roll orientation. Therefore, I first investigated the possibility of applying fanning motions to detect the current surface normal. Similar approaches were used in [178] using force measurements and US confidence maps. In this probe was turned around its roll axis until the coupling quality degraded significantly (mean above 0.2) and then turned in the opposite direction. The values obtained were then normalised with the threshold value to obtain a normalised decoupling mean for further evaluation. This way a spectrum of orientations was determined with the reasonable assumption that the mean of this spectrum should lie close enough to the actual surface normal. While this approach was found to work, it revealed itself to be impractical for arbitrary surfaces and it would need to be repeated several times over. Furthermore, the range in which mean decoupling was detected to be low, was quite large, meaning extensive movements of up to 100° and thus quite time-consuming in themselves. Figure 5.4 depicts a typical profile of the normalised coupling quality over a fanning motion.

A second approach that was investigated was the use of capacitive sensors attached to the side of the ultrasound probe. The idea was that by measuring the capacitance on both sides of the probe it would be determined if either side was in better or worse contact. The developed sensor setup is shown in Figure 5.5 on the right. The left shows a well perceived change in capacitance over a fanning motion. Unfortunately, this solution was found to be highly sensitive to liquid attaching to the sensor surface. This can and does usually happen when the probe get in direct touch with the tissue, vastly changing

the baseline capacitance, changing the overall profile of the perceived capacitance over a fanning motion. Therefore, this solution was also deemed unworkable.

3D Point Cloud and Surface Normal Estimation

As a third option, the surface normals were estimated using a stereo camera. Despite it being a less favourable approach in the context of MIS due to the additional setup required and the necessity to co-register the camera with the robot, it is a common approach in extracorporeal US. Furthermore, previous works in the context of RAMIS have already used this information to automate specific tasks, such as tissue retraction [32].

In the setup developed as part of this work, the surface geometry is extracted using a stereo camera (Intel Realsense 405d, Intel Corporation, Santa Clara, CA, USA), analogous to a stereo endoscope. The camera was placed at a distance of roughly 13cm from the surface to account for the larger lens disparity compared to an endoscope. The average point distance was downsampled to 3mm for the phantom surface to filter outliers, and the closest point on the surface was found by interpolation. To calculate the surface normal, the algorithm performs a PCA with all points within a 10mm radius around the found point. For hand-eye calibration, ArUco markers are attached to the 3D-printed frame used for IR tracking and arm co-registration. Using the mesh from the phantom mold CAD model as ground truth, the mean angle error of the normal vectors extracted from the point cloud are calculated to be around 4.63° with a maximum error of 16.95° that was mainly observed on the edges of the phantom. The mean and root mean square errors were 0.16mm and 0.91mm , respectively.

5.2.3 Modified Electrosurgical Unit

The original intention of the project was to use a novel US cutting probe, capable of quantifying the contact with the tissue. A prototype of the probe, however, was not yet available at the time of this writing. Therefore, I investigated means to achieve a similar workflow with a standard ESU that could then eventually be easily translated onto an US cutting device. Similar to ES, US tools also provide cutting and coagulation and can be tuned by modulating the electric signal fed to the piezo element. The dimensions of the pick-up interface were directly taken from the initial casing for the US pick-up tool.

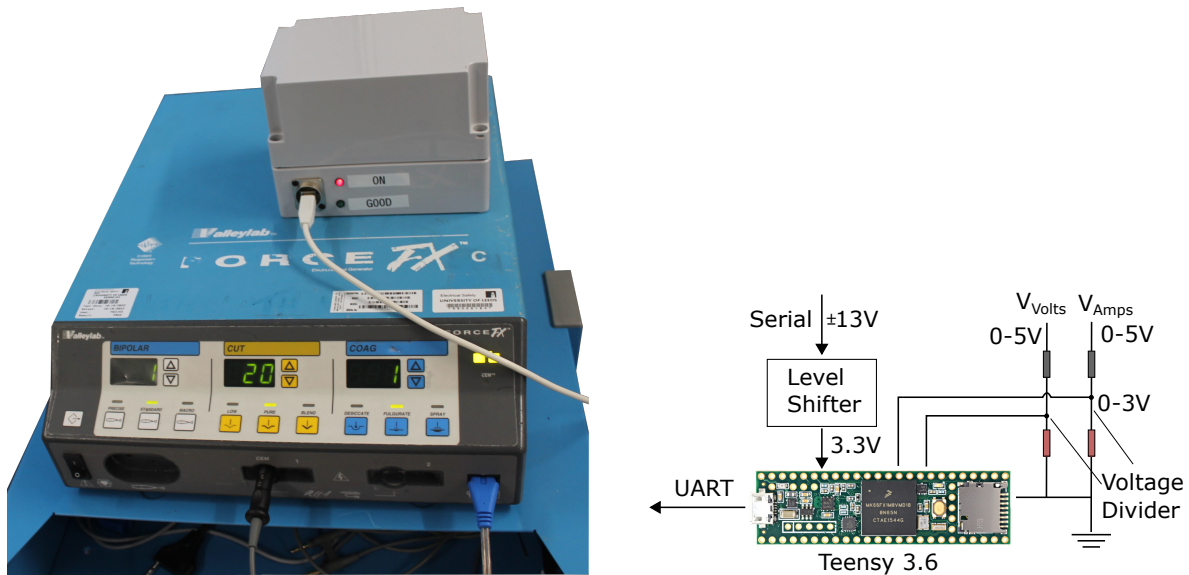


FIGURE 5.6: **Left:** ESU with custom built data extraction box **Right:** Schematic circuit diagram for data extraction box.

The main principle behind electrosurgery is that a high frequency (commonly between $0.3MHz$ and $5MHz$) electric current is injected into the tissue that results in the local denaturation of tissue cells [179]. While lower current frequencies (below $1kHz$) may induce neuromuscular stimulation that can even severely affect the heart beat up until the patient's death, this effect becomes negligible at frequencies above $100kHz$ to $300kHz$ [179]. Depending on the type of electrosurgery, the return electrode is either provided by the instrument itself (bipolar electrosurgery) or by a return electrode connected to the patient that is spread throughout a larger area on the patient body (monopolar cautery).

For further investigation of the contact detection, I modified a commercially available ESU (Valleylab Force FX-8, Medtronic plc, Minneapolis, MN, USA). The system includes two DB-15HD ports at the back capable of providing real-time data from the system. To use this data, the signals are fed from both ports into a Teensy 3.6 (PJRC.COM LLC, Sherwood, OR, USA) that processes the data and then publishes it into the ROS environment (see Figure 5.6).

Since the dVRK does not offer reliable force estimation as explored in Chapter 4, further measures are needed to ensure proper contact of the tooltip with the tissue surface. An integration of an FSR seemed inappropriate in this case as opposed to the US pick-up probe where the sensor could be simply placed between the commercial probe and the 3D printed pick-up interface. Additionally, it would not have been easily miniaturisable to

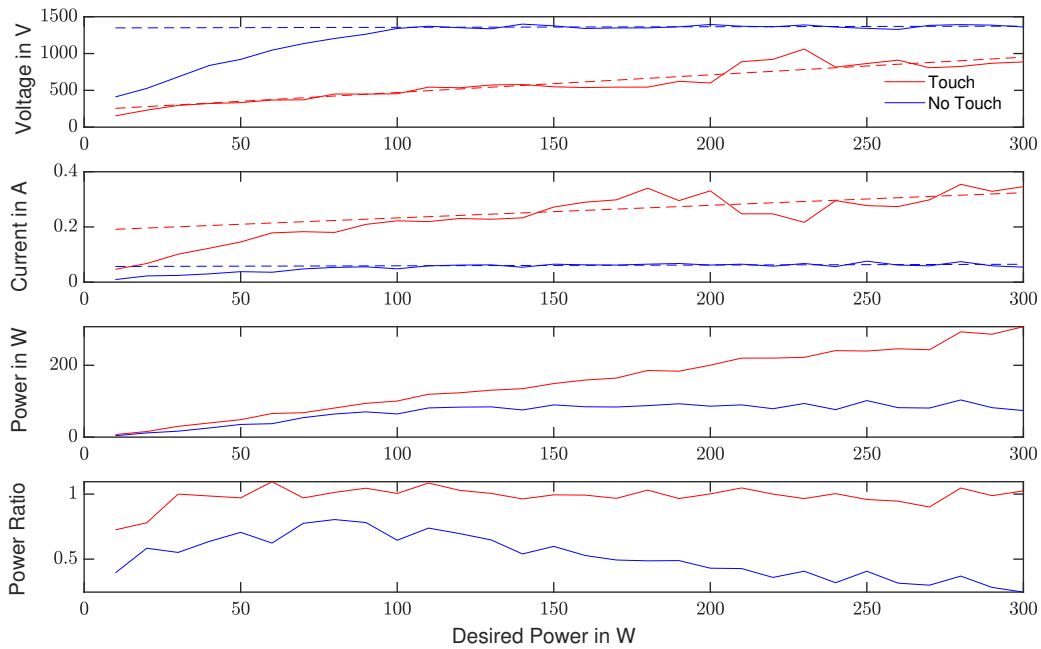


FIGURE 5.7: Measured output signals over different desired power settings and for contact and non-contact settings.

eventually fit inside a surgical robotic tool such as the FBF. Previous research has already looked at using the da Vinci tools to estimate tissue impedance [180]. Similarly, the impedance of the instrument changes once contact with the tissue surface is established. While the ESU's internal controller will try to reach target values for current and voltage, it might not always be feasible; if there is no contact with the tissue surface, a voltage difference can be created, but the current flow will be prohibited. Consequently, the power output P_{out} will vary.

$$P_{out} = U \cdot I \quad (5.5)$$

where U and I are the measured voltage and current, respectively.

The goal is to apply as little force to the surface as necessary but establish enough contact to maintain a clean mark. In order to control the instrument, the output over the desired power ratio are calculated

$$r_P = \frac{P_{out}}{P_{des}} \quad (5.6)$$

When contact is lost, the average achievable power will be significantly lower. Figure 5.7 show the ratio over different desired output power settings. This is an observation that will be used to control the probe. To adjust the contact, the PSM lifts the probe off away from the surface until contact is lost before reapproaching the surface until contact is restored.

5.2.4 Ultrasound Tumour Scan

For detecting features in the US image, the previously described U-Net is employed [50] along with the custom-built deep neural network to estimate the coupling quality between the US probe and the tissue surface based on the US image. The details of these can be found in Section 4.2.3 to 4.2.4. To ensure the probe is not applying excessive pressure, the robot slightly lifts the probe off the surface as it moves. As soon as the probe detaches from the tissue surface, the contact detection sets in and slightly adjusts the probe position towards the surface. In this manner, the system can autonomously scan without requiring the additional force sensor employed in the previous chapter

Initially, the probe is assumed to be at a location in the approximate vicinity of the tumour and propagates along the image normal axis. Once a tumour is detected, it is centered in the image while continuing to move in the image normal direction. Once the probe has passed the tumour, the current centroid of the point cloud is calculated and used to determine the center of rotation on the tissue surface. Subsequently, the probe is rotated by 30° and propagated back towards and across the tumour. Lastly, this is repeated a second time with a 60° angle compared to the initial position. Three scans were found to generally be sufficient to create varying point clouds from different angles. Furthermore, 30° and 60° were chosen to allow for varying angles while reducing the risk of the robot running into joint limits. Note that for ex-vivo experiments, the system only relied on a single scan as tissue movement caused significant differences between the scans.

5.2.5 Trajectory Generation

According to feedback from surgeons at St. James's University Hospital in Leeds, there is no standardised way to project the internal 3D tumour geometry onto the surface. This may primarily depend on the eventual goal of the resection. If the goal is to resect a liver segment or lobe, a direct upward projection with the same vector for every point may

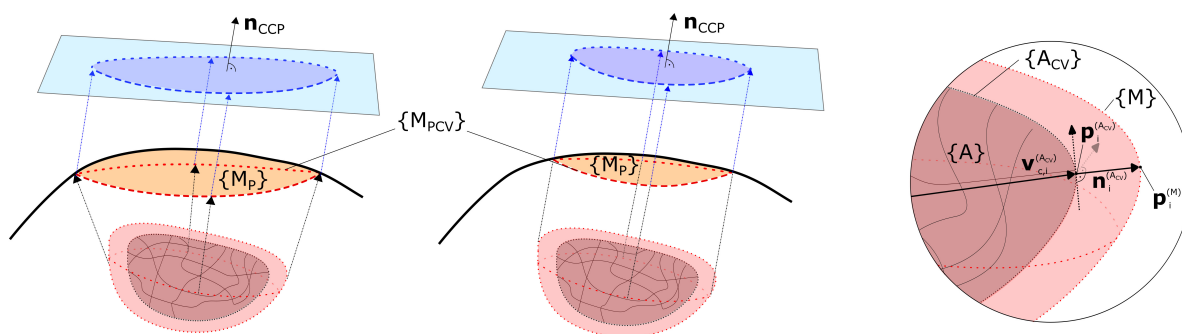


FIGURE 5.8: Comparison between different projection methods. **Left:** DPP using the same vector to project each point to the surface. **Center:** CPP using the closest point as surface projection. \mathbf{n}_{CCP} marks the surface normal plane at the surface point closest to the centroid of the tumour. A clear difference can be observed in the size of the different projections both on the surface marked as red contours $\{M_{PCV}\}$, as well as on the projected outline on \mathbf{n}_{CCP} plane. **Right:** Zoomed in view showing the different point sets and vector quantities involved in the calculation of the margin, in particular the surface normal $\mathbf{n}_i^{(A_{CV})}$ and surface point $\mathbf{p}_i^{(A_{CV})}$.

be desirable (DPP). This, however, may not be practical for an actual resection since a cylindrical cut-out is usually not feasible. In these cases, it may be desirable to project the internal geometry to its closest point on the surface (CPP). This may be seen as a greedy optimisation for minimum resection volume by minimising the distance of each point to the surface, while also creating a more realistic resection volume (e.g., in the form of a wedge). The difference between the two methods becomes further exacerbated depending on the surface structure. In the following, the surface is assumed to be either planar or convex since this primarily reflects the general surface structures accessed around gastrointestinal organs such as the liver or kidney. While for a planar surface, the two projection methods might be almost identical, this may not be the case if the shape of the surface is convex. In these cases, the CPP will result in a larger projected area. The difference between the two methods is further depicted in Figure 5.8 with the formulas used for plane projection are defined in Appendix A.3. An overview over the entire trajectory generation pipeline from surface scan acquisition until eventual execution is outlined in Figure 5.9

To marginalise the tumour, the outer surface needs to be found. In the following, it is assumed that the tumour is relatively round and without major concave surface regions. In this case, finding the outer surface reduces to finding the convex hull, for whose calculation numerous methods exist. The convex hull, referred to as $\{A_{CV}\}$, is the smallest convex set of points that encloses all other points within it. For calculating the convex hull, the Quickhull algorithm provided by Scipy is used [181]. Once the set of points $\mathbf{p}_i^{(A_{CV})}$ of the convex hull $\{A_{CV}\}$ is found, the centroid $\mathbf{p}_c^{(A_{CV})}$ of the resulting surface is determined.

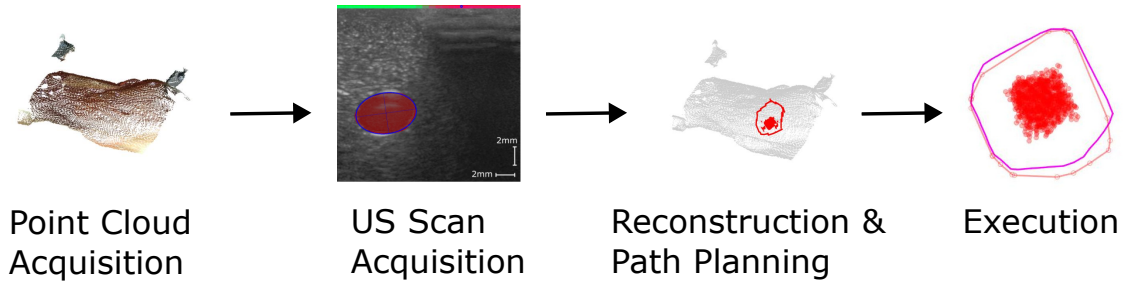


FIGURE 5.9: Overview over the Pipeline: 1) A surface point cloud is extracted from the real sense and referenced to the robot via Aruco markers 2) Based on the surface information, a scan is acquired 3) The 3D geometry is projected onto the surface using one of the two suggested methods 4) The planned path is executed on a second robotic arm

Then the normal vector pointing away from the contour for each convex hull point is calculated. This is achieved by considering the vector connecting the centroid to each convex hull point. Since the centroid needs to lie within the contour, it can be expressed as a linear combination of the surface tangent and normal at that point. Consequently, the connecting vector from the centroid to point i of the convex hull as can be defined as

$$\mathbf{v}_{c,i}^{(ACV)} = \mathbf{p}_i^{(ACV)} - \mathbf{p}_c^{(ACV)} \quad (5.7)$$

This method further guarantees that the fraction in the normal vector direction always points outwards, away from the contour. The algorithm starts by calculating the two tangent vectors $\mathbf{t}^{j,0}$ and $\mathbf{t}^{j,1}$ of each simplex that point $p_i^{(ACV)}$ is part of

$$\mathbf{t}_{j,k}^{(s_j)} = \frac{(\mathbf{p}_{k+1}^{(s_j)} - \mathbf{p}_k^{(s_j)})}{\|\mathbf{p}_{i+1}^{(s_j)} - \mathbf{x}_i\|} \quad (5.8)$$

where $k = \{0, 1\}$ and $\mathbf{p}_k^{(s_j)}$ is the k^{th} point of simplex s_j . This leads to a simplex normal $\mathbf{n}_{i,k}^{(s_j)}$ at point i via the following formula

$$\mathbf{n}_{j,k}^{(s_j)} = \mathbf{v}_{c,i}^{(ACV)} + \mathbf{t}_{j,k}^{(s_j)} \left(\left(\mathbf{t}_{j,k}^{(s_j)} \right)^T \mathbf{v}_{c,i}^{(ACV)} \right) \quad (5.9)$$

The normal \mathbf{n}_i for each point is then inferred by calculating the average over-all simplex face normal. Finally, the set of points $\{M\} = \mathbf{p}_i^{(M)}$ defining the margin is calculated by updating each point with its scaled surface normal vector

$$\mathbf{p}_i^{(M)} = \mathbf{p}_i^{(ACV)} + d_m \mathbf{n}_i^{(ACV)} \quad (5.10)$$

with d_m being the desired margin.

To infer the trajectory on the surface, all points in $\{M\}$ are projected up onto the surface using one of the previously outlined methods, resulting in $\{M_P\}$. Next, all points are identified on the outer edge of the projected points. For this, all points $\{p_i^{(MP)}\}$ are projected onto the surface normal plane at the point closest to the centroid P_c . In the planar projection, all points in $\{M_P\}$ that are part of the convex hull in the planar projection are again determined, resulting in the final set of points $\{M_{PCV}\}$ making up the surface trajectory. This process is further depicted in Figure 5.8.

5.2.6 Control Scheme

While the IMU on the US probe is predominantly used to determine the correct location of the US scan, the IMU on the marking tool feeds back into a controller to adjust the probe location. For this, a Proportional-Integral (PI)-controller is implemented that provides an updated cartesian position to the dVRK software framework in the form

$$\mathbf{x}_{des,i+1} = \mathbf{x}_{traj,i+1} + \mathbf{K}_P \underbrace{(\mathbf{x}_{traj,i+1} - \mathbf{x}_{meas,i})}_{\Delta \mathbf{x}_{ctrl,i}} + \mathbf{K}_I \sum_{k=0}^{k=i+1} \underbrace{(\mathbf{x}_{traj,i+1} - \mathbf{x}_{meas,i})}_{\Delta \mathbf{x}_{ctrl,i}} \quad (5.11)$$

where $\mathbf{x}_{traj,i}$ describes robot pose at the i^{th} time step as output by the planner and $\mathbf{x}_{meas,i}$ describes the pose as measured by IMU-fused kinematics. \mathbf{K}_P and \mathbf{K}_I , in turn, are diagonal matrices defining the gains for updating the components of $\Delta \mathbf{x}_{des,i}$. Each trajectory starts by moving the end-effector at a safe distance of $10mm$ from the surface. The controller is then initialised by slowly adapting $\Delta \mathbf{x}_{ctrl,i}$ along with the end effector pose until root squared error for position and orientation are below $0.75mm$ and 0.25° , respectively. After that, the tools starts approaching the tissue surface until a contact is detected and then starts moving along the trajectory on the surface. During the following, the instrument is gradually and slightly lifted off the surface. After a $3mm$ ($10mm$ for ex-vivo) distance, the contact is adjusted futher. For this, the PSM lifts the instrument off the surface until the contact is lost, if necessary, and then re-approaches it. This way, a saw-tooth motion is achieved that prevents the marking tool from getting stuck inside the tissue and minimises contact forces. Since the main objective is to marking the surface,

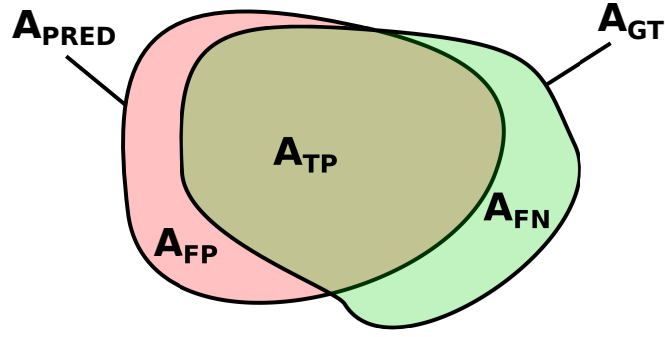


FIGURE 5.10: Different areas used in the calculation of metrics.

ensuring contact every $3mm$ is sufficient to outline the contour, as the ESU will also mark the tissue surface if slightly above the surface.

5.3 Phantom Experiments

5.3.1 Metrics

To compare the different scans on the tissue surface, both the IR-tracked and the predicted point cloud are projected into the same tangential plane. Using the ground truth mesh, the tangential plane at the point closest to the IR-tracked centroid is chosen.

For the assessment of the projections in this plane, the True Positive Rate (TPR) r_{TP} , also referred to as sensitivity, or equivalently the False Negative Rate (FNR) $r_{FN} = 1 - r_{TP}$, also known as miss rate, as well as the False Discovery Rate (FDR) r_{FD} are considered. Based on the areas outlined in Figure 5.10, they are defined as follows:

$$r_{TP} = \frac{A_{PRED} \cup A_{GT}}{A_{GT}} = \frac{A_{TP}}{A_{GT}} = 1 - r_{FN} \quad (5.12)$$

$$r_{FD} = \frac{A_{GT} - A_{TP}}{A_{GT}} = \frac{A_{FN}}{A_{GT}} \quad (5.13)$$

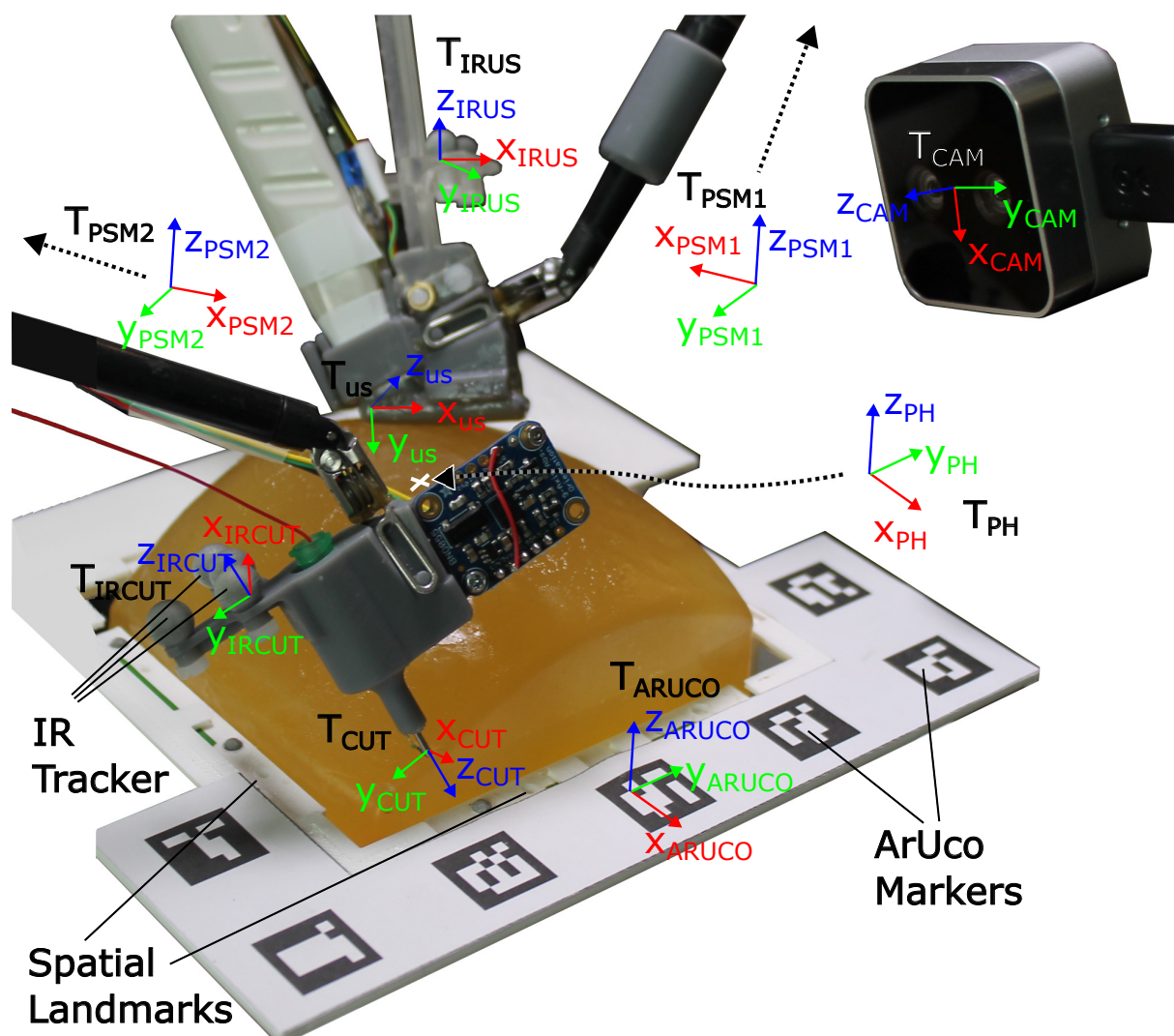


FIGURE 5.11: Overview of setup and frames used. \mathbf{T}_{PSM1} and \mathbf{T}_{PSM2} sit at the fulcrum point of each PSM, while \mathbf{T}_{PH} is located at the center of the US phantom. \mathbf{T}_{CUT} and \mathbf{T}_{US} are the tooltip frame for the marking tool and US probe respectively, along with the tool-attached IR tracking frames \mathbf{T}_{IRCUT} and \mathbf{T}_{IRUS}

5.3.2 Ultrasound Phantom Design

In order to develop and assess the system under controllable conditions, an US phantom was designed, keeping in mind a final application. For the design and subsequent experiments, the following assumptions were made: (1) tumour masses are relatively small in diameter ($d < 20mm$), such as very early-stage Hepatocellular carcinoma (HCC) [177]. It is also assumed that the tumours are (2) relatively round and (3) lie closely below the surface (starting around 5 – 10mm from the organ surface). The last assumption is

necessary for a minimally invasive resection to make more sense than performing a full lobectomy.

To provide a realistic chance of translating results from the lab bench to an ex-vivo organ, the curved surface geometry of a CT liver scan was extracted and then integrated into a mold with a support surface of $95 \times 95 \text{mm}$. The gelatin-water ratio was chosen to make the tissue phantom as soft as possible while maintaining mechanical properties similar to those of real tissue. The precise phantom composition is attached in Appendix A. For the tumour masses, $15 - 18 \text{mm}$ hydrated Polyacrylamide (PAM) beads were used that, due to their acoustic properties relative to the gelatine, make them appear as dark areas in the US slices. Unfortunately, presumably due to the applied heat during phantom production, the masses' diameter seem to reduce by $2 - 3 \text{mm}$. The final phantom can be seen in Figure 5.11.

5.3.3 Phantom Trajectory Generation

Three phantoms with identical surfaces were cast and a single mass was placed in each, varying its locations. The masses were placed at the opposing lower ends of two phantoms and close to the peak on the third. In total five repetitions were run on each of the three masses, making 15 distinct scans. For each scan the trajectory was calculated for further evaluation. To begin with, the probe was set at a random location around the tumour, before the scanning procedure was run as outlined in Section 5.2.4. Once the scans were acquired, the results were processed, calculating the direct and closest point projections.

The results of the 15 scans are outlined in Table 5.1. The TPR for both methods lies around 0.9, slightly above these values for CPP and slightly below for DPP. Similarly, the FDR for both methods is comparable, yet slightly lower for the CPP. All employed coordinated frames are depicted in Figure 5.11. Furthermore, the mean standard deviation of all runs is again slightly lower for the closest point method. The higher robustness may be explained by the fact that the projection vector is calculated individually for each point rather than based on a single estimate of the connecting vector between the mass centroid and its closest point. Exemplary results for both projection methods are shown in Figure 5.12.

When comparing the 3D scans, the average distance between the projected scan centroids was found to be $3.2 \pm 1.4 \text{mm}$. This number agrees with the shift of the radius of the margined mass (15mm diameter plus twice the 7.5mm margins) that also accounts for

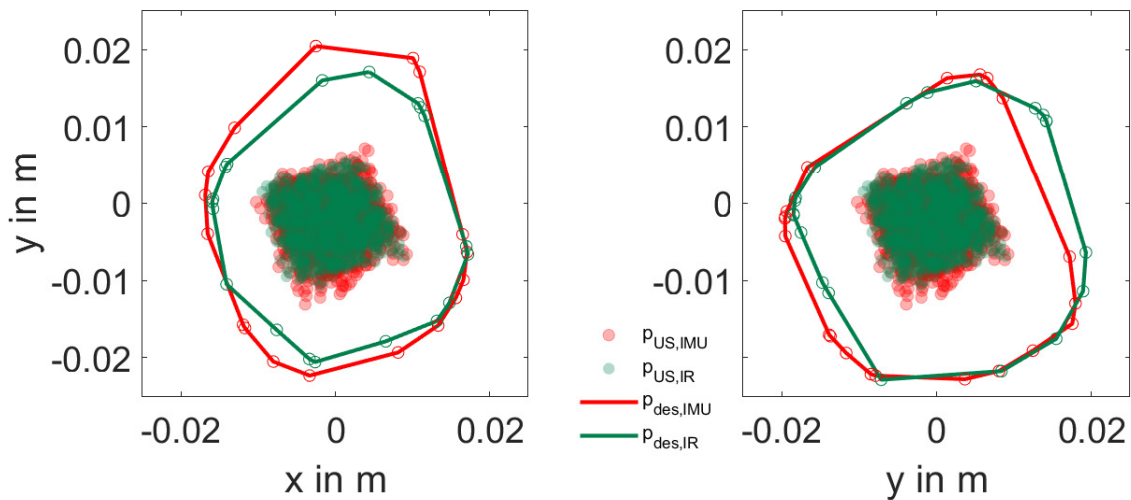


FIGURE 5.12: **Left:** Centroid Projected Scans. **Right:** Closest Point projection

TABLE 5.1: True Positive Rate (TPR), False Negative Rate (FNR) and False Discovery Rate (FDR) for the two different projection methods: Direct Point Projection (DPP) and Closest Point Projection (CPP)

Method	r_{TP}	r_{FD}	r_{FN}
DPP	0.879 ± 0.059	0.151 ± 0.088	0.121 ± 0.059
CPP	0.907 ± 0.036	0.148 ± 0.060	0.093 ± 0.036

roughly 10%. Similarly, a 10% reduction in the TPR is observable. While this error is likely caused by the inaccurate kinematics of the PSM, even after IMU fusion, another potential source of error might be the grid size of the extracted point cloud. Currently, this is limited to a grid of $3mm$ average distance, which is used for closest point interpolation.

Comparing the inferred trajectory against the convex hull of an unmarginated tumour, an overlap of 0.992 is achieved. Only in two cases did the convex hull slightly cross the ground truth tumour outline. Since the inaccuracies are not expected to scale up with margin size, this may be expected to vanish for a larger margin of e.g. $10mm$.

5.3.4 Phantom Marking

Based on the results of the trajectory generation, CPP was selected for further investigation since it resulted in a higher TPR, a slightly lower FDR, and a lower variance. However, the results of the execution are expected to be translatable to arbitrary surface trajectories, regardless of the projection method. Since the gelatine phantom melts under electrosurgery, the phantom marking was simulated using a dummy device (see

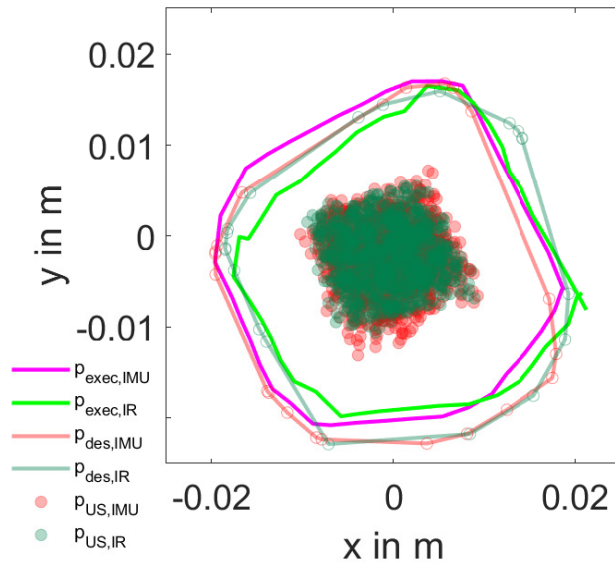


FIGURE 5.13: Execution of the marking on the tissue surface

Figure 5.11). Rather than applying actual power and measuring the power-out-ratio, the pick-up tool integrates a capacitive touch sensor that is thresholded to generate a binary signal (touch / no touch) comparable to the thresholded power output signal of the ESU. The top surface of the US phantom is further covered up with a Low Density Polyethylene (LDPE) film to prevent the probe from poking through the surface. This also allowed it to repeat the execution several times without altering the phantom surface. To produce a clearer change in the capacitive signal, the LDPE film was coated with US gel.

Similarly, for the surface trajectories generated from the US scans, the overlap between the executed circular trajectory and the IMU-generated trajectory is compared, using the calculated ground truth normal plane for projection. To calculate the overlap between the executed and the inferred or ground truth trajectory, the downsampled execution trajectory to only the points where the probe is initiating contact with the tissue surface. This resulted in a roughly 3 – 5mm spacing and ensured the trajectory points lay on the surface.

The controller provided good tracking with a mean error norm and mean error norm variation of $0.54 \pm 0.30\text{mm}$ and $0.7 \pm 0.53^\circ$ between the desired and executed IMU trajectory over all 15 runs and for position and orientation, respectively. The positional error $e_{des,IMU,j}$ and orientational error $\Delta\theta_{des,IMU,j}$ for run j with N time steps was calculated as follows

$$e_{des,IMU,j} = \frac{1}{N} \sum_{i=0}^N \sqrt{(p_{des,i} - p_{IMU,i})^T (p_{des,i} - p_{IMU,i})} \quad (5.14)$$

$$\Delta\theta_{des,IMU,j} = \frac{1}{N} \sum_{i=0}^N \arccos(|z_{US,des}^T z_{US,IMU}|) \quad (5.15)$$

and then mean and standard deviation calculated over all runs.

Overall, the mean positional error between the projected trajectories for ground truth (IR) and IMU was $3.4 \pm 0.7mm$. This resulted in an overlap (TPR) of 0.875 ± 0.035 with the inferred area. FDR was found to be 0.135 ± 0.058 . Both values are similar to the ones found for the 3D projection. Figure 5.13 shows exemplary results of an executed marking.

5.4 Ex-Vivo Feasibility Test

To assess the approach under more realistic conditions and to test the proposed control scheme with an actual ESU, both previously tested routines were also performed on an ex-vivo porcine liver. In preparation, a small pocket was cut into the side of the liver, through which a hydrated PAM bead was inserted, representing a dummy tumour mass. The mass had similar dimensions (around $15mm$ diameter) to the ones previously used for the phantom study.

Similar to the phantom, the IR tracking system as well as the stereo camera was co-registered using spatial landmarks and ArUco markers. Figure 5.14 shows the setup for the ex-vivo trials, consisting of a polymer box for liquid retention and contamination prevention. Inside the box, a laser-cut frame holding the 3D-printed platform was fixated that contained all spatial landmarks to co-register PSM, stereo camera and IR tracking. On the bottom of the container the ground electrode of the ESU was placed, covered with folded cloths soaked in saline, with sufficient osmolarity to match the required electrical impedance for the ESUs safety mechanism. In addition to electrical conductance and impedance matching, the cloth ensured sufficient friction to prevent the liver from slipping during scanning and marking.

At first, the liver was scanned with the stereo camera. For the experiment the point cloud was assumed to be static and was not updated during scanning or marking. For hand-eye calibration, the aforementioned ArUco markers were attached to the 3D-printed frame

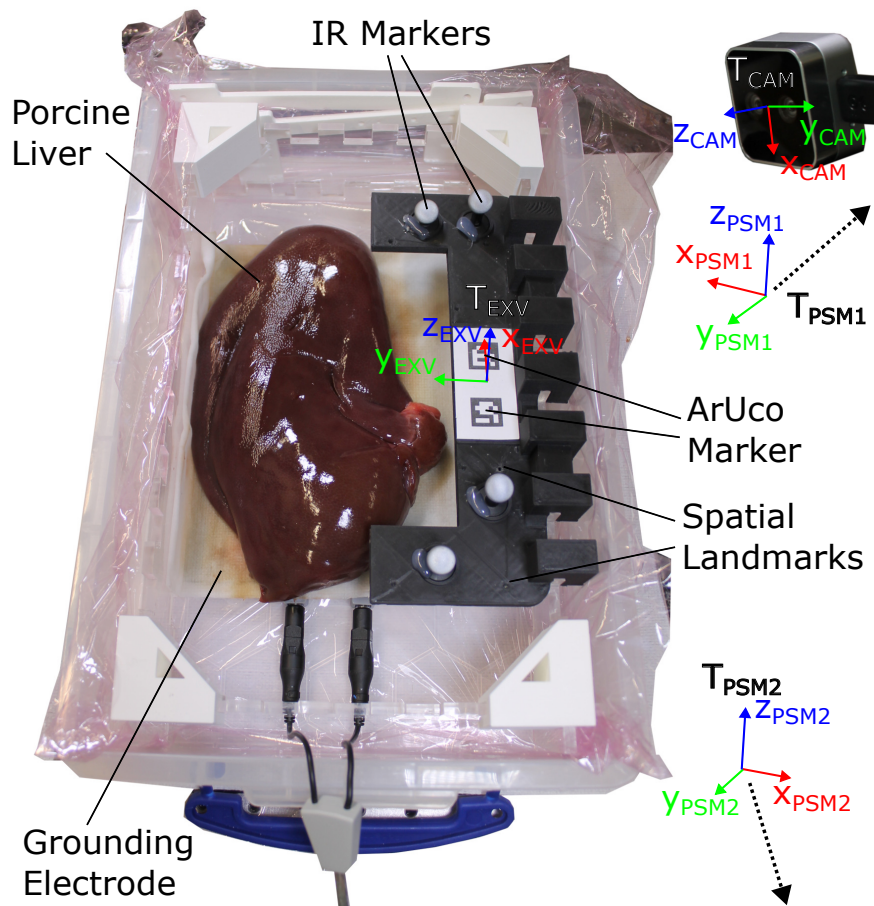


FIGURE 5.14: Experimental setup for ex-vivo trials, including frame with ArUco markers, IR-trackers and defined coordinate reference frames.

used for both IR tracking and arm co-registration. To ensure that the ArUco markers were visible in the camera frame as well as the whole liver, the distance between the camera and surface was adjusted to 165mm , slightly further than for the phantom, giving a more robust reconstruction of the surface structure and considerably less noise. One possible explanation for this is that the liver surface contains more fine features than the relatively shiny and structureless gelatine surface. Additionally, this allowed it to decrease the point cloud grid size to 1mm .

Equivalent to the phantom study, the probe was placed at a random location around the tumour with the US image plane normal pointing towards the phantom. After performing the scans, the projections were calculated; again choosing CPP. Lastly, the surface of the liver was marked. For further validation, a further 3D scan of the surface using the stereo camera were performed. Using black ink, the trajectories were dyed for enhanced contrast. Figure 5.15 shows the colour thresholded point set marked as blue dots p_{post} . This allowed it to perform colour thresholding on the 3D point cloud to extract the marked

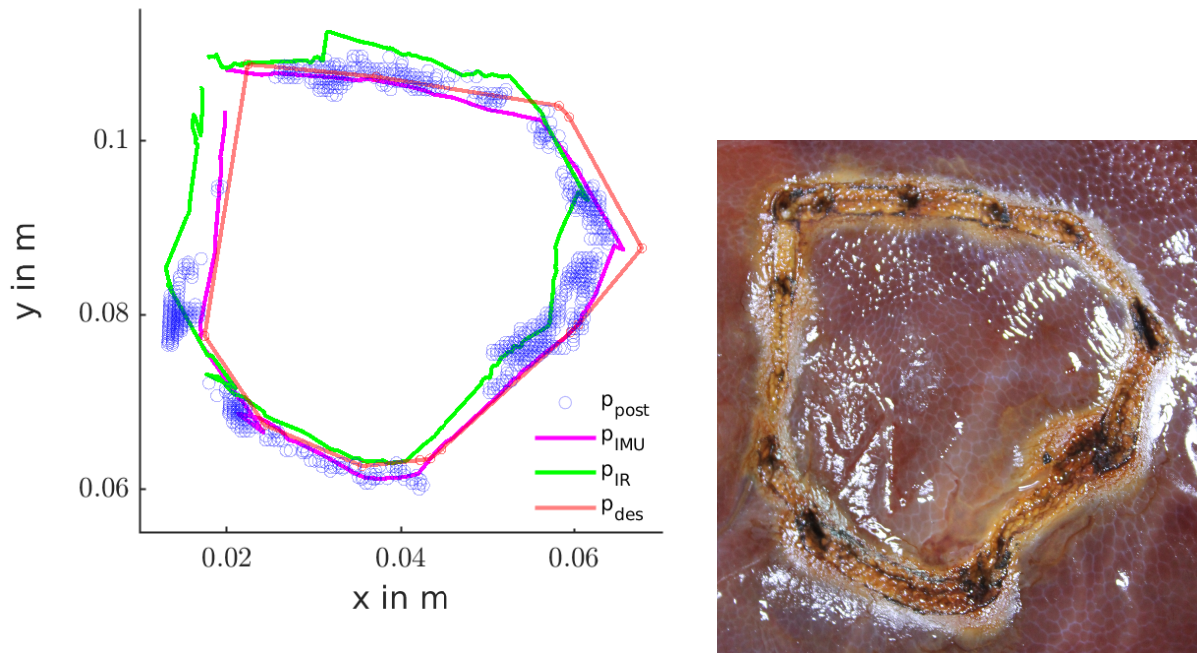


FIGURE 5.15: **Left:** Ex Vivo 3D results including point cloud. **Right:** Marked profile on the liver surface

path directly from the surface scan. Aside from the previously employed kinematic data, this provided further means to assess the system's accuracy under these conditions.

Assessing the scan projection before execution, the TPR is determined to be 0.844 and the FDR to be 0.119, comparable to those observed in the phantom study. Note, however, that as opposed to the phantom study, both projections were referenced against the same point cloud, as no ground truth point cloud was available. Looking at the execution, the TPR is calculated at 0.905 and the FDR to be 0.130 when compared against the control input trajectory. Similarly, the TPR compared to the ground truth trajectory was 0.863, with an FDR of 0.133.

Figure 5.15 shows the results of the marking. The width of the mark left by the instrument was measured to be around 4mm . The points at which the impedance adjustment occurred are clearly visible, marked by slight carbonisation and a deeper insertion into the tissue. The rest of the mark looks relatively even. Furthermore, the picture of the ESU marking in Figure 5.15 clearly shows fully closed contour, indicating a good alignment between the start- and end-point.

Looking at the extracted trajectories, a relatively good match with the planned and executed trajectories can be observed (see Figure 5.15). Figure 5.16 further shows the

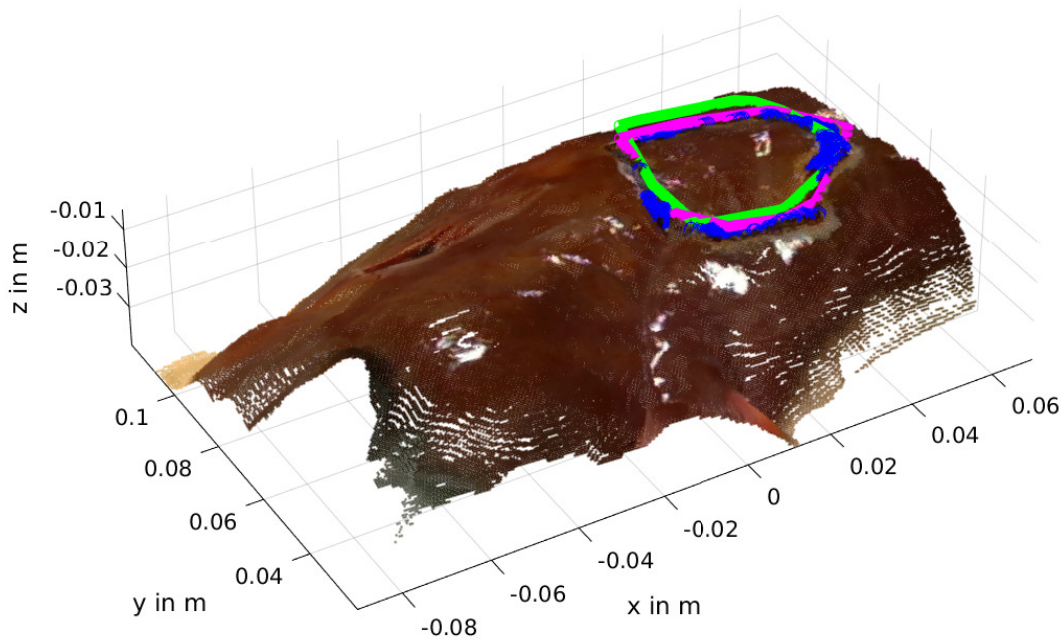


FIGURE 5.16: 3D point cloud of ex-vivo liver, overlaid with the different trajectories corresponding to Figure 5.15

overlay of these trajectories in 3D space. Looking at the IR-tracked trajectories, the TPR and FDR are calculated at 0.905 and 0.129 respectively, for this single run, when compared to the input trajectory.

The distance between the centroid of the two tumour point clouds is 6.1mm . This is significantly higher than the results of the tumour study. A major reason for this may be the more flexible structure of the ex-vivo tissue, causing the tumour to move more under applied forces exacerbating already existing inaccuracies and potentially complicating the visual segmentation task.

Tumor scanning and marking together took around 3min , with over 80% of that time being taken up by the marking. Considering an overall reported median time of 360min for a minor hepatectomy [182], the overall time this assistive procedure takes up may be regarded as insignificant with less than 1% of the overall duration.

5.5 Discussion and Conclusions

A novel approach for automating the marking of the resection margin on the tissue surface via ES was presented. The effectiveness of the approach in automating the marking of

tumour boundaries on an organ surface in a controlled lab setting. Furthermore, the work showed, for the first time, the possibility to apply the concept of autonomous tumour boundary marking to an ex-vivo liver specimen.

While the fused kinematics were capable of reducing the error to a range of several millimeters, this still had a noticeable effect on the results of the scanning and marking. The achieved TPR between 0.8 and 0.9 and FDR between 0.05 and 0.15 may be viewed as a success and a potential benchmark for future attempts to automate tumour margin marking. The quantified positional accuracy of around $3mm$ needs to be further improved to ensure reliability, an increase in TPR and decrease in FDR. It should also be noted that the $3mm$ error makes up 20% of the roughly $15mm$ mass size. Employing the system for larger masses will consequently increase the TPR, and decrease the FDR and increase the likelihood of reaching an acceptable reliability level. While there is a maximum tumour size that can be considered for laparoscopic resection, it may still be useful for certain pathologies.

Further improvements should also be made to reduce carbonization and the thickness of the marking. As a first step, a smaller marking tip could be used. This, however, will most likely also influence the contact surface and thus the power transfer. A more generic solution would be to investigate a more fine-grained method to measure impedance and thus the contact quality. Being a feasibility study, an optimisation of the contact control and detection for the electrosurgery tool are out of scope. Improving it would require further insights into the workings of the controller or more precise measurements of the contact impedance. This could include a more thorough characterisation of the power output over different surface impedances, a modification of the ESU, or a further opening of the data interface by the manufacturer.

Future work will be focused on further increasing the accuracy of the system. Currently, this is mainly limited by the robot's positional accuracy as well as the point cloud obtained through the camera. Rather than assuming a static point cloud, a constant update of the dynamic point cloud could be a potential avenue to be explored. Additionally, the system should be transitioned towards a more practical solution for hand-eye calibration, as ArUco markers are not well suited to be employed within the abdomen. One promising direction may be to use instrument surface registration, as previously explored in [183]. With these challenges solved, the system may be assessed in an even more realistic cadaveric or animal studies. For the latter, further approaches would need to be investigated to account for breathing and heart beat motion that have been ignored for the scope of this work.

Another possibility could be to account for uncertainty along the pipeline and integrate this into the calculation and even the outlining of the margined tumour projection [184].

In terms of medical applications, it would be interesting to extend the approach to marking further anatomical boundaries, such as the resection lines along segments. Additionally, more elaborate methods for calculating the projection on the surface are possible, in particular methods that reduce the resection volume in a more discriminate manner. It could also be interesting to investigate performing full resections of tumours or organ segments. Furthermore, the markings could be used for Augmented Reality (AR) projections in future work to give the surgeon a clearer image of where the tumour lies with respect to the outlined projection.

Chapter 6

Autonomous Ultrasound-guided Tumour Ablation

This chapter outlines the results from autonomous ablation using HIFUS. First, the technical requirements of the envisioned system are outlined (see Section 6.1.2) that were the starting point for further investigation. Next, the system concept is developed (see Section 6.1.3 and 6.1.4), results of the probe characterisation and modelling (see Section 6.1.5) as well as the approach for ablation trajectory planning (see Section 6.1.6) are presented. The implemented hybrid force-position control scheme is first tested on a planar phantom following surface trajectories while maintaining a constant contact force (see Section 6.2.3). With control parameters adequately tuned, the system is further scrutinised on a non-planar surface structure (see Section 6.2.3).

As outlined in Section 2.4.3, there are several methods to perform ablation and several works have investigated robotic integration in an extracorporeal context. The only mentioning of robotically assisted laparoscopic ablation was in [156], presenting a design and proof of concept for integration of a miniaturised HIFUS into a flexible robotic arm. It did, however, not include US guidance or any other information for targeted and planned tumour treatment. Furthermore, it did not involve or investigate any autonomy. Looking at the broader context of intracorporeal ablation, HIFUS was identified as a highly suitable technology to be integrated into a robotic setting. The following will give an introduction into HIFUS physics and outline its integration into robotic setup for intracorporeal ablation.

6.1 Materials and Methods

6.1.1 HIFUS Physics

Aside from its application in tissue imaging, US may further be used as a means of delivering and focusing energy. Hereby, the energy that is carried within the ultrasonic waves is used to dissect or ablate tissues. The latter is achieved by focusing the US wave towards a focal point. Thereby, the surrounding tissue is spared while the beam converges at the focal point, rapidly increasing the local temperature to and above $60C$, causing coagulative necrosis and thus cell death of the tissue surrounding that area [185]. Depending on the size and application, this may be achieved either via a single transducer with an attached convex lens or an array of transducers that are placed along a convex surface. The latter gives more control about the focus of the beam, while naturally being more technically complex. Additionally, these systems may integrate an imaging probe placed in the center of the lens that allow imaging the target area in parallel with its ablation. In the context of miniaturised transducers, integrating multiple elements or even an imaging probe are incredibly complex to realise. A schematic depiction of a single transducer system is shown in Figure 6.1. Common frequencies are in the range of $2MHz$ to $4MHz$, while they can go as $10MHz$ or even $20MHz$ for some applications [186].

6.1.2 Requirements for Robotic HIFUS Probe Integration

For the scope of this work, the focus in the following will be on a single element transducer with imaging provided by a separate US imaging probe. Starting from an initial design of the partner institution at the University of Glasgow, a robotic interface had to be integrated into the design, allowing its manipulation by a surgical robotic tool.

Just as in US imaging, ensuring mechanical coupling between the US lens and the tissue surface is paramount to ensure that sufficient energy is induced into the tissue and not reflected back to the transducer. An additional difficulty arises from the fact that the lens is concave as opposed to a usually planar or convex imaging probe design, making a contact with the tissue easier. To achieve good matching with the tissue surface the two main concepts are either submerging the target region along with the transducer inside a coupling medium, such as water, or adding an acoustic impedance matching layer at the end of the transducer as shown in Figure 6.1.

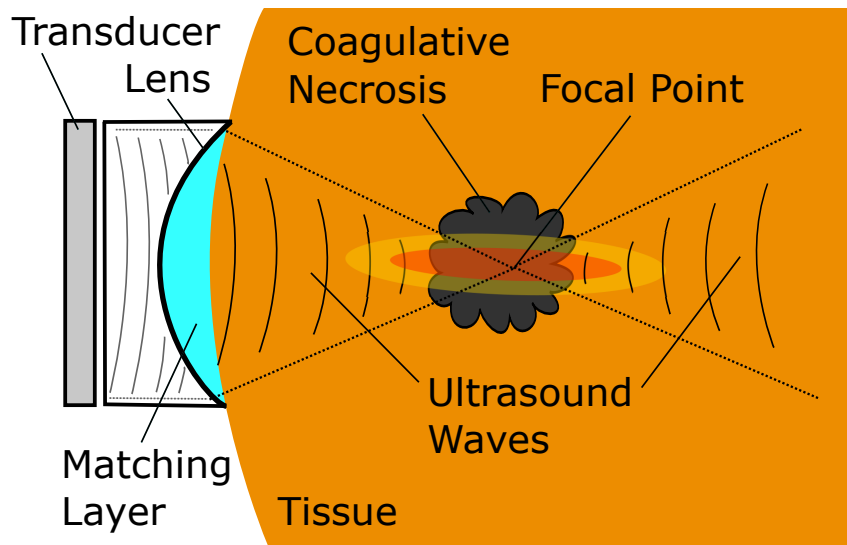


FIGURE 6.1: HIFUS with tumour in focal region. The transducer, usually a piezo element is electrically stimulated to resonate in the ultrasonic spectrum. As the waves travel through and out of the lens they are focused to converge on the focal point. An acoustic matching layer between the lens and the tissue surface ensures that these waves are properly induced into the tissue and not reflected back towards the transducer. Inside the tissue the waves converge onto the focal point. Through constructive interference, the majority of the energy is focused around the focal point causing the local tissue to heat up, denaturizing cell and eventually leading to coagulative necrosis (death of tissue cells). Beyond the focal point the wave front diverges again, spreading the energy over a larger area.

Similarly, to autonomously ablate tissue, a major challenge with any active device is establishing, maintaining and accounting for the contact with the tissue. This means ensuring the device is within a certain contact force range, establishing sufficient acoustic coupling and preventing overly high forces leading to deteriorating kinematic accuracy or even eventually even potential injury. Once again, since force measurement of the robotic system itself was found to be insufficiently accurate and visual estimation seemed unsuitable for the task. Therefore, a different solution to solve this problem had to be found.

Lastly, a method had to be devised that could plan a trajectory of the target region ablation while also taking into account the surface shape and the ideal point of access.

In summary the following three requirements had to be addressed:

1. Allow interfacing the HIFUS probe with a surgical robotic tool (see Subsection 6.1.3)
2. Enable automated interaction with the tissue (see Subsections 6.1.4 - 6.1.5)

3. Provide means for trajectory planning and execution based anatomical information
Subsections 6.1.6 - 6.1.9

6.1.3 Transducer Design and Interfacing

The main transducer was developed and manufactured by our project partner at the University of Glasgow. While miniaturised HIFUS transducers already exist as commercial products, they come at specific specifications in terms of focal length. The novelty in this device comes from the lens design that rather than being continuously convex, employs a Fresnell lens and its design tailored towards the specific application. This means that after analysing the preoperative data, a bespoke HIFUS transducer can be manufactured with the ideal specification for that specific patient's pathology e.g. the ideal focal point for the identified tumour depth. This would allow to treat a variety of pathologies via intracorporeal HIFUS without in being limited by a single transducer design with a fixed focal depth.

The main transducer is composed of a cylindrical shell, a lens and a piezo element that is connected to and driven via two cables (V_{cc} and GND). The shell is designed in two parts, which allows the placement and arrangement of lens and piezo element inside the shell. As common in ultrasonic devices, the entire inside of the shell is filled with epoxy. This serves two purposes. Firstly, it provides acoustic impedance matching between the piezo element and its direct surrounding inside the shell as well as the lens. This is important for the ultrasonic waves to be adequately induced into the lens and not reflected back at the transducer interface. Secondly, it helps to watertight the piezo element and its electronics.

A thread at the top allows equipping the transducer with appropriate mechanical interfaces. For the purpose of interfacing the probe with a robotic tool, a pick-up interface with matching thread was designed to fixate to the transducer. As previously, the pick-up interface was equipped with an IMU as well as an IR tracking marker for evaluation.

6.1.4 Interaction with the Tissue Surface

To solve the issue of acoustic impedance matching, submerging the transducer and target surface was not a feasible option, which left using an acoustic impedance matching layer as the most suitable solution to be investigated. HIFUS systems used in a similar setup

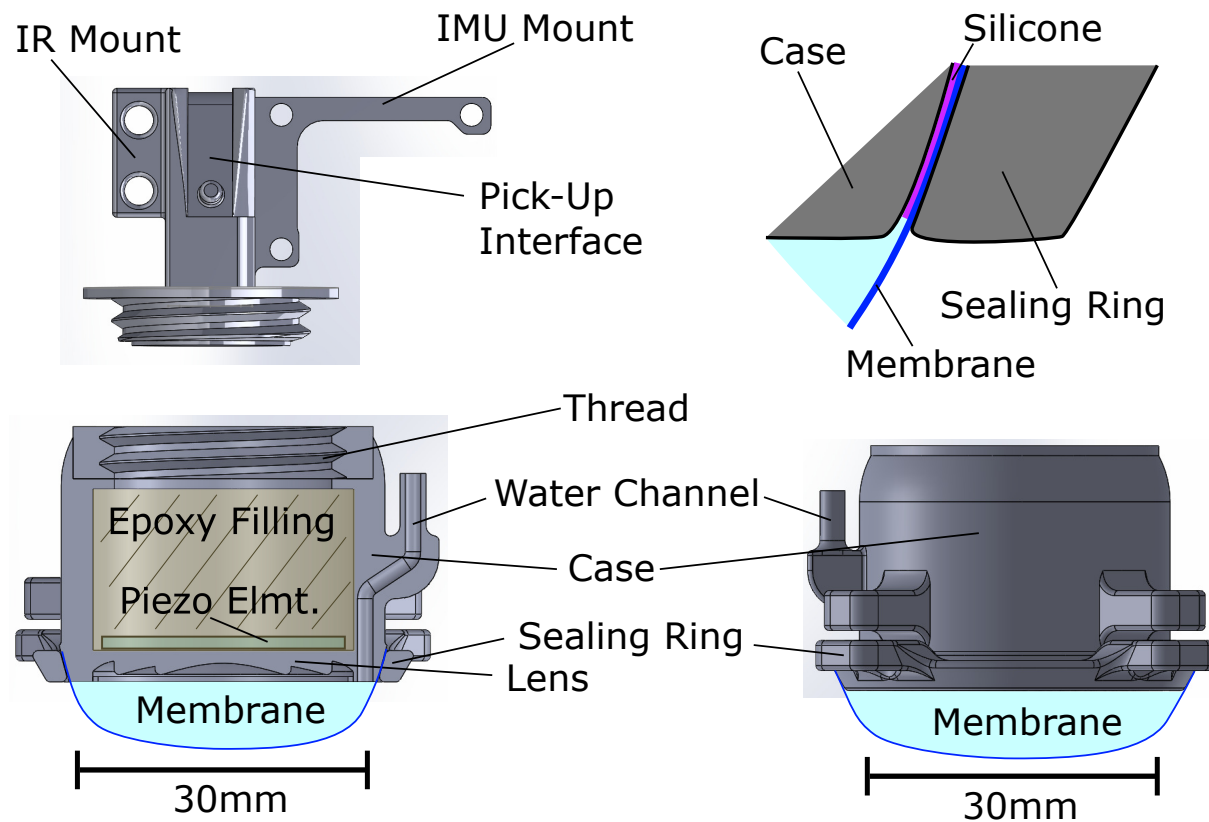


FIGURE 6.2: Cut view of the assembled HIFUS probe design including the epoxy-filled casing with integrated water channels, the sealing ring as well as the piezo element.

described using a water-filled membrane at the end of the transducer [162]. At the same time, being relatively soft, the inflated membrane can conform to different surface shapes.

Considering, the goal of achieving contact control it is necessary to measure the contact force or quality to some degree. An initial idea was to achieve this by attempting to characterise the change in pressure of the inflated membrane under different loading conditions. This would in theory allow the estimation of the contact force between the robotically guided transducer and the tissue surface and ablate the tumour as shown in Figure 6.3.

Starting from the shell design, provided by Glasgow, consisting of the cylindrical, threaded case and the lens, I further modified the design to accommodate the membrane and pressure sensing capabilities. The space at the tip of the transducer was mainly limited by the outlet hole for the piezo element's cables that were not able to bend, which left around 7mm from the tip surface of the transducer. To fit a membrane, it was decided to realise a tapered ring design (See Figure 6.2). The ring is held by four screws that allow equal tightening from all side, while reducing buckling. The membrane is spanned in

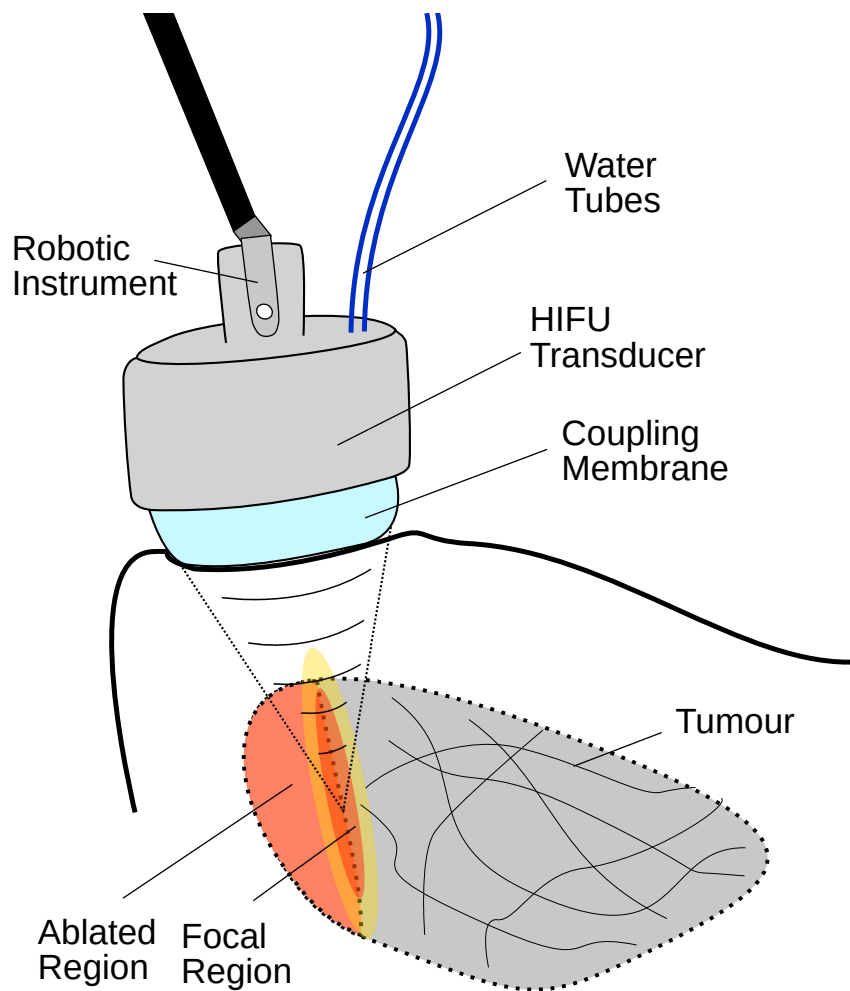


FIGURE 6.3: HIFUS ablation of tumour

between the ring and the transducer. To ensure water sealing the tapered transducer tip is covered with a thin layer of silicone glue that the ring compresses against the membrane and transducer wall.

To allow feeding water into the membrane to instantiate a static pressure and inflation profile as well as measuring the pressure, two 1mm channels were integrated into the casing wall. While, a single channel would also allow for pressure measurements, two channels were needed to expel any excess air trapped between the lens and the membrane. This is particularly important to ensure good energy transfer as any trapped air will lead to a strong reflection of ultrasonic wave back to the transducer. Please refer to Figure 6.2 for a cut 3D CAD model of the transducer shell.

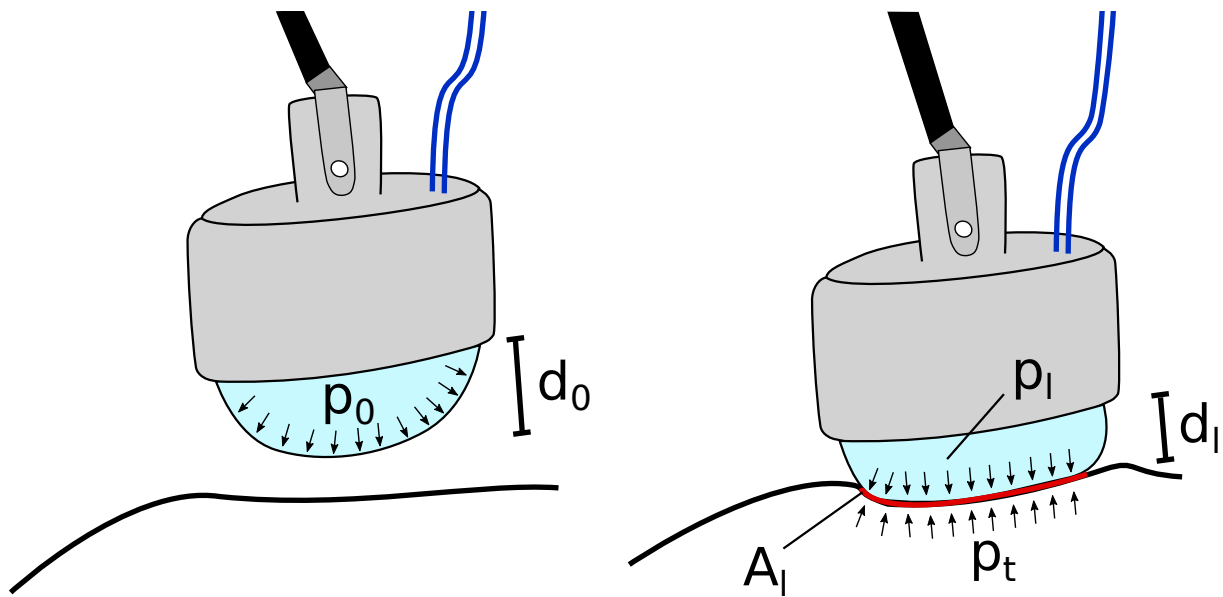


FIGURE 6.4: Concept of the water filled membrane (left) in its inflated yet unloaded state and (right) when in contact with the tissue exerting pressure profile p_t onto the an area A_I of the tissue, resulting in measured pressure change from p_0 to p_I inside the transducer and a reduction in dome height from d_0 to d_I .

6.1.5 Membrane Material Characterisation

To usefully employ the designed membrane in a control context, it became necessary to characterise the material properties of the membrane. An initial analysis revealed that it might be possible to infer the force applied to the tissue surface $f_{HIFUS,ext}$ as well as the indentation of the membrane $\Delta z_{HIFUS,ext}$ in the manner shown in Figure 6.4. Knowing both allows to control the forces applied to the tissue surface, while accounting for the tool length that changes with indentation. A major question was, to what degree these quantities would change depending on differently stiff surface materials the membrane would interact with.

For characterisation, a 3D printed frame was used to fixate the probe within the experimental setup. To apply an indentation and measure the resulting force the setup employs a manually adjustable linear stage (unknown manufacturer) equipped with a load cell Omegadyne LCM703-10 (Omegadyne Inc., Stamford, CT, USA). The load cell is connected to a HX711 (Avia Semiconductor (Xiamen) Ltd, Xiamen, Cina) amplifier. The amplifier's analogue output is then transmitted to the ROS network via a Teensy 3.2 (PJRC.COM LLC, Sherwood, OR, USA) and a serial protocol, in a similar fashion to the previously outlined integrated sensors (see Section 3.4). The tip of the load cell integrates

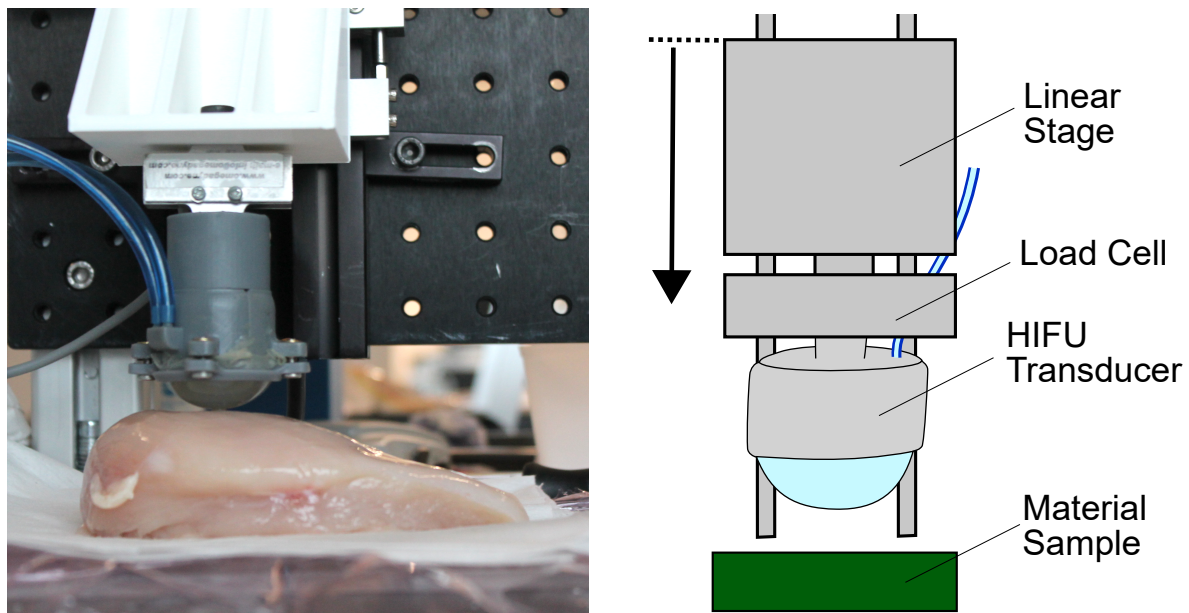


FIGURE 6.5: **Left:** Test Setup used to characterise the HIFUS membrane. The probe is mounted onto a load cell that attaches to a linearly movable stage. **Right:** Schematic drawing of the test rig.

a 3D printed interface that directly connects to the threaded top of the transducer (see Figure 6.5).

The characterisation was performed both for three different material samples of decreasing stiffness that were placed under the probe: a rigid surface, a gelatin block and a chicken thigh. Additionally, experiments were carried out at three different inflation states resulting in varying membrane dome heights. Initially the transducer was placed to barely touch the surface below. This was taken as the starting position in terms of pressure. Then the transducer was moved down in increments between $25\mu\text{m}$ and $50\mu\text{m}$ depending on the material and the rate of change.

For the pressure-force relationship a second order polynomial was found to be the best fitting model of lowest complexity. Figure 6.6 depicts the characterisation results for the pressure / force relationship. The mean RMSE of the fitted curves for the three different initial pressures was $0.0627N$. Overall, the relationship did not significantly vary with a change of indentation material. While the area over which the pressure is applied does change depending on the material, its variation seems to low enough to have little effect on the measured force. As expected, however, it did vary with initial pressure. For the eventual application during robotic control, the weighted average between the two curves with an initial pressure above and below the current initial pressure were taken. This

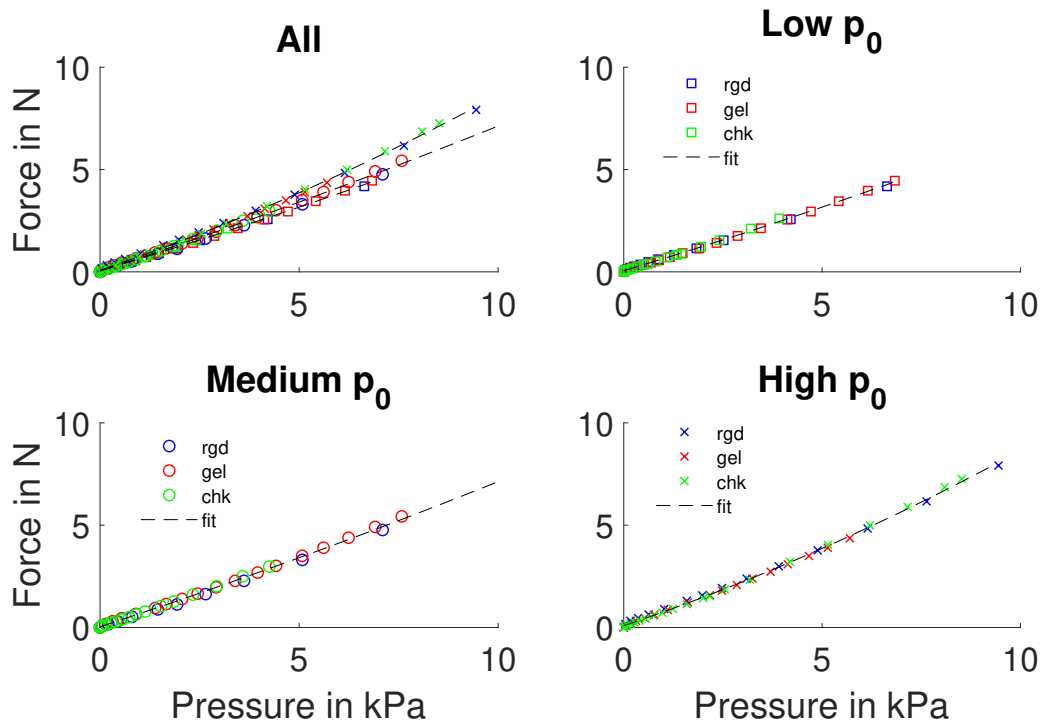


FIGURE 6.6: Membrane Characterisation and subsequent fitting results for membrane pressure (kPa) over force (N) for different materials. Top left shows all data points and fitted curves overlaid, top right, bottom left and bottom right show the data and fitted curves for low, medium and high initial inflation pressure respectively and for different materials.

allowed varying the initial pressure of the system and thereby the compliance as well as the initial dome height of the coupling membrane.

As opposed to the pressure force relationship, the pressure indentation relationship is heavily dependent of the material pairing, arguably more so than on the initial pressure. Trying out third order polynomial, exponential and the sum of two exponentials, the latter was found to be the most accurate fit for this relationship. The overall error for this relationship was $0.0879kPa$ from a given indentation (see Figure 6.7). Unfortunately, this relationship is not easily invertible and while the initial pressure is known through measurement, the material pairing is usually not known. It is for this reason that the route of also estimating the membrane dome indentation was not pursued further.

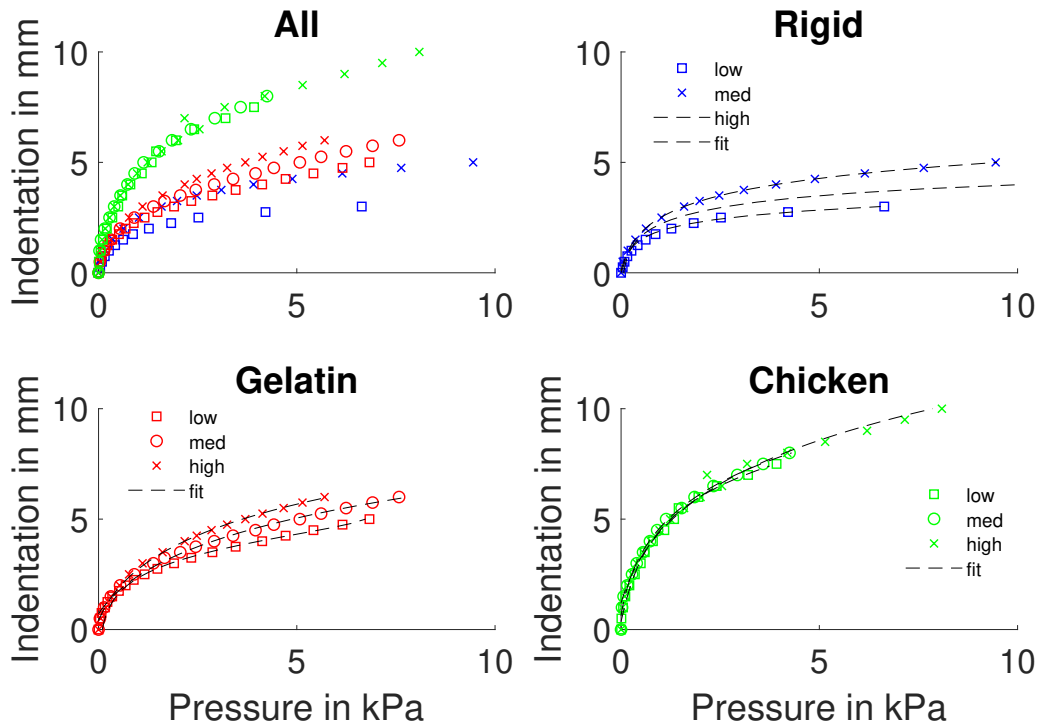


FIGURE 6.7: Membrane Characterisation and subsequent fitting results for indentation over pressure. Top left shows all data points. Top right, bottom left and bottom right show the data and fitted curves for rigid, gelatin and chicken respectively and for different initial pressures.

6.1.6 Trajectory Planning

Planning a trajectory for the laparoscopic HIFUS device is slightly different compared to usual applications in an extracorporeal setting since the target region and probe cannot be immersed in water. Consequently, the planning is highly constrained by the tissue surface, allowing only specific lines of access approximating local surface normals. To allow for a good induction of the ultrasonic waves into the tissue, the probe should be oriented close to the surface normal. Assuming the surface to be relatively planar (e.g. slightly convex) and thus a relatively constant normal vector within the vicinity of each surface point, this may be approximated by finding the surface points whose connecting vector to the tumour's centroid and the surface point matches the normal vector at that point. This point is identified by simply iterating through all surface points and checking the angular error between the connecting vector and the surface normal at that point and selecting the one with the lowest error.

Once the ideal point is found, the DPP method outlined in the previous chapter is employed (see Section 5.2.5) to project the tumour geometry onto the surface normal plane.

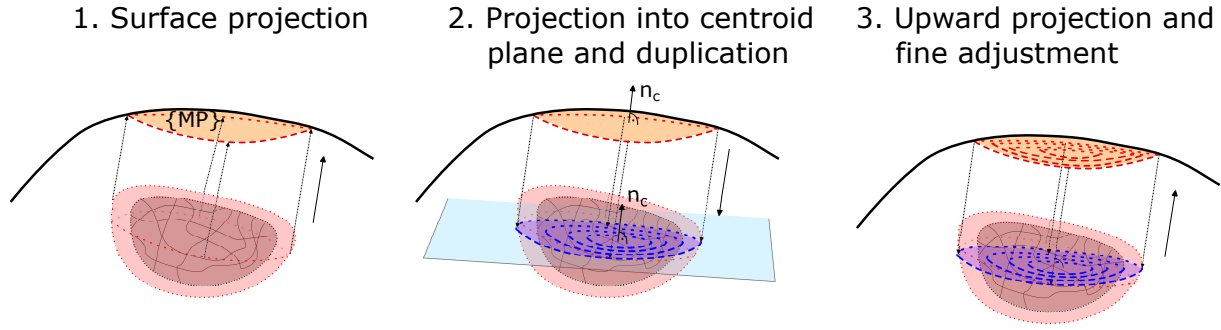


FIGURE 6.8: Trajectory planning process: **1.** Find the best surface point and project the entire point cloud onto the surface using that point's surface normal (\mathbf{n}_C) and calculation of the convex hull **2.** Shift the convex hull into the centroid of the mass, scale and duplicate it to end up with spiraling trajectory. **3.** Project up to the surface and fine-adjust all points to better match the surface normal.

The projected plane is then shifted into the centroid of the tumour. Here the trajectory now outlines the outer most edge of the tumour (see Figure 6.8). To cover the inside as well, the trajectory was repeated multiple times with decreasing scaling, resulting in a spiraling trajectory that covers the entirety of the tumour. Lastly, the points on the surface are slightly adjusted to further minimise their individual surface normal error.

6.1.7 Hybrid Position Force Controller Design

To control the probe position based on the updated IMU-PSM-fused kinematics, while also integrating the force input from the coupling membrane, a hybrid force position controller was devised [187]. The controller is based in global cartesian space in the following way

$$\begin{aligned} \mathbf{x}_{des,i+1} = & \mathbf{x}_{traj,i+1} + \mathbf{K}_{P,x} \Delta \mathbf{x}_{ctrl,i} + \mathbf{K}_{I,x} \sum_{k=0}^{k=i+1} \Delta \mathbf{x}_{ctrl,i} \\ & + k_{P,f} \Delta \mathbf{f}_{ctrl,i} + k_{I,f} \sum_{k=0}^{k=i+1} \Delta \mathbf{f}_{ctrl,i} \end{aligned} \quad (6.1)$$

where $\mathbf{x}_{traj,i+1}$ is the pre-calculated position from the trajectory planner at time step $i+1$, $\mathbf{K}_{P,x}$ and $\mathbf{K}_{I,x}$ are diagonal matrices defining the positional proportional and integral gains and $k_{P,f}$ and $k_{I,f}$ are scalar force proportional and integral gains respectively. The positional difference $\Delta \mathbf{x}_{ctrl,i}$ used inside the controller in turn is defined in the following way



FIGURE 6.9: Hydrophone setup at the University of Glasgow used to measure the pressure field.

$$\Delta \mathbf{x}_{err,i} = \mathbf{x}_{traj,i+1} - \mathbf{x}_{meas,i} \quad (6.2)$$

$$\Delta \mathbf{x}_{ctrl,i} = \Delta \mathbf{x}_{err,i} - (\Delta \mathbf{x}_{err,i}^T \mathbf{z}_{TT,i}) \cdot \mathbf{z}_{TT,i} \quad (6.3)$$

where $\mathbf{x}_{meas,i}$ is the measured position via IMU-fused kinematics at time step i and $\mathbf{z}_{TT,i}$ is the current tool tip z-axis axis. Equation 6.3 subtracts the component that is along the tool axis that is determined by the force difference $\Delta \mathbf{f}_{ctrl,i}$ in the following way.

$$\Delta \mathbf{f}_{ctrl,i} = (f_{des} - f_{meas})^T \mathbf{z}_{TT,i} \quad (6.4)$$

This way it is ensured that the positional control along the tool axis is excluded and fully controlled by the surface normal force. The force vector in turn is defined in the following way

6.1.8 Pressure Profile Characterisation and Modelling

Applying HIFUS to tissue ablation, requires precise knowledge about the spatial distribution of induced energy. More specifically, it requires knowing the shape and magnitude of the induced pressure field. To acquire this data it is common practice to immerse and spatially fix the HIFUS probe inside a water tank and measuring the pressure field via

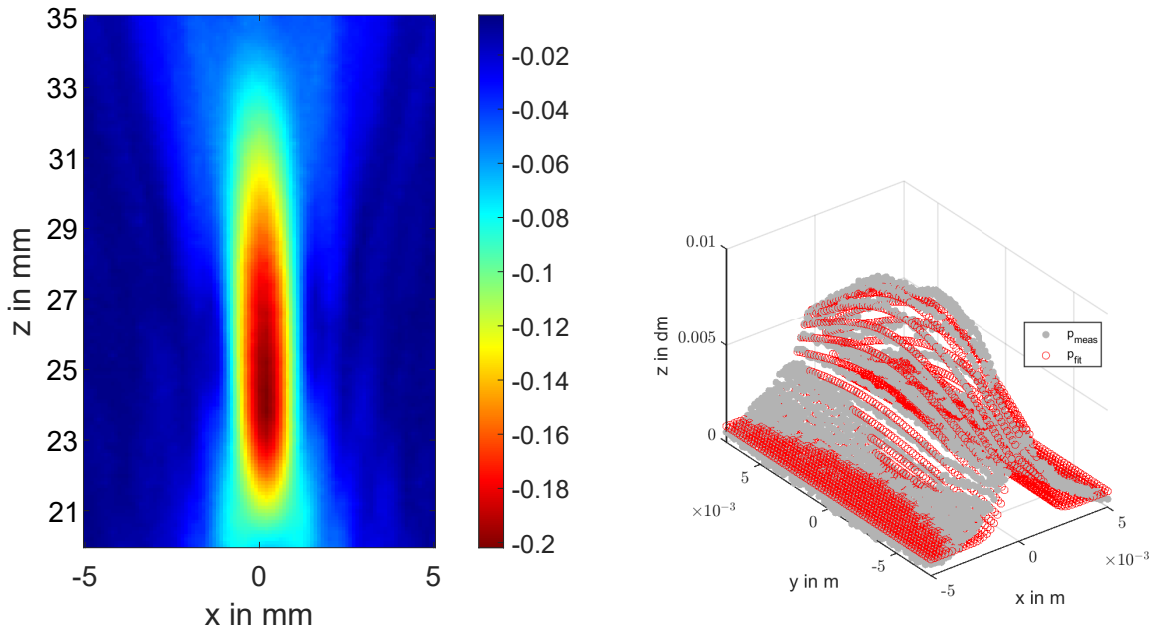


FIGURE 6.10: **Left:** Hydrophone pressure field measurements of the HIFUS probe as measured by the research partners at University of Glasgow. The focal point of the HIFUS pressure field can be clearly observed at a distance of 25mm from the transducer. **Right:** 3D representation of the same measured pressure field, overlaid with the fitted curve

a miniature hydrophone. By mounting the hydrophone on a serial chain of three linear stages, the hydrophone can be spatially displaced in all three spatial directions and the pressure field can be measured. The setup is depicted in Figure 6.9. Since the pressure field of the transducer is rotationally symmetric around the lens surface normal, the measurements can be performed in any plane which includes focal point and transducer normal. Note that the acquired data depicted in Figure fig:hifu-hydrophone - Right was provided by the Ultrasurge research partners at the University of Glasgow.

Figure 6.10 shows the results of the measurement. The focal point of the HIFUS pressure field can be clearly observed at a distance of 25mm from the transducer. The mean focal region (-3dB isoline) marks an elliptic region around the focal point. This is equivalent to approximately a 50% reduction in the negative pressure amplitude, a measure commonly used in the HIFUS research community as it hints towards the presence of cavitation effects. The -20dB line in turn represents roughly a 99% reduction in the signal. To integrate knowledge about the induced energy into the robotic control framework, the 3D pressure field is modelled as a 3D-gaussian with $\sigma_x = \sigma_y = 0.00113$ and $\sigma_z = 0.00969$. For the final field, the intensity is normalised to end up being between 0 (minimum pressure) and 1 (maximum pressure). Figure 6.10 shows the overlay of the fitted and the measured

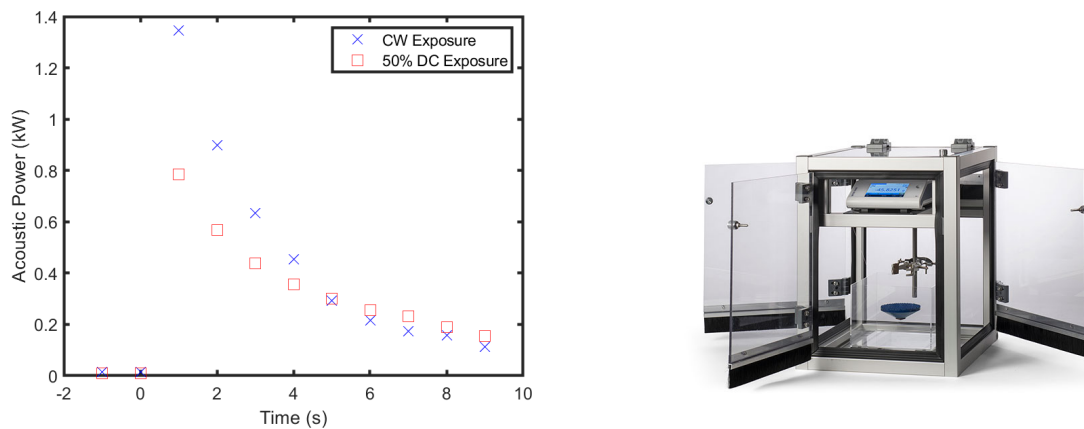


FIGURE 6.11: **Left:** Power drop of the transducer measured over time both for continuous wave (CW) and 50% duty cycle (DC) exposure as acquired by the Ultrasound Group at the University of Leeds via radiation force balance. **Right:** Precision Acoustics Radiation Force Balance used for validation (© 2023 Precision Acoustics Ltd.)

profile. The root mean squared error over the entire field is 0.0523, meaning roughly a 5% error.

Hydrophones usually only allow measuring pressure amplitudes at low power driving signals, as higher driving signal may cause cavitation that could burst its sensitive membrane. To extrapolate the pressure field to higher pressures, a radiation force balance (Precision Acoustics Ltd., Dorset, UK) can be used that registers the integrated power and validate the power output at higher driving powers (see Figure 6.11). Unfortunately these measurements, performed by the Ultrasound Group at the University of Leeds revealed issues with the transducer at higher driving power. While for a short time of around 0.5s, a sufficiently high power could be measured, the energy quickly dropped to extremely low levels. This can further be seen in Figure 6.11. A plausible reason may be the heating up of the transducer, in combination with the choice of piezo material. Additionally, acoustic nonlinear effects as reported in [188] may cause the creation of higher harmonics with vastly increased attenuation and a consequent reduction of the overall pressure at the focus. This all meant a redesign of the transducer would have become necessary. Unfortunately, this would have required redesigning the entire casing with cooling channels and, ideally, manufacture it from a different material with a better heat transfer coefficient (e.g. a stainless steel). While this meant that no ablation was possible with this transducer, the capabilities of robotically targeting specific tumour regions and assessing the suitability of the membrane in establishing and maintaining contact may still be adequately evaluated and directly translated.

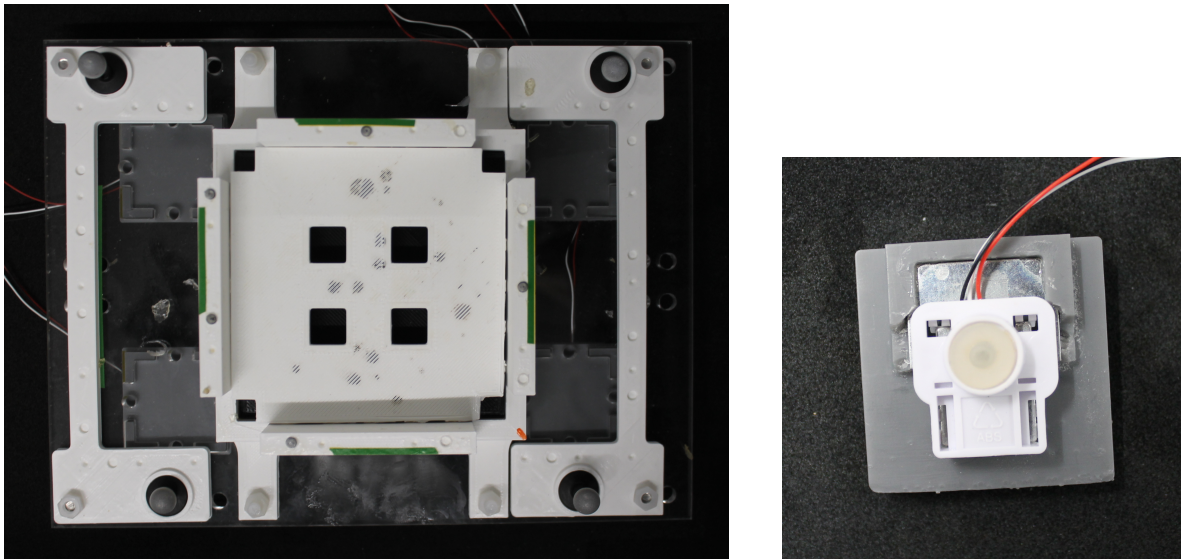


FIGURE 6.12: **Left:** Frame for phantom fixation, IR tracking and load cell measurements. **Right:** Close up view of a single load cell element

In the following results were all performed with a final prototype, however, without the HIFUS transducer being actually driven. In the following, it is therefore assumed that the transducer will in the future be capable of ablating tissue and approximately in the manner previously modelled.¹

For the experiments a framework for monitoring the energy induced into the tumour and surrounding tissue was implemented. The pressure field is treated as a discretised $4D$ point cloud (three positional and one amplitude value) that are logged over time. The pressure field around the transducer is modelled. For the sake of simplicity here, the time dimension is being ignored, since only an applied amplitude over time would result in an increase in temperature. To integrate this point a model that could simulate the temperature field over time would be needed. In ignoring this point, it is assumed that a specified temperature could be achieved by simply moving the probe slower or keeping it stationary in specified locations around the tumour to increase the delivered energy. Here, the goal is rather to see how well the system and approach can target and cover specific regions under autonomous robotic guidance.

¹The HIFUS transducer was provided to us as part of the EPSRC project Ultrasurge and manufactured and developed by the university of Glasgow. Due to these constraints it was out of our control to provide a working transducer.

6.1.9 Beam Steering

While the transducer is custom made to fit a certain tumour profile and thus focal point, there is an additional possibility to change the focal point of the transducer by inducing waves of a differing frequency. Due to the nature of the Fresnell lens a higher frequency will shift the focal point closer to the transducer whereas a lower frequency will move it further away from it. Our project partner in Glasgow was able to confirm this in hydrophone experiments. Realistically the focal point can be adjusted within a range of $9mm$ around the focal point of $25mm$ it has been designed for. This makes it possible to cover a wider range of tumour sizes and depths. Since this is still work in progress, the assumed fixed depth for now will be $25mm$ as previously modelled.

6.2 Experiments

After the concept design an experimental study was performed to validate the system in more depth. In a first experiment, the force estimation and trajectory following on a planar surface was further scrutinised. With the system properly tuned, further experiments were performed on a custom gelatin phantom and an anatomical surface, similar to the one used in the previous chapter. This was meant to test the controller under more complex conditions as well as validate the trajectory planning algorithm.

6.2.1 Experimental Setup

To validate the forces, a frame that sat on top of four load cells and hosted a gelatin phantom was devised. The frame consisted of a laser cut plate integrating the four load cells at the bottom. At the center of the plate, a 3D printed frame was fixated that held the gelatin phantom in place (see Figure 6.12). Furthermore, the frame integrated spatial landmarks and IR tracking markers that were used to co-register the robotic arms and acquire positional reference data respectively. With the probe orientation controlled to be normal to the platform, its load cells and the planar surface, meant that the four load cells were picking up any force transmitted by the probe.

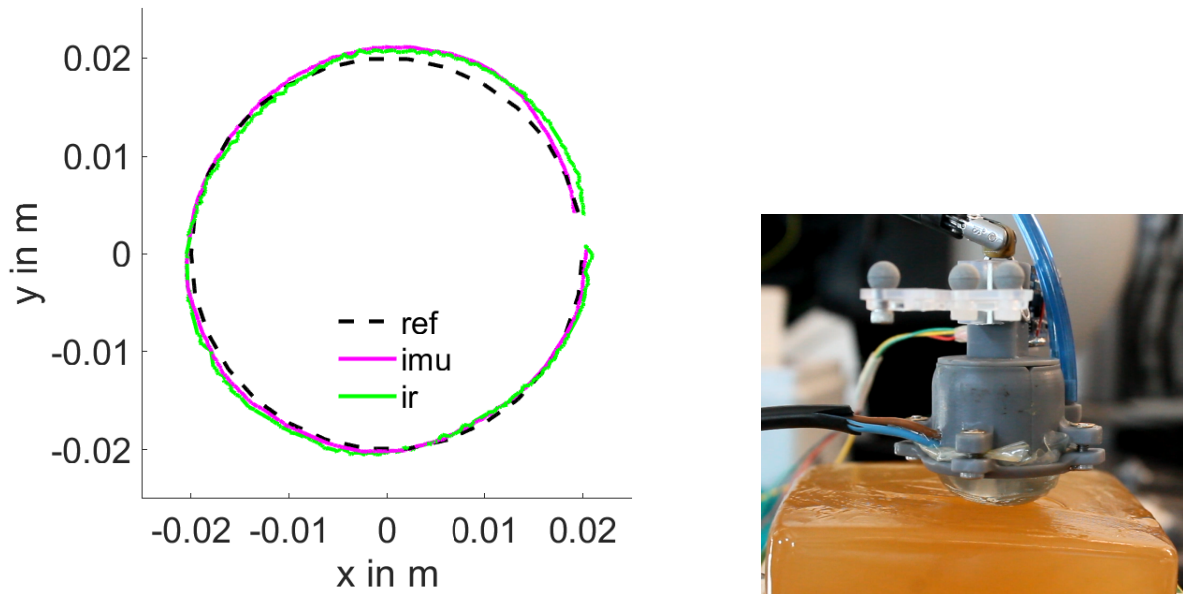


FIGURE 6.13: **Left:** Planar trajectory executed on a block of agar **Right:** Experimental setup including robotically guided HIFUS probe and planar agar phantom.

6.2.2 Planar Surface Testing

Three repetitions of three different trajectories, all circular trajectories with varying diameter ($d = \{10, 20, 30\}mm$), were performed and recorded, giving a total of nine trajectories. In addition to following the trajectory, a target contact force constrain of $1N$ was set.

The results indicate positional errors of $0.6312 \pm 0.3133mm$ between IMU-fused and IR trajectory. The control error, meaning the error between the reference trajectory and IMU-fused kinematics as input into the controller was determined to be 0.8039 ± 0.3219 . Lastly, the error between the IR-tracked, ground truth path and the control input was 1.0212 ± 0.5021 . Figure 6.14 shows the three measures as box plots. Qualitatively, Figure 6.13 shows a good overlap between the executed trajectories, as both measured by IMU-fused kinematics as well IR-tracked and the reference trajectory.

Looking at the force control, a slight overshoot at the beginning can be observed that is slowly controlled out over the course of the trajectory. Furthermore, a lower peak force is observable, as well as slight time delay between the measurement with the HIFUS membrane and model and ground truth force measured through the scale. Despite this, the overall estimation of the model, particularly for static pressure, is as low as $-0.0364 \pm 0.0861N$. Disregarding the first $5s$ in which the controller has not yet reached its steady

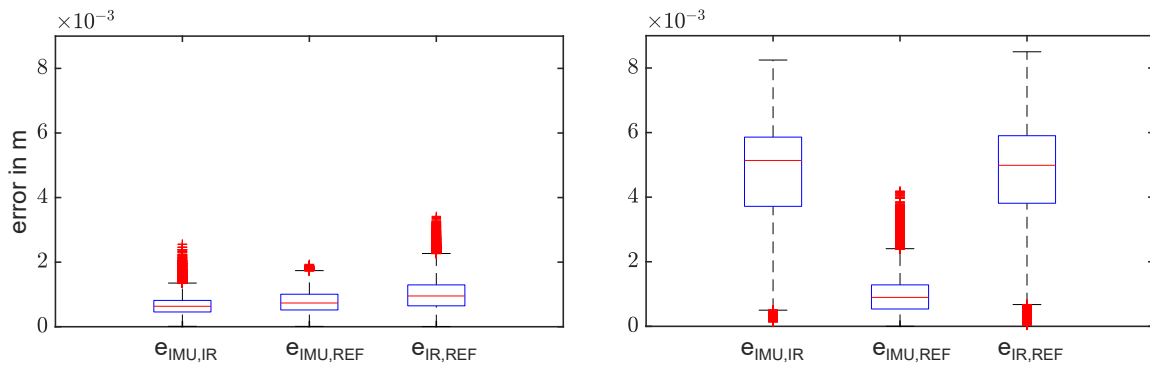


FIGURE 6.14: **Left:** HIFUS position errors for planar trajectory execution comparing the errors between IMU-fused, IR-tracked and reference trajectory with one another. **Right:** HIFUS position errors for phantom trajectory execution comparing the errors between IMU-fused, IR-tracked and reference trajectory with one another.

state, the error is as low as $-0.0135 \pm 0.0448N$. An attempt to increase the P -gain of the controller, leading to a quicker response, led to oscillatory motion of controller, signaling instability. Eventually, while not ideal, it was decided to leave the controller tuned as shown in Figure 6.16.

6.2.3 Non-Planar Phantom with Ultrasound Guidance

For the non-planar case the experiments also included three repetitions at three different locations. The phantom included a single mass that was scanned using the same routines outlined in the previous chapter (see Section 5.2.4). To validate the system under different tumour locations, the acquired scan was virtually shifted to two other locations, covering different surface topologies while remaining at a similar depth. Subsequently, the reconstructed scans were processed in the trajectory planner. As a starting point a spiraling trajectory with four concentric circular turns was chosen. An exemplary resulting trajectory is shown in Figure 6.15. Execution time of these trajectories was around 260s. As in the prior planar experiments, the desired pressure was set to be 1N.

Looking at Figure 6.14, the significantly higher positional error compared to the planar case becomes apparent. While the control error stays roughly similar ($0.96 \pm 0.53mm$) aside from more outlier, the mean error between IMU-fused and IR trajectory was determined at $4.77 \pm 0.91mm$ and at $4.77 \pm 1.03mm$ between IR and control input trajectory. Looking at the force control signal, a good tracking of the constant desired force of 1N can be observed (see Figure 6.17). The mean control error was found to be $0.0088 \pm 0.0689N$.

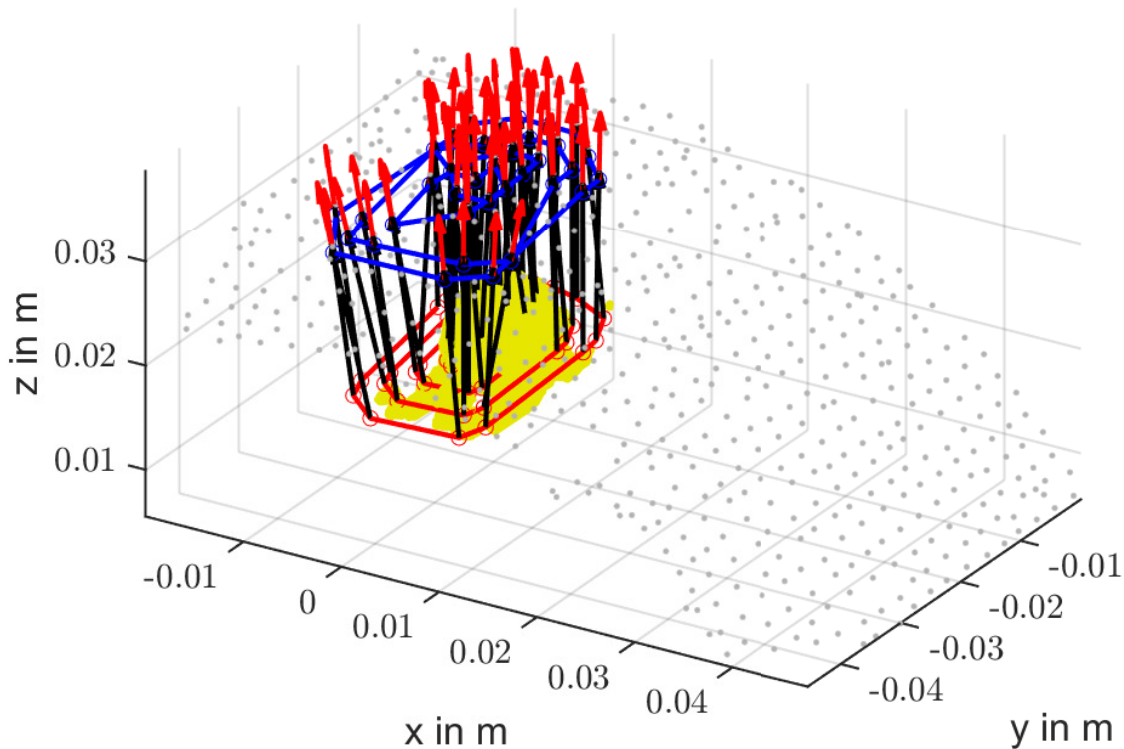


FIGURE 6.15: HIFUS trajectory generated including normal orientation and the connecting vectors between surface and tumour target point.

To get a better idea of the coverage of 3D space by the HIFUS pressure field, the HIFUS pressure field was recorded as a 4D point cloud over time, containing 3D position and pressure intensity. It is assumed that only a pressure over a certain threshold would have a noticeable heating effect on the tissue. Therefore, any points with a pressure intensity lower than 50% of the maximum, equivalent to points outside the $-3dB$ line from the gaussian model, are disregarded. Figure 6.18 depicts this thresholded pressure point cloud overlaid with the tumour volume. The overlay shows a full coverage of the tumour area with the focal region. As it can also be seen though on the top view, the trajectories are not nearly dense enough yet, as there are spots that are not fully covered by the HIFUS pressure field point cloud.

Looking at the plot of the trajectories depicted in Figure 6.19, an offset between the IR-tracked and reference trajectory become further apparent. While the IMU-fused trajectory is following the overall shape, the IR-tracked trajectory is clearly offset, despite still resembling a similar overall shape.

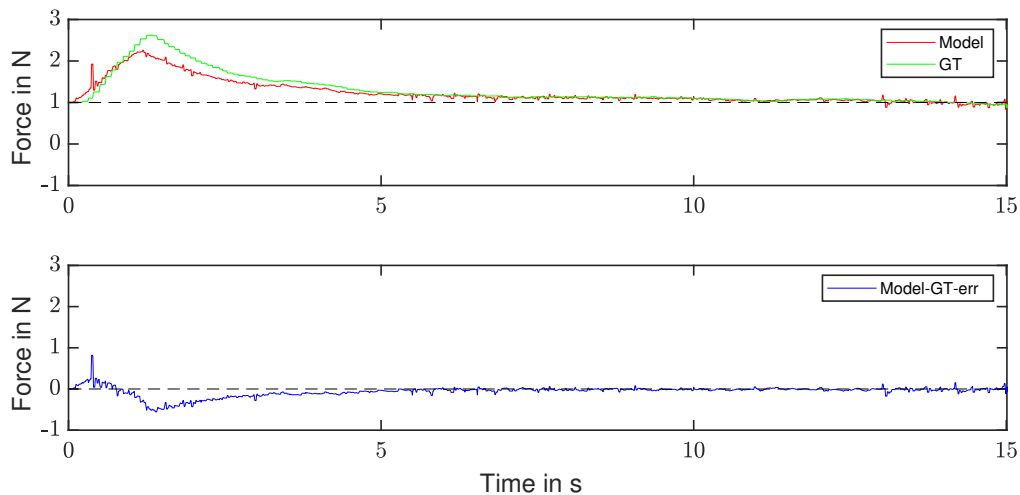


FIGURE 6.16: HIFUS force during execution of planar, circular trajectory.

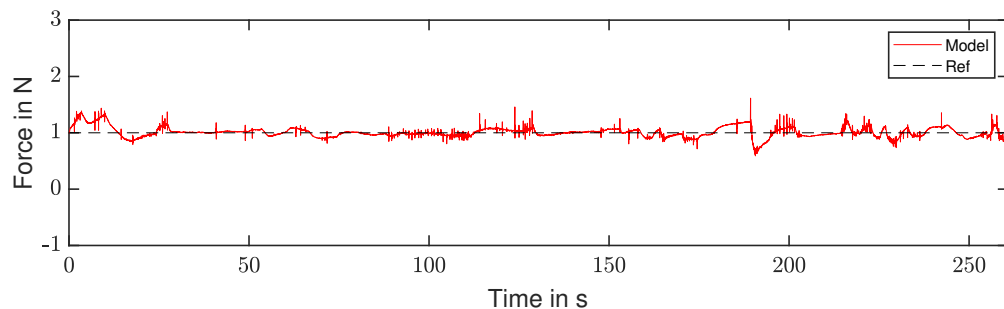


FIGURE 6.17: HIFUS forces during execution on non-planar phantom targeting concealed mass.

6.3 Discussion and Conclusions

Comparing the results for the simpler experiment on a planar surface with the more complex scenario of the anatomical surface and target structure, potential sources of the larger error can be identified.

Firstly, as in the previous work presented in this thesis, the applied force has a tremendous effect on the kinematic accuracy of the system. As opposed to the previous applications, US scanning and tissue marking, contact forces between the tool tip and the tissue surface are not supposed to be minimised, but rather enforced to be constant yet very much present. This had a clear effect on the systems accuracy in determining the position despite IMU-fused kinematics. This error is likely very dependent on the exact orientation of the system, since different joints are differently accurate and the fusion algorithm does

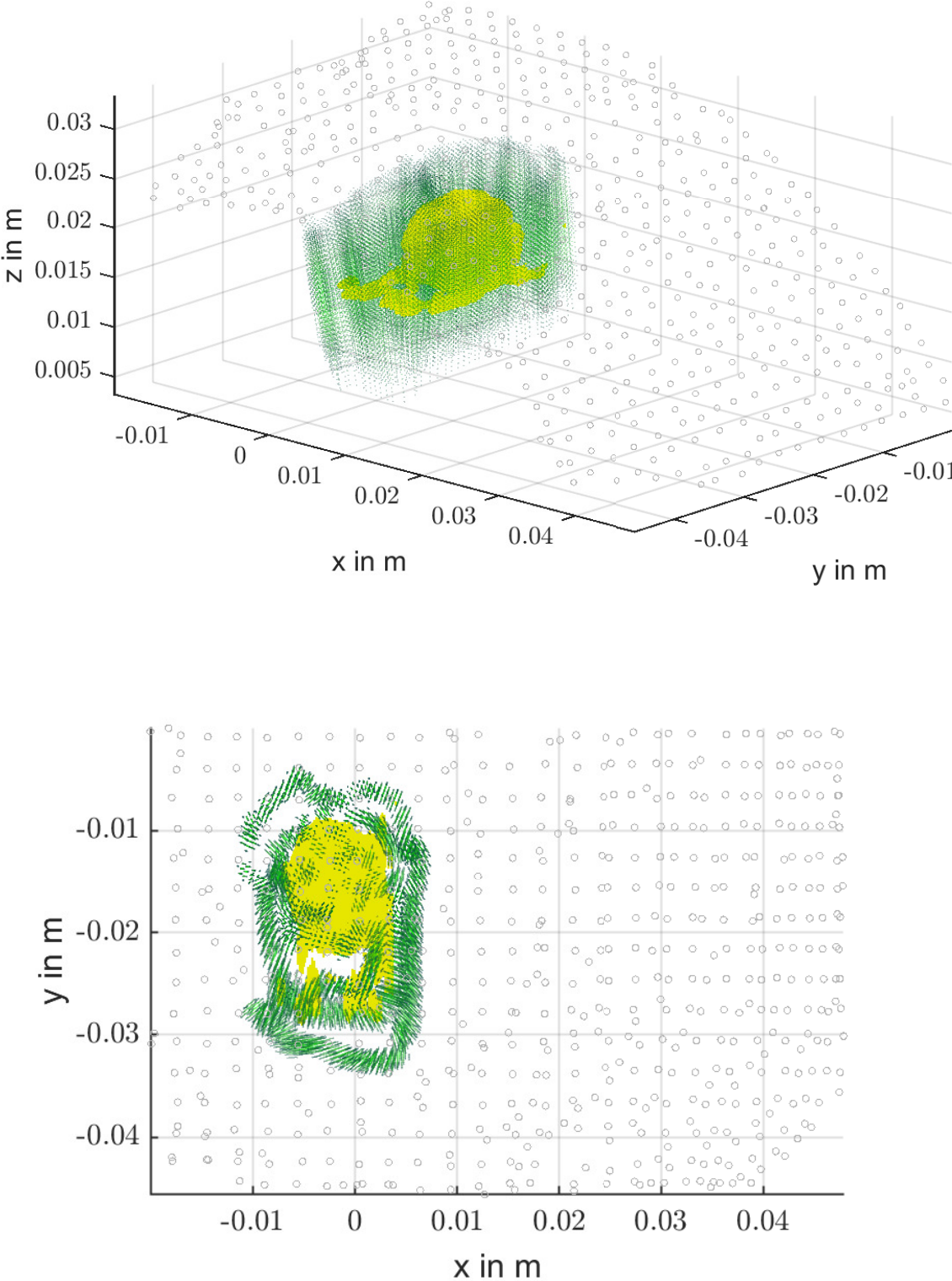


FIGURE 6.18: **Left:** HIFUS tumour coverage in 3D. **Right:** HIFUS tumour coverage projection in x-y plane, showing full but coarse coverage of the area.

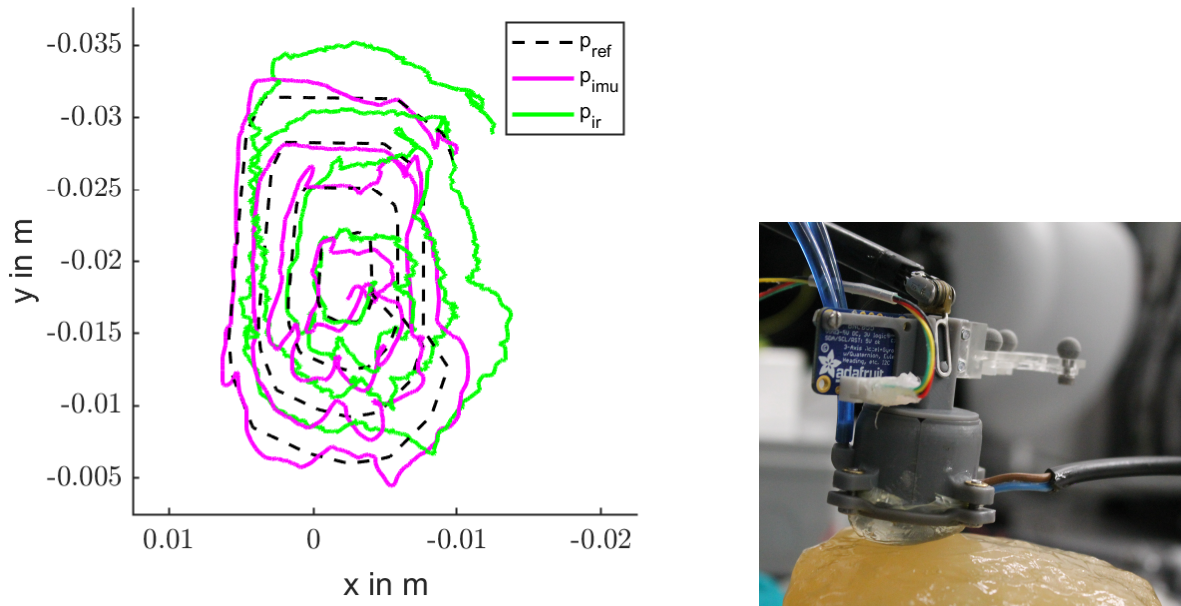


FIGURE 6.19: **Left:** HIFUS trajectory as with reference, IMU-fused and IR trajectories. **Right:** Experimental setup with membrane conforming to surface shape

not account for rotations around the gravity axis that are not measured by kinematics itself.

Secondly, the control of the system is performed via a virtually prolonged tool by controlling the positing of the focal point around $25mm$ away from the transducer surface. This mean, in consequence, that any orientational error will be further magnified by the longer tool tip resulting in higher positional errors. This becomes especially apparent when comparing the results for the planar execution that had no prolonged tool and did not involve a constantly changing tool orientation.

It remains to be seen how the whole system would perform under induction of real ultrasonic energy into the tissue. Most likely, the robotic execution would need a denser coverage of the surface area, which would in turn mean a longer execution time. As the execution is currently already at over $4min$, this in turn would entail practical considerations as to how long would be acceptable or to what extend the execution time may be sped up.

When analysing the trajectories, it becomes clear that the grid structure of the surface has a strong effect on how the trajectory is projected upwards. As currently, the surface point cloud is rather coarse at $3mm$ grid size, the resulting trajectories are also relatively edgey. Therefore, a finer grid of the surface would be desirable. For that a more textured

US phantom would need to be created or the system directly evaluated in an ex-vivo setting as done in the previous chapter.

While only accurate within roughly $5mm$, the system still performed well in covering the area around the tumour. In particular, it covered the entire areas as previously planned. In the future it would be desirable to integrate the model of the indentation height that was obtained through the characterisation. This may be useful in the determining at what depth below the tissue surface the transducer is currently focusing. In theory, this model may be coupled with the kinematic information from the robot and could help improve the tactile information gained e.g. identifying the stiffness of the tissue at that point and thus improving the indentation measurements.

Chapter 7

Conclusions and Future Direction

This work explored means to provide autonomous assistance during robotically assisted minimally invasive surgery employing intracorporeal US as a main source of guidance. While many groups have extensively researched extracorporeal US, there remains a distinct lack of research into intracorporeal applications. Furthermore, the majority of these works employ visually tracking markers on the instrument that are not a practical solution for real surgical applications, including spatial constraints, reduced visibility and coverage by bleedings or other body fluids.

For the purpose of enabling US-guided autonomy, a robotic platform was built up including tool integration and IR tracking in Chapter 3. Based on an initial assessment of the platform concluding strong tool backlash, Chapter 4 introduced and assessed a novel IMU-sensor fusion scheme that allowed to account for orientational changes of the robotic tool tip, induced by external forces. Further contributions were made in the development of a platform and algorithmic approach to apply the sensor fusion scheme to the autonomous scanning and 3D reconstruction of a vascular structure on an ultrasonic phantom. The results confirmed a significant improvement of the kinematics accuracy, particularly preventing backlash-induced skips in the trajectory. The resulting accuracy was in the range of several millimeters.

With the involvement of a second robotic arm, the focus of the work shifted towards applying the autonomous navigation to tumour surgery and employing the 3D reconstructed geometry to perform meaningful assistance to the surgeon (Chapter 5) with the goal of eventually performing autonomous procedures (Chapter 6). In particular, mentally mapping the US image via the endoscopic image onto the actuated cutting instrument was

identified as a promising research area for autonomous assistance. To address this, a solution that mapped the margined tumour geometries onto the surface and autonomously marked them using ES tools was developed and assessed. The achieved true positive rates of 85% and offsets as high as 5mm were found to be an acceptable, initial start for further improvements.

Moving towards higher autonomy, autonomous tumour ablation was identified as another promising avenue. The concept made use of a HIFUS probe that was developed as part of a research project STORM lab has been a part of. To enable autonomy, a sensorised water filled membrane was integrated that served both as an impedance matching layer between the HIFUS transducer and the tissue surface as well as means to measure contact forces with the tissue surface. To this end, a material characterisation was carried out to model the relationship between measured pressure change and forces applied to the tissue. Furthermore, a hybrid force-position control scheme and trajectory planning algorithm was setup to enable planning and controlling the robotic position based on a given internal ablation trajectory and surface force profile. The final evaluation revealed good force tracking and tumour coverage despite positional inaccuracies.

Overall, this PhD thesis was able to achieve several milestones and contributed toward the following:

Platform and Approach for Ultrasound-Guided Autonomy

With the platform concept outlined in this work, an important step was made towards translating the plethora of work from extracorporeal US scanning to the realm of surgical robotics and intracorporeal US guidance. This included the design and integration of additional hardware, in particular robotic pick-up devices, sensor integration, in particular IMUs, as well as the development of a deep learning based vision pipeline capable of segmenting US images and extracting further clues about the acoustic coupling with the tissue surface. A foundation of this was the build up of a comprehensive data set of labeled US image samples. Being sampled from commercially available US vessel phantoms, it may be of particular interest for further research groups working on US-enabled autonomy and is planned to be release as a publicly available labeled image dataset in the future.

Furthermore, the integration of ES tools allowed the exploration of autonomous functionalities. Future efforts should explore further translation and synergies between extracorporeal and intracorporeal US scanning. An interesting aspect of research could involve the

application of reinforcement learning as done in [189]. The current trend towards elaborate simulation environments in the surgical robotics community could further enable this research route [190].

Analysis and Solution Approach for Kinematic Inaccuracies

A further major contribution of this work was the development and assessment of a sensor-based approach for improved kinematic accuracy. This showed to be particularly beneficial in the reconstruction and navigation of anatomical structures and in the more accurate control of surgical instruments.

Primarily, the inaccurate kinematics of the robot are still a main hurdle in more accurate and reliable application of autonomy. To this end, more researchers should be encouraged to validate their algorithms against a tracking technology more suitable to be treated as a ground truth (e.g. IR-tracking) as it has been done in this work. While the devised IMU sensor fusion scheme is able to strongly decrease kinematic inaccuracies, it could further be improved by integrating measurements of the rotation around the gravity vector. This may be achieved via the integrated magnetometer that was purposefully excluded. To see if this technology is fitting, a more thorough analysis would need to be carried out to ensure its orderly working within a surgical environment. Similarly, arm co-registration on the current platform is another main obstacle that needs to be overcome for further improvements in accuracy and robustness to unfold. The currently used approach of spatial landmark registration is hard to accomplish inside the abdominal cavity. While in theory a marker, introduceable through a trocar, could be devised, it would be much more desirable to rely on kinematic measurements to provide the flexibility of rearranging the SUJ configuration during surgery without the need of co-registration. Fortunately, more modern surgical robotic systems such as the da Vinci Xi, seem to include this functionality to an acceptable accuracy.

Planning, Navigation and Control in an Intracorporeal Setting

This work has illustrated several routes in which US enabled autonomy could be realised in the context of surgical robotics. At the core this included the development of planning algorithms, such for tumour boundary marking and HIFUS ablation, novel navigation schemes, such as for autonomous exploration of vessels, as well as the integration of

interaction control schemes. This particularly applies to the hybrid force position control scheme developed for the HIFUS ablation.

A crucial bottleneck in this is the availability of further sensory signals. Further avenues should be explored to allow for a finer interaction control of the ES with the tissue surface. This would prevent the charring and deeper incisions observed during ex-vivo experiments. A key step towards a more holistic planning pipeline could also be the integration of pre-operative imaging. To this end the autonomous exploration of anatomical structures could both be pre-informed and eventually combined to improve the planning quality for tissue resection or ablation.

Ex-Vivo Feasibility Study

A major milestone of this work was the successful feasibility study of ex-vivo tumour boundary marking. This marked the demonstration of a level 2 autonomous US-guided functionality, including the scanning and reconstruction of the tumour geometry as well as marking the calculated and projected tumour margin onto the tissue surface using standard ES tools.

Further experiments are needed to fully confirm the results. While this work has largely focused on solutions involving no visual tracking and visual perception of the surgical environment, further work could work towards combining the work done with visual approaches, such as identifying key points in the surgical scene. A crucial element for this will be a more practical solution for hand-eye calibration that does not rely on ArUco markers but rather on the technology available in a surgical setting such as the pure endoscopic stereo image. Current efforts, such as the MICCAI 2022 EndoVis challenge underline the importance of the topic for the research community as a whole [191].

Ultrasound-Guided Intracorporeal Robotic HIFUS

With the exploration of autonomous intracorporeal HIFUS ablation, this work has realised a surgical assistance function of level 3 autonomy. A key part of this endeavor was the development and assessment of a sensorised coupling membrane.

Future prototypes should also include the transition towards an ultrasonic-based cutting tool and a working version of the HIFUS transducer that were unfortunately not at a working state for the time scope of this PhD. Particularly in the case of HIFUS, this

would give further clues to the more precise conceptualisation of planning algorithms and fine tuning them more towards clinical needs. Similarly, investigating a more tailored, miniaturised imaging and cutting devices that include further sensing modalities such as contact (e.g. via impedance) or contact force sensors (e.g. via FSR), could be an effective way to improve accuracy. Knowing the contact forces more precisely could also be used to inform the kinematics and account for the increased inaccuracies found at larger contact forces.

Despite the encouraging results, the approaches presented in this work still contain specific limitations, aside from the already mentioned spatial inaccuracies still present in the system. Concerning the US scanning, the probe still requires to be placed in the direct vicinity of the vessel or tumor to be scanned. A base for further exploration could be the inclusion of bayesian methods to probe the entire organ surface and probabilistically identify regions of interest such as in [192]. The ES-based marking in turn lead to significant charcoaling that needs further investigation and improvement, in particular fine-tuning the contact detection based on the ratio between expected and delivered power. Lastly, for the HIFUS-based tissue ablation the biggest limitation was the fact experiments were only carried out on a non-functional device that could not deliver sufficient US energy for ablation. In case a redesign of the probe becomes infeasible or still does not lead to satisfactory ablation results, commercial systems could be considered to carry out further experiments and allow more solid conclusions.

Once the technology is more mature a comparison with surgeon and their integration in a more harmonised user interface (UI) and user experience (UX) will become necessary and are likely to drive the further development efforts around autonomous US-guided assistance and surgery. Being an early stage work, further investigation will be needed before transitioning to a more complex environment. This could include considering heart beat and breathing motions that have been ignored within this work, that, however, are clearly present in a real world surgical environment. First works that have treated this endeavor such as [108] could be a good starting point.

Appendix A

Appendix

A.1 General Remarks

Please note that all experimental values expressed as $x \pm y$ represent mean x and single standard deviation y comparable to other publications in the field.

A.2 Nomenclature

Within this work a specific mathematical notation is used to denote the several coordinate frames and transformations between those frames defined in our system. Transformations with a mere subscript such as \mathbf{T}_A (including \mathbf{R}_A and \mathbf{p}_A) are used to refer to the coordinate frame itself, while the transformation from a coordinate frame \mathbf{T}_B to coordinate frame \mathbf{T}_A is written as \mathbf{T}_A^B and denoted with subscript and superscript. Additionally, comma-separated superscripts such as $\mathbf{T}_A^{B,des}$ are used to specify the relative poses, in this case the desired (abbreviated as *des*) relative pose of B with respect to A . Expressed in other terms, \mathbf{T}_A^B is the pose of \mathbf{T}_B relative to \mathbf{T}_A . Broken down further, \mathbf{T}_A^B is defined as a homogeneous transformation, composed of a rotation \mathbf{R}_A^B and a translation \mathbf{p}_A^B

$$T_A^B = \begin{bmatrix} \mathbf{R}_A^B & \mathbf{p}_A^B \\ 0 & 0 & 0 & 1 \end{bmatrix} \quad (\text{A.1})$$

For vectors, uppercase letters are used for the superscript to denote defined coordinate frame quantities (e.g. relative position of the origin \mathbf{p}_A^B or coordinate axes \mathbf{x}_A^B , \mathbf{y}_A^B and

\mathbf{z}_A^B). Unless otherwise stated, vectors are assumed to be column vectors of dimension $n \times 1$ where n defines the number of elements. We further use lowercase letters to specify relative positions without defined coordinate frames. An example of this is the changing center line of the vessel \mathbf{t}_A^c . The only exception to this is the gravity vector \mathbf{g}_A , which does not specify a reference frame or lowercase subscript, as gravity is a world-implicit quantity (e.g. implying a specific orientation). Additionally, rotation matrices for rotations around specific coordinate axes are denoted as $\mathbf{R}_{x,A}$, $\mathbf{R}_{y,A}$ or $\mathbf{R}_{z,A}$ for rotations around \mathbf{x}_A , \mathbf{y}_A and \mathbf{z}_A respectively.

The robotic pose is defined as three positional coordinates and roll pitch and yaw

$$\mathbf{x} = [p_x, p_y, p_z, \theta_r, \theta_p, \theta_y] \quad (\text{A.2})$$

Equivalently, the robotic state may be expressed via its six joint angles

$$\mathbf{q} = [q_{l1}, q_{l2}, q_{l3}, q_{l4}, q_{l5}, q_{l6}] \quad (\text{A.3})$$

Note that the ultimate joint angle (j7), corresponding to the jaw opening is excluded as it stands separately to the other joints and is mostly ignored for the largest part of this work. That is because the jaw remains either fixed, in the case of a pick up device, or close in the case of a cutting tool.

The forward kinematics solution can be calculated by multiplying the parameterised transformations from the robots base until the tool tip (e.g. following the Denavit-Hartenberg convention).

$$\mathbf{x} = \mathbf{f}(\mathbf{q}) \quad (\text{A.4})$$

Inverse Kinematics are the inverse of the forward kinematics, defined as

$$\mathbf{q} = \mathbf{f}^{-1}(\mathbf{x}) \quad (\text{A.5})$$

Note that the solution to this equation is generally not guaranteed to exist in symbolic form. A general approach is to approximate the solution numerically. In this work the inverse solution is provided by the dVRK software framework.

A.3 Planar Projections

For the projection of an arbitrary point \mathbf{x}_a via an arbitrary unit vector \mathbf{v}_a into a plane defined by point \mathbf{x}_p and normal vector \mathbf{n}_p the following equation must hold

$$\mathbf{n}_p^T \cdot (\mathbf{x}_a - \underbrace{(\mathbf{x}_p + \sigma \mathbf{v}_a)}_{\mathbf{x}_{a,proj}}) = 0 \quad (\text{A.6})$$

Solving for σ and plugging the result into the definition of $\mathbf{x}_{a,proj}$ leads to the following result

$$\mathbf{x}_{a,proj} = \mathbf{x}_p + \underbrace{\left(\frac{\mathbf{n}_p^T \cdot (\mathbf{x}_p - \mathbf{x}_a)}{\mathbf{n}_p^T \cdot \mathbf{v}_a} \right)}_{\sigma} \mathbf{n}_p \quad (\text{A.7})$$

Note that in the particular case of \mathbf{v}_a being the normal vector, $\mathbf{n}_p^T \cdot \mathbf{n}_p = 1$ reduces the denominator leading to

$$\mathbf{x}_{a,proj} = \mathbf{x}_p + \underbrace{(\mathbf{n}_p^T \cdot (\mathbf{x}_p - \mathbf{x}_a))}_{\sigma} \mathbf{n}_p \quad (\text{A.8})$$

A.4 Quaternion Maths

Rather than defining the pose of the robot as a homogeneous transformation, it can be handy to use a position and unit quaternion representation. Quaternions have some advantageous properties that can be made use of in the context of robotic sensor fusion and control. Furthermore, they reduce the number of parameters needed to describe a rotation from 9 (3×3 rotation matrix) to four in the following form

$$\mathbf{q} = (q_w, q_x, q_y, q_z) \quad (\text{A.9})$$

The conversion between unit quaternions and Rotation matrix may be defined in the following way:

$$\begin{aligned}
r_{1,1} &= (q_w)^2 + (q_x)^2 - (q_y)^2 - (q_z)^2 \\
r_{2,1} &= 2.0 * (q_x * q_y + q_w * q_z) \\
r_{3,1} &= 2.0 * (q_x * q_z - q_w * q_y) \\
r_{1,2} &= 2.0 * (q_x * q_y - q_w * q_z) \\
r_{2,2} &= (q_w)^2 - (q_x)^2 + (q_y)^2 - (q_z)^2 \\
r_{3,2} &= 2.0 * (q_w * q_x + q_y * q_z) \\
r_{1,3} &= 2.0 * (q_w * q_y + q_x * q_z) \\
r_{2,3} &= 2.0 * (q_y * q_z - q_w * q_x) \\
r_{3,3} &= (q_w)^2 - (q_x)^2 - (q_y)^2 + (q_z)^2
\end{aligned} \tag{A.10}$$

The quaternion product $\mathbf{p} \otimes \mathbf{q}$ is defined as

$$\mathbf{p} \otimes \mathbf{q} = \begin{bmatrix} p_w q_w - p_x q_x - p_y q_y - p_z q_z \\ p_w q_x + p_x q_w + p_y q_z - p_z q_y \\ p_w q_y - p_x q_z + p_y q_w + p_z q_x \\ p_w q_z + p_x q_y - p_y q_x + p_z q_w \end{bmatrix} \tag{A.11}$$

Generally the quaternion product is not commutative meaning $\mathbf{p} \otimes \mathbf{q} \neq \mathbf{q} \otimes \mathbf{p}$

A.4.1 Point Set Notation

Curved brackets are used to denote point sets e.g. $\{A\}$, such as the convex hull. To denote individual points within this set $p_i^{(A)}$ is used. Additional superscription may be used to further denote the set such as $\{A_{CV}\}$ and $p_i^{(A_{CV})}$, to denote a convex hull set

Bibliography

- [1] G. A. Fontanelli, F. Ficuciello, L. Villani, and B. Siciliano, “Modelling and identification of the da Vinci Research Kit robotic arms,” in *IEEE International Conference on Intelligent Robots and Systems (IROS)*, pp. 1464–1469, 2017.
- [2] G. Z. Yang, J. Cambias, K. Cleary, E. Daimler, J. Drake, P. E. Dupont, N. Hata, P. Kazanzides, S. Martel, R. V. Patel, V. J. Santos, and R. H. Taylor, “Medical robotics - Regulatory, ethical, and legal considerations for increasing levels of autonomy,” *Science Robotics*, vol. 2, no. 4, 2017.
- [3] D. Jones, N. Marahrens, D. Sarikaya, and P. Valdastri, “Autonomy in robot-assisted minimally invasive surgery,” *Robotica*, 2023, ready for submission.
- [4] J. Leven, D. Burschka, R. Kumar, G. Zhang, S. Blumenkranz, X. D. Dai, M. Awad, G. D. Hager, M. Marohn, M. Choti, C. Hasser, and R. H. Taylor, “DaVinci Canvas: A Telerobotic Surgical System with Integrated, Robot-Assisted, Laparoscopic Ultrasound Capability,” in *Medical Image Computing And Computer-Assisted Intervention (MICCAI)*, pp. 811–818, Springer, 2005.
- [5] Z. Chua and A. M. Okamura, “A modular 3-degrees-of-freedom force sensor for robot-assisted minimally invasive surgery research,” *Sensors*, vol. 23, no. 11, p. 5230, 2023.
- [6] P. Pratt, A. Hughes-hallett, L. Zhang, and N. Patel, “Autonomous Ultrasound-Guided Tissue Dissection,” in *Medical Image Computing And Computer-Assisted Intervention (MICCAI)*, Springer, 2015.
- [7] C. Schneider, C. Nguan, R. Rohling, and S. Salcudean, “Tracked ”pick-Up” ultrasound for robot-assisted minimally invasive surgery,” *IEEE Transactions on Biomedical Engineering*, vol. 63, no. 2, pp. 260–268, 2016.

- [8] S. McKinley, A. Garg, S. Sen, D. V. Gealy, J. P. McKinley, Y. Jen, M. Guo, D. Boyd, and K. Goldberg, “An interchangeable surgical instrument system with application to supervised automation of multilateral tumor resection,” in *IEEE International Conference on Automation Science and Engineering (CASE)*, pp. 821–826, 2016.
- [9] C. M. I. Quarato, D. Lacedonia, M. Salvemini, G. Tuccari, G. Mastrodonato, R. Villani, L. A. Fiore, G. Scioscia, A. Mirijello, A. Saponara, and M. Sperandeo, “A Review on Biological Effects of Ultrasounds: Key Messages for Clinicians,” *Diagnostics*, vol. 13, no. 5, pp. 1–29, 2023.
- [10] W. Zhang, D. Yin, X. Chen, S. Zhang, F. Meng, H. Guo, S. Liang, S. Zhou, S. Liu, L. Sun, X. Guo, H. Luo, B. He, D. Xiao, W. Cai, C. Fang, L. Liu, and F. Jia, “Morphologic Change of In Vivo Porcine Liver Under 13mmHg Pneumoperitoneum Pressure,” *Surgical Laparoscopy Endoscopy & Percutaneous Techniques*, vol. 31, no. 6, 2021.
- [11] J. Keating and S. Singhal, “Novel Methods of Intraoperative Localization and Margin Assessment of Pulmonary Nodules,” *Seminars in Thoracic and Cardiovascular Surgery*, vol. 28, no. 1, pp. 127–136, 2016.
- [12] T. L. Walker, R. Bamford, and M. Finch-Jones, “Intraoperative ultrasound for the colorectal surgeon: current trends and barriers,” *ANZ Journal of Surgery*, vol. 87, no. 9, pp. 671–676, 2017.
- [13] E. J. Hagopian, “Liver ultrasound: A key procedure in the surgeon’s toolbox,” *Journal of Surgical Oncology*, vol. 122, no. 1, pp. 61–69, 2020.
- [14] P. Kazanzides, Z. Chen, A. Deguet, G. S. Fischer, R. H. Taylor, and S. P. Dimaio, “An open-source research kit for the da Vinci® Surgical System,” in *IEEE International Conference on Robotics and Automation (ICRA)*, pp. 6434–6439, IEEE, 2014.
- [15] Z. Chen, A. Deguet, R. H. Taylor, and P. Kazanzides, “Software architecture of the da vinci research kit,” in *Proceedings of IEEE International Conference on Robotic Computing*, pp. 180–187, 2017.
- [16] A. Attanasio, B. Scaglioni, E. De Momi, P. Fiorini, and P. Valdastri, “Autonomy in Surgical Robotics,” *Annual Review of Control, Robotics, and Autonomous Systems*, vol. 4, no. 1, pp. 651–679, 2021.

- [17] T. Haidegger, “Autonomy for Surgical Robots: Concepts and Paradigms,” *IEEE Transactions on Medical Robotics and Bionics*, vol. 1, no. 2, pp. 65–76, 2019.
- [18] O. Mohareri, C. Schneider, and S. Salcudean, “Bimanual telerobotic surgery with asymmetric force feedback: A daVinci® surgical system implementation,” in *IEEE International Conference on Intelligent Robots and Systems (IROS)*, pp. 4272–4277, IEEE, 2014.
- [19] N. Zevallos, R. A. Srivatsan, H. Salman, L. Li, J. Qian, S. Saxena, M. Xu, K. Patath, and H. Choset, “A surgical system for automatic registration, stiffness mapping and dynamic image overlay,” in *IEEE International Symposium on Medical Robotics*, 2018.
- [20] N. Zevallos, A. Srivatsan Rangaprasad, H. Salman, L. Li, J. Qian, S. Saxena, M. Xu, K. Patath, and H. Choset, “A Real-time Augmented Reality Surgical System for Overlaying Stiffness Information,” in *Proceedings of Robotics: Science and Systems*, 2018.
- [21] R. Elek, T. D. Nagy, D. Nagy, T. Garamvölgyi, B. Takács, P. Galambos, J. K. Tar, I. J. Rudas, and T. Haidegger, “Towards surgical subtask automation - Blunt dissection,” in *IEEE International Conference on Intelligent Engineering Systems*, pp. 253–257, 2017.
- [22] T. D. Nagy, M. Takacs, I. J. Rudas, and T. Haidegger, “Surgical subtask automation - Soft tissue retraction,” in *IEEE World Symposium on Applied Machine Intelligence and Informatics*, pp. 55–60, 2018.
- [23] K. Omote, H. Feussner, A. Ungeheuer, K. Arbter, G. Q. Wei, J. R. Siewert, and G. Hirzinger, “Self-guided robotic camera control for laparoscopic surgery compared with human camera control,” *American Journal of Surgery*, vol. 177, no. 4, pp. 321–324, 1999.
- [24] C. Staub, T. Osa, A. Knoll, and R. Bauernschmitt, “Automation of tissue piercing using circular needles and vision guidance for computer aided laparoscopic surgery,” in *IEEE International Conference on Robotics and Automation (ICRA)*, pp. 4585–4590, 2010.
- [25] H. Mayer, F. Gomez, D. Wierstra, I. Nagy, A. Knoll, and J. Schmidhuber, “A system for robotic heart surgery that learns to tie knots using recurrent neural networks,” *Advanced Robotics*, vol. 22, no. 13-14, pp. 1521–1537, 2008.

- [26] S. McKinley, A. Garg, S. Sen, R. Kapadia, A. Murali, K. Nichols, S. Lim, S. Patil, P. Abbeel, A. M. Okamura, and K. Goldberg, “A single-use haptic palpation probe for locating subcutaneous blood vessels in robot-assisted minimally invasive surgery,” in *IEEE International Conference on Automation Science and Engineering (CASE)*, pp. 1151–1158, 2015.
- [27] S. Leonard, K. L. Wu, Y. Kim, A. Krieger, and P. C. Kim, “Smart tissue anastomosis robot (STAR): A vision-guided robotics system for laparoscopic suturing,” *IEEE Transactions on Biomedical Engineering*, vol. 61, no. 4, pp. 1305–1317, 2014.
- [28] S. Leonard, A. Shademan, Y. Kim, A. Krieger, and P. C. Kim, “Smart Tissue Anastomosis Robot (STAR): Accuracy evaluation for supervisory suturing using near-infrared fluorescent markers,” in *IEEE International Conference on Robotics and Automation (ICRA)*, pp. 1889–1894, 2014.
- [29] C. D’Ettorre, G. Dwyer, X. Du, F. Chadebecq, F. Vasconcelos, E. De Momi, and D. Stoyanov, “Automated pick-up of suturing needles for robotic surgical assistance,” in *2018 IEEE International Conference on Robotics and Automation (ICRA)*, pp. 1370–1377, IEEE, 2018.
- [30] P. Pratt, A. Jaeger, A. H.-h. Erik, J. Vale, A. Darzi, T. Peters, and G.-z. Yang, “Robust ultrasound probe tracking : initial clinical experiences during robot-assisted partial nephrectomy,” *International Journal of Computer Assisted Radiology and Surgery*, vol. 10, pp. 1905–1913, 2015.
- [31] P. Mathur, G. Samei, K. Tsang, J. Lobo, and S. Salcudean, “On the feasibility of transperineal 3D ultrasound image guidance for robotic radical prostatectomy,” *International Journal of Computer Assisted Radiology and Surgery*, vol. 14, p. 923–931, 2019.
- [32] A. Attanasio, B. Scaglioni, M. Leonetti, A. F. Frangi, W. Cross, C. S. Biyani, and P. Valdastrì, “Autonomous Tissue Retraction in Robotic Assisted Minimally Invasive Surgery - A Feasibility Study,” *IEEE Robotics and Automation Letters*, vol. 5, no. 4, pp. 6528–6535, 2020.
- [33] P. Hoskins, *Diagnostic Ultrasound - Physics and Equipment*. Cambridge University Press, 2010.
- [34] J. T. Alander, I. Kaartinen, A. Laakso, T. Pättilä, T. Spillmann, V. V. Tuchin, M. Venermo, and P. Välisuo, “A Review of indocyanine green fluorescent imaging in surgery,” *International Journal of Biomedical Imaging*, vol. 2012, 2012.

- [35] S. Dietsch, L. Lindenroth, A. Stilli, and D. Stoyanov, “Imaging skins: stretchable and conformable on-organ beta particle detectors for radioguided surgery,” *Progress in Biomedical Engineering*, vol. 5, 2023.
- [36] M. F. Reiser, W. Semmler, and H. Hricak, *Magnetic resonance tomography*. Springer Science & Business Media, 2007.
- [37] E. Pauwels, D. Van Loo, P. Cornillie, L. Brabant, and L. Van Hoorebeke, “An exploratory study of contrast agents for soft tissue visualization by means of high resolution x-ray computed tomography imaging,” *Journal of microscopy*, vol. 250, no. 1, pp. 21–31, 2013.
- [38] S. Boppart, A. Goodman, J. Libus, C. Pitris, C. Jesser, M. E. Brezinski, and J. Fujimoto, “High resolution imaging of endometriosis and ovarian carcinoma with optical coherence tomography: feasibility for laparoscopic-based imaging,” *BJOG: An International Journal of Obstetrics & Gynaecology*, vol. 106, no. 10, pp. 1071–1077, 1999.
- [39] V. De Luca, J. Banerjee, A. Hallack, S. Kondo, M. Makhinya, D. Nouri, L. Royer, A. Cifor, G. Dardenne, O. Goksel, M. J. Gooding, C. Klink, A. Krupa, A. Le Bras, M. Marchal, A. Moelker, W. J. Niessen, B. W. Papiez, A. Rothberg, J. Schnabel, T. van Walsum, E. Harris, M. A. Lediju Bell, and C. Tanner, “Evaluation of 2D and 3D ultrasound tracking algorithms and impact on ultrasound-guided liver radiotherapy margins,” *Medical Physics*, vol. 45, no. 11, pp. 4986–5003, 2018.
- [40] M. Makhinya and O. Goksel, “Motion Tracking in 2D Ultrasound Using Vessel Models and Robust Optic-Flow,” *MICCAI workshop: Challenge on Liver Ultrasound Tracking*, pp. 20 – 27, 2015.
- [41] A. Hallack, B. W. Papiez, A. Cifor, M. J. Gooding, and J. A. Schnabel, “Robust liver ultrasound tracking using dense distinctive image features,” *MICCAI Challenge on Liver Ultrasound Tracking (CLUST15)*, pp. 28–35, 2015.
- [42] A. J. Shepard, B. Wang, T. K. Foo, and B. P. Bednarz, “A Block Matching Based Approach with Multiple Simultaneous Templates for the Real-Time 2D Ultrasound Tracking of Liver Vessels,” *Medical Physics*, vol. 44, no. 11, pp. 5889–5900, 2017.
- [43] Q. Huang, F. Zhang, and X. Li, “Machine Learning in Ultrasound Computer-Aided Diagnostic Systems: A Survey,” *BioMed Research International*, vol. 2018, 2018.

- [44] D. Meng, L. Zhang, G. Cao, W. Cao, G. Zhang, and B. Hu, "Liver Fibrosis Classification Based on Transfer Learning and FCNet for Ultrasound Images," *IEEE Access*, vol. 5, pp. 5804 – 5810, 2017.
- [45] S. Han, H. K. Kang, J. Y. Jeong, M. H. Park, W. Kim, W. C. Bang, and Y. K. Seong, "A deep learning framework for supporting the classification of breast lesions in ultrasound images," *Physics in Medicine and Biology*, vol. 62, no. 19, pp. 7714–7728, 2017.
- [46] J. Chi, E. Walia, P. Babyn, J. Wang, G. Groot, and M. Eramian, "Thyroid Nodule Classification in Ultrasound Images by Fine-Tuning Deep Convolutional Neural Network," *Journal of Digital Imaging*, vol. 30, no. 4, pp. 477–486, 2017.
- [47] Q. Zhang, Y. Xiao, W. Dai, J. Suo, C. Wang, J. Shi, and H. Zheng, "Deep learning based classification of breast tumors with shear-wave elastography," *Ultrasonics*, vol. 72, pp. 150–157, 2016.
- [48] J. Z. Cheng, D. Ni, Y. H. Chou, J. Qin, C. M. Tiu, Y. C. Chang, C. S. Huang, D. Shen, and C. M. Chen, "Computer-Aided Diagnosis with Deep Learning Architecture: Applications to Breast Lesions in US Images and Pulmonary Nodules in CT Scans," *Scientific Reports*, vol. 6, pp. 1–13, 2016.
- [49] T. M. Hassan, M. Elmogy, and E. S. Sallam, "Diagnosis of Focal Liver Diseases Based on Deep Learning Technique for Ultrasound Images," *Arabian Journal for Science and Engineering*, vol. 42, no. 8, pp. 3127–3140, 2017.
- [50] O. Ronneberger, P. Fischer, and T. Brox, "U-net: Convolutional networks for biomedical image segmentation," in *Medical Image Computing And Computer-Assisted Intervention (MICCAI)*, pp. 234–241, 2015.
- [51] F. Milletari, N. Navab, and S.-A. Ahmadi, "V-Net: Fully Convolutional Neural Networks for Volumetric Medical Image Segmentation," in *International Conference on 3D Vision (3DV)*, 2016.
- [52] F. Milletari, S. A. Ahmadi, C. Kroll, A. Plate, V. Rozanski, J. Maiostre, J. Levin, O. Dietrich, B. Ertl-Wagner, K. Bötzel, and N. Navab, "Hough-CNN: Deep learning for segmentation of deep brain regions in MRI and ultrasound," *Computer Vision and Image Understanding*, vol. 164, pp. 92–102, 2017.
- [53] S. E. Salcudean, G. Bell, B. S., W. Zhu, P. Abolmaesumi, and P. Lawrence, "Robot-Assisted Diagnostic Ultrasound - Design and Feasibility Experiments," in *Medical*

- Image Computing And Computer-Assisted Intervention (MICCAI)*, pp. 1162–1172, 1999.
- [54] F. Pierrot, E. Dombre, E. Dégoulange, L. Urbain, P. Caron, S. Boudet, J. Gariépy, and J. L. Mégrien, “Hippocrate: A safe robot arm for medical applications with force feedback,” *Medical Image Analysis*, vol. 3, no. 3, pp. 285–300, 1999.
- [55] J. D. Gumprecht, T. Bauer, J. U. Stolzenburg, and T. C. Lueth, “A robotics-based flat-panel ultrasound device for continuous intraoperative transcutaneous imaging,” *Proceedings of the Annual International Conference of the IEEE Engineering in Medicine and Biology Society (EMBS)*, pp. 2152–2155, 2011.
- [56] A. M. Priester, S. Natarajan, and M. O. Culjat, “Robotic Ultrasound Systems in Medicine,” *IEEE Transactions on Ultrasonics, Ferroelectrics, and Frequency Control*, vol. 60, no. 3, pp. 507–523, 2013.
- [57] R. Elek, T. D. Nagy, D. A. Nagy, B. Takacs, P. Galambos, I. Rudas, and T. Haidegger, “Robotic platforms for ultrasound diagnostics and treatment,” *2017 IEEE International Conference on Systems, Man, and Cybernetics, SMC 2017*, vol. 2017-Janua, pp. 1752–1757, 2017.
- [58] Z. Jiang, S. E. Salcudean, and N. Navab, “Robotic ultrasound imaging: State-of-the-art and future perspectives,” *Medical Image Analysis*, vol. 89, 2023.
- [59] V. G. Mallapragada, N. Sarkar, and T. K. Podder, “Robot assisted real-time tumor manipulation for breast biopsy,” in *IEEE International Conference on Robotics and Automation*, pp. 2515–2520, 2008.
- [60] P. Abolmaesumi, S. E. Salcudean, W. H. Zhu, M. R. Siroospour, and S. P. DiMaio, “Image-guided control of a robot for medical ultrasound,” *IEEE Transactions on Robotics and Automation*, vol. 18, no. 1, pp. 11–23, 2002.
- [61] M. Sauvee, P. Poignet, and E. Dombre, “Ultrasound image-based visual servoing of a surgical instrument through nonlinear model predictive control,” *International Journal of Robotics Research*, vol. 27, no. 1, pp. 25–40, 2008.
- [62] P. Chatelain, A. Krupa, and M. Marchal, “Real-time needle detection and tracking using a visually servoed 3D ultrasound probe,” in *IEEE International Conference on Robotics and Automation (ICRA)*, pp. 1679–1681, IEEE, 2013.

- [63] M. A. Vitrani, G. Morel, and T. Ortmaier, "Automatic Guidance of a Surgical Instrument with Ultrasound Based Visual Servoing," in *IEEE International Conference on Robotics and Automation (ICRA)*, pp. 508–513, 2005.
- [64] J. Hong, T. Dohi, M. Hashizume, K. Konishi, and N. Hata, "An ultrasound-driven needle-insertion robot for percutaneous cholecystostomy," *Physics in Medicine and Biology*, vol. 49, no. 3, pp. 441–455, 2004.
- [65] A. Krupa, G. Fichtinger, and G. D. Hager, "Full motion tracking in ultrasound using image speckle information and visual servoing," in *IEEE International Conference on Robotics and Automation (ICRA)*, pp. 2458–2464, 2007.
- [66] A. Krupa, G. Fichtinger, and G. D. Hager, "Real-time tissue tracking with B-mode ultrasound using speckle and visual servoing.," in *Medical Image Computing And Computer-Assisted Intervention (MICCAI)*, pp. 1–8, Springer, 2007.
- [67] A. Krupa, G. Fichtinger, and G. Hager, "Rigid motion compensation with a robotized 2D ultrasound probe using speckle information and visual servoing," in *Advanced Sensing and Sensor Integration in Medical Robotics, Workshop at the IEEE International Conference on Robotics and Automation (ICRA)*, 2009.
- [68] W. Bachta and A. Krupa, "Towards ultrasound image-based visual servoing," *Proceedings - IEEE International Conference on Robotics and Automation*, vol. 2006, no. May, pp. 4112–4117, 2006.
- [69] R. Mebarki, A. Krupa, and F. Chaumette, "2-D ultrasound probe complete guidance by visual servoing using image moments," *IEEE Transactions on Robotics*, vol. 26, no. 2, pp. 296–306, 2010.
- [70] R. Mebarki, A. Krupa, and F. Chaumette, "Image moments-based ultrasound visual servoing," in *IEEE International Conference on Robotics and Automation (ICRA)*, pp. 113–119, 2008.
- [71] R. Mebarki, A. Krupa, and F. Chaumette, "Modeling and 3D local estimation for in-plane and out-of-plane motion guidance by 2D ultrasound-based visual servoing," in *IEEE International Conference on Robotics and Automation (ICRA)*, pp. 319–325, IEEE, 2009.
- [72] C. Nadeau and A. Krupa, "A multi-plane approach for ultrasound visual servoing: Application to a registration task," in *IEEE International Conference on Intelligent Robots and Systems*, pp. 5706–5711, IEEE, 2010.

- [73] C. Nadeau, A. Krupa, J. Petr, and C. Barillot, “Moments-based ultrasound visual servoing: From a mono- to multiplane approach,” *IEEE Transactions on Robotics*, vol. 32, no. 6, pp. 1558–1564, 2010.
- [74] C. Nadeau and A. Krupa, “Intensity-based ultrasound visual servoing: Modeling and validation with 2-D and 3-D probes,” *IEEE Transactions on Robotics*, vol. 29, no. 4, pp. 1003–1015, 2013.
- [75] C. Nadeau, H. Ren, A. Krupa, and P. Dupont, “Intensity-based visual servoing for instrument and tissue tracking in 3D ultrasound volumes,” *IEEE Transactions on Automation Science and Engineering*, vol. 12, no. 1, pp. 367–371, 2015.
- [76] L. Royer, A. Krupa, G. Dardenne, A. Le Bras, E. Marchand, and M. Marchal, “Real-time target tracking of soft tissues in 3D ultrasound images based on robust visual information and mechanical simulation,” *Medical Image Analysis*, vol. 35, pp. 582–598, 2017.
- [77] L. Royer, *Real-time tracking of deformable targets in 3D ultrasound sequences*. PhD thesis, University of Rennes, 2016.
- [78] L. Royer, M. Marchal, A. Le Bras, G. Dardenne, and A. Krupa, “Real-time tracking of deformable target in 3D ultrasound images,” in *IEEE International Conference on Robotics and Automation*, pp. 2430–2435, 2015.
- [79] L. Royer, G. Dardenne, A. L. Bras, M. Marchal, and A. Krupa, “Tracking of Non-rigid Targets in 3D US Images: Results on CLUST 2015,” in *Medical Image Computing And Computer-Assisted Intervention (MICCAI)*, 2015.
- [80] D. Lee and A. Krupa, “Intensity-based visual servoing for non-rigid motion compensation of soft tissue structures due to physiological motion using 4D ultrasound,” in *IEEE International Conference on Intelligent Robots and Systems (IROS)*, pp. 2831–2836, IEEE, 2011.
- [81] C. Nadeau, A. Krupa, P. Moreira, N. Zemiti, P. Poignet, and J. Gangloff, “Active stabilization of ultrasound image for robotically-assisted medical procedures,” in *Hamlyn Symposium on Medical robotics*, 2012.
- [82] O. Zettinig, B. Fuerst, R. Kojcev, M. Esposito, M. Salehi, W. Wein, J. Rackerseder, E. Sinibaldi, B. Frisch, and N. Navab, “Toward real-time 3D ultrasound registration-based visual servoing for interventional navigation,” in *IEEE International Conference on Robotics and Automation (ICRA)*, pp. 945–950, 2016.

- [83] O. Zettinig, B. Frisch, S. Virga, M. Esposito, A. Rienmüller, B. Meyer, C. Hennersperger, Y. M. Ryang, and N. Navab, “3D ultrasound registration-based visual servoing for neurosurgical navigation,” *International Journal of Computer Assisted Radiology and Surgery*, vol. 12, no. 9, pp. 1607–1619, 2017.
- [84] B. Fuerst, W. Wein, M. Müller, and N. Navab, “Automatic ultrasound-MRI registration for neurosurgery using the 2D and 3D LC2 Metric,” *Medical Image Analysis*, vol. 18, no. 8, pp. 1312–1319, 2014.
- [85] S. Virga, O. Zettinig, M. Esposito, K. Pfister, B. Frisch, T. Neff, N. Navab, and C. Hennersperger, “Automatic force-compliant robotic Ultrasound screening of abdominal aortic aneurysms,” in *IEEE International Conference on Intelligent Robots and Systems (IROS)*, pp. 508–513, 2016.
- [86] C. Hennersperger, B. Fuerst, S. Virga, O. Zettinig, B. Frisch, T. Neff, and N. Navab, “Towards MRI-Based Autonomous Robotic US Acquisitions: A First Feasibility Study,” *IEEE Transactions on Medical Imaging*, vol. 36, no. 2, pp. 538–548, 2017.
- [87] S. Virga, R. Göbl, M. Baust, N. Navab, and C. Hennersperger, “Use the force : deformation correction in robotic 3D ultrasound,” *International Journal of Computer Assisted Radiology and Surgery*, vol. 13, no. 5, pp. 619–627, 2018.
- [88] Z. Jiang, Z. Li, M. Grimm, M. Zhou, M. Esposito, W. Wein, W. Stechele, T. Wendler, and N. Navab, “Autonomous Robotic Screening of Tubular Structures based only on Real-Time Ultrasound Imaging Feedback,” *IEEE Transactions on Industrial Electronics*, vol. 69, no. 7, pp. 7064 – 7075, 2021.
- [89] V. Groenhuis, F. Visentin, F. J. Siepel, B. M. Maris, D. Dall’alba, P. Fiorini, and S. Stramigioli, “Analytical derivation of elasticity in breast phantoms for deformation tracking,” *International Journal of Computer Assisted Radiology and Surgery*, vol. 13, no. 10, pp. 1641–1650, 2018.
- [90] E. Tagliabue, D. Dall’Alba, E. Magnabosco, C. Tenga, I. Peterlik, and P. Fiorini, “Position-based modeling of lesion displacement in ultrasound-guided breast biopsy,” *International Journal of Computer Assisted Radiology and Surgery*, vol. 14, no. 8, pp. 1329–1339, 2019.
- [91] A. Nikolaev, H. H. G. Hansen, L. de Jong, E. Tagliabue, B. Maris, V. Groenhuis, F. Siepel, M. Caballo, I. Sechopoulos, and C. L. de Korte, “Ultrasound-guided breast biopsy of ultrasound occult lesions using multimodality image co-registration

- and tissue displacement tracking,” *Medical Imaging 2019: Ultrasonic Imaging and Tomography*, vol. 10955, 2019.
- [92] M. K. Welleweerd, A. G. D. Groot, S. O. D. Looijer, F. J. Siepel, and S. Stramigioli, “Automated robotic breast ultrasound acquisition using ultrasound feedback,” *Proceedings - IEEE International Conference on Robotics and Automation*, 2020.
- [93] M. K. Welleweerd, F. J. Siepel, V. Groenhuis, J. Veltman, and S. Stramigioli, “Design of an end-effector for robot-assisted ultrasound-guided breast biopsies,” *International Journal of Computer Assisted Radiology and Surgery*, vol. 15, no. 4, pp. 681–690, 2020.
- [94] P. K. Weber, J. C. Schlegel, J. Meiche, L. Peter, and U. Harland, “A system for ultrasound based intraoperative navigation in spine surgery,” in *IEEE Ultrasonics Symposium*, pp. 1361–1364, IEEE, 2001.
- [95] Z. Zhou, Z. Wang, Z. Zheng, J. Cao, C. Zhang, Z. He, W. Lv, and J. Hu, “An “ alternative finger ” in robotic-assisted thoracic surgery : intraoperative ultrasound localization of pulmonary nodules,” *Medical Ultrasound*, vol. 19, no. 4, pp. 374–379, 2017.
- [96] C. M. Schneider, G. W. D. Ii, C. J. Hasser, M. A. Choti, S. P. Dimaiio, and R. H. Taylor, “Robot-Assisted Laparoscopic Ultrasound,” in *International Conference on Information Processing in Computer-Assisted Interventions (IPCAI)*, pp. 67–80, 2010.
- [97] R. P. Budde, R. Meijer, P. F. Bakker, C. Borst, and P. F. Gründeman, “Endoscopic localization and assessment of coronary arteries by 13 MHz epicardial ultrasound,” *Annals of Thoracic Surgery*, vol. 77, no. 5, pp. 1586–1592, 2004.
- [98] R. P. Budde, T. C. Dessing, R. Meijer, P. F. Bakker, C. Borst, and P. F. Gründeman, “Robot-assisted 13 MHz epicardial ultrasound for endoscopic quality assessment of coronary anastomoses,” *Interactive Cardiovascular and Thoracic Surgery*, vol. 3, no. 4, pp. 616–620, 2004.
- [99] I. N. Fleming, C. Kut, K. J. Macura, L. M. Su, H. Rivaz, C. Schneider, U. Hamper, T. Lotan, R. Taylor, G. Hager, and E. Boctor, “Ultrasound elastography as a tool for imaging guidance during prostatectomy: Initial experience,” *Medical Science Monitor*, vol. 18, no. 11, pp. 635–642, 2012.

- [100] C. M. Schneider, *Characterization of Renal Tissue using Ultrasound and Elastography*. PhD thesis, University of British Columbia, Vancouver, CA, 2017.
- [101] A. Stilli, E. Dimitrakakis, C. D. Ettore, M. Tran, and D. Stoyanov, “Pneumatically Attachable Flexible Rails for Track-Guided Ultrasound Scanning in Robotic-Assisted Partial Nephrectomy — A Preliminary Design Study *,” in *IEEE International Conference on Robotics and Automation*, 2019.
- [102] C. Wang, C. Komninos, S. Andersen, C. D’Ettore, G. Dwyer, E. Maneas, P. Edwards, A. Desjardins, A. Stilli, and D. Stoyanov, “Ultrasound 3D reconstruction of malignant masses in robotic-assisted partial nephrectomy using the PAF rail system: a comparison study,” *International Journal of Computer Assisted Radiology and Surgery*, vol. 15, no. 7, pp. 1147–1155, 2020.
- [103] L. Zhang, M. Ye, P.-l. Chan, and G.-Z. Yang, “Real-time surgical tool tracking and pose estimation using a hybrid cylindrical marker,” *International Journal of Computer Assisted Radiology and Surgery*, vol. 12, pp. 921–930, 2017.
- [104] C. Schneider, A. Baghani, R. Rohling, and S. Salcudean, “Remote ultrasound palpation for robotic interventions using absolute elastography,” in *Medical Image Computing And Computer-Assisted Intervention (MICCAI)*, pp. 42–49, 2012.
- [105] C. Schneider, J. Guerrero, C. Nguan, R. Rohling, and S. Salcudean, “Intra-operative Pick-Up Ultrasound for Robot Assisted Surgery in Vessel Extraction and Registration - A Feasibility Study,” in *Information Processing in Computer-Assisted Interventions. IPCAI 2011. Lecture Notes in Computer Science*, vol. 6689, 2011.
- [106] I. Tong, L. Metcalf, C. Hennessey, and S. E. Salcudean, “Free Head Movement Eye Gaze Contingent Ultrasound Interfaces for the da Vinci Surgical System,” *IEEE Robotics and Automation Letters*, vol. 3, no. 3, pp. 2137–2143, 2018.
- [107] L. Zhang, M. Ye, S. Giannarou, P. Pratt, and G.-Z. Yang, “Motion-Compensated Autonomous Scanning for Tumour Localisation using Intraoperative Ultrasound,” in *Medical Image Computing and Computer-Assisted Intervention*, 2017.
- [108] J. Zhan, J. Cartucho, and S. Giannarou, “Autonomous tissue scanning under free-form motion for intraoperative tissue characterisation,” in *2020 IEEE International Conference on Robotics and Automation (ICRA)*, 2020.

- [109] J.-a. Long, B. H. Lee, J. Guillotreau, R. Autorino, H. Laydner, R. Yakoubi, E. Rizkala, R. J. Stein, J. H. Kaouk, and G.-P. Haber, “Real-Time Robotic Transrectal Ultrasound Navigation During Robotic Radical Prostatectomy : Initial Clinical Experience,” *Journal of Urology*, vol. 80, no. 3, pp. 608–613, 2012.
- [110] D. C. Abreu, S. Shoji, A. C. Goh, A. K. Berger, A. J. Hung, M. M. Desai, M. Aron, I. S. Gill, and O. Ukimura, “Robotic Transrectal Ultrasonography During Robot-Assisted Radical Prostatectomy,” *European Urology*, vol. 62, pp. 341–348, 2012.
- [111] M. Han, C. Kim, P. Mozer, F. Schäfer, S. Badaan, B. Vigaru, K. Tseng, D. Petrisor, B. Trock, and D. Stoianovici, “Tandem-robot Assisted Laparoscopic Radical Prostatectomy to Improve Neurovascular Bundle Visualization : A Feasibility Study,” *Journal of Urology*, vol. 80, no. 3, pp. 502–506, 2012.
- [112] O. Mohareri, M. Ramezani, T. Adebar, P. Abolmaesumi, and S. Salcudean, “Automatic detection and localization of da Vinci tool tips in 3D ultrasound,” in *International Conference on Information Processing in Computer-Assisted Interventions (IPCAI)*, pp. 22–32, 2012.
- [113] O. Mohareri, C. Schneider, T. K. Adebar, M. C. Yip, P. Black, C. Y. Nguan, D. Bergman, J. Seroger, S. DiMaio, and S. E. Salcudean, “Ultrasound-based image guidance for robot-assisted laparoscopic radical prostatectomy: Initial in-vivo results,” in *International Conference on Information Processing in Computer-Assisted Interventions (IPCAI)*, pp. 40–50, 2013.
- [114] G. Samei, K. Tsang, C. Kesch, J. Lobo, S. Hor, O. Mohareri, S. Chang, S. L. Goldenberg, P. C. Black, and S. Salcudean, “A partial augmented reality system with live ultrasound and registered preoperative MRI for guiding robot-assisted radical prostatectomy,” *Medical Image Analysis*, vol. 60, 2020.
- [115] D. Zbyszewski, H. Liu, P. Puangmali, K. Althoefer, S. Catarina, L. D. Seneviratne, and B. Challacombe, “Wheel/Tissue Force Interaction: A New Concept for Soft Tissue Diagnosis during MIS,” in *Annual International Conference of the IEEE Engineering in Medicine and Biology Society*, 2008.
- [116] R. Yasin, L. Wang, C. Abah, and N. Simaan, “Using Continuum Robots for Force-Controlled Semi Autonomous Organ Exploration and Registration,” in *International Symposium on Medical Robotics (ISMR)*, IEEE, 2018.

- [117] E. Ayvali, A. Ansari, L. Wang, N. Simaan, and H. Choset, “Utility-Guided Palpation for Locating Tissue Abnormalities,” *IEEE Robotics and Automation Letters*, vol. 2, no. 2, pp. 864–871, 2017.
- [118] L. Li, B. Yu, C. Yang, P. Vagdargi, R. A. Srivatsan, and H. Choset, “Development of an inexpensive tri-axial force sensor for minimally invasive surgery,” in *IEEE International Conference on Intelligent Robots and Systems (IROS)*, pp. 906–913, 2017.
- [119] G. A. Fontanelli, L. R. Buonocore, F. Ficuciello, L. Villani, and B. Siciliano, “A Novel Force Sensing Integrated into the Trocar for Minimally Invasive Robotic Surgery,” in *IEEE International Conference on Intelligent Robots and Systems (IROS)*, 2017.
- [120] A. Marban, V. Srinivasan, W. Samek, J. Fern, and A. Casals, “Estimation of Interaction Forces in Robotic Surgery using a Semi-Supervised Deep Neural Network Model,” in *IEEE International Conference on Intelligent Robots and Systems (IROS)*, 2018.
- [121] A. Marban, V. Srinivasan, W. Samek, J. Fernández, and A. Casals, “A recurrent convolutional neural network approach for sensorless force estimation in robotic surgery,” *Biomedical Signal Processing and Control*, vol. 50, pp. 134–150, 2019.
- [122] Z. Chua, A. M. Jarc, and A. M. Okamura, “Toward force estimation in robot-assisted surgery using deep learning with vision and robot state,” in *2021 IEEE International Conference on Robotics and Automation (ICRA)*, IEEE, 2021.
- [123] Z. Chua and A. M. Okamura, “Characterization of real-time haptic feedback from multimodal neural network-based force estimates during teleoperation,” in *2022 IEEE/RSJ International Conference on Intelligent Robots and Systems (IROS)*, pp. 1471–1478, IEEE, 2022.
- [124] H. Sang, J. Y. Fooladi, R. Monfaredi, E. Wilson, H. Fooladi, and K. Cleary, “External force estimation and implementation in robotically assisted minimally invasive surgery,” *International Journal of Medical Robotics and Computer Assisted Surgery*, vol. 13, no. 2, pp. 1–15, 2017.
- [125] F. Piqué, M. N. Boushaki, M. Brancadoro, E. D. Momi, and A. Menciassi, “Dynamic Modeling of the Da Vinci Research Kit Arm for the Estimation of Interaction Wrench,” in *International Symposium on Medical Robotics (ISMR)*, 2019.

- [126] R. A. Gondokaryono, “Master Thesis: Cooperative Object Manipulation with Force Tracking on the da Vinci Research Kit,” tech. rep., Worcester Polytechnic Institute, 2018.
- [127] Y. Wang, R. Gondokaryono, A. Munawar, and G. S. Fischer, “A Convex Optimization-Based Dynamic Model Identification Package for the da Vinci Research Kit,” *IEEE Robotics and Automation Letters*, vol. 4, no. 4, pp. 3657–3664, 2019.
- [128] N. Yilmaz, J. Y. Wu, P. Kazanzides, and U. Tumerdem, “Neural Network based Inverse Dynamics Identification and External Force Estimation on the da Vinci Research Kit,” in *IEEE International Conference on Robotics and Automation*, pp. 1387–1393, 2020.
- [129] N. Tran, J. Y. Wu, A. Deguet, and P. Kazanzides, “A Deep Learning Approach to Intrinsic Force Sensing on the da Vinci Surgical Robot,” in *IEEE International Conference on Robotic Computing, IRC 2020*, pp. 25–32, 2020.
- [130] S. K. Chang, W. W. Hlaing, L. Yang, and C. K. Chui, “Current technology in navigation and robotics for liver tumours ablation,” *Annals of the Academy of Medicine Singapore*, vol. 40, no. 5, pp. 231–236, 2011.
- [131] H. G. Rau, A. P. Duessel, and S. Wurzbacher, “The use of water-jet dissection in open and laparoscopic liver resection,” *Hpb*, vol. 10, no. 4, pp. 275–280, 2008.
- [132] J. L. Hinshaw and F. T. Lee, “Cryoablation for Liver Cancer,” *Techniques in Vascular and Interventional Radiology*, vol. 10, no. 1, pp. 47–57, 2007.
- [133] N. Bhardwaj, D. A. Strickland, F. Ahmad, A. R. Dennison, and D. M. Lloyd, “Liver ablation techniques: A review,” *Surgical Endoscopy*, vol. 24, no. 2, pp. 254–265, 2010.
- [134] K. W. Huang, P. H. Lee, T. Kusano, I. Reccia, K. Jayant, and N. Habib, “Impact of cavitron ultrasonic surgical aspirator (CUSA) and bipolar radiofrequency device (Habib-4X) based hepatectomy for hepatocellular carcinoma on tumour recurrence and diseasefree survival,” *Oncotarget*, vol. 8, no. 55, pp. 1–11, 2017.
- [135] J. G. Hunter, “Exposure, dissection, and laser versus electrosurgery in laparoscopic cholecystectomy,” *The American Journal of Surgery*, vol. 165, no. 4, pp. 492–496, 1993.

- [136] S. S. Club, “A prospective analysis of 1518 laparoscopic cholecystectomies,” *The New England journal of medicine*, vol. 324, no. 16, pp. 1073–1078, 1991.
- [137] E. Schena, P. Saccomandi, and Y. Fong, “Laser Ablation for Cancer: Past, Present and Future,” *Journal of Functional Biomaterials*, vol. 8, no. 2, p. 19, 2017.
- [138] G. Pittiglio, J. H. Chandler, T. da Veiga, Z. Koszowska, M. Brockdorff, P. Lloyd, K. L. Barry, R. A. Harris, J. McLaughlan, C. Pompili, *et al.*, “Personalized magnetic tentacles for targeted photothermal cancer therapy in peripheral lungs,” *Communications Engineering*, vol. 2, no. 1, p. 50, 2023.
- [139] C. M. Pacella, G. Francica, G. G. Di Costanzo, *et al.*, “Laser ablation for small hepatocellular carcinoma,” *Radiology Research and Practice*, vol. 2011, 2011.
- [140] Z. Izadifar, Z. Izadifar, D. Chapman, and P. Babyn, “An introduction to high intensity focused ultrasound: Systematic review on principles, devices, and clinical applications,” *Journal of Clinical Medicine*, vol. 9, no. 2, pp. 1–22, 2020.
- [141] R. W. Ritchie, T. A. Leslie, G. D. Turner, I. S. Roberts‡, L. D’Urso, D. Collura, A. Demarchi, G. Muto, and M. E. Sullivan, “Laparoscopic high-intensity focused ultrasound for renal tumours: a proof of concept study,” *BJU International*, vol. 107, 2011.
- [142] A. Gunderman, R. Montayre, A. Ranjan, and Y. Chen, “Review of Robot-Assisted HIFU Therapy,” *Sensors*, vol. 23, no. 7, pp. 1–27, 2023.
- [143] B. Matthews, “Ultrasonic and Nonultrasonic Instrumentation,” *Archives of Surgery*, vol. 143, no. 6, p. 592, 2008.
- [144] B. Thananjeyan, A. Garg, S. Krishnan, C. Chen, L. Miller, and K. Goldberg, “Multilateral Surgical Pattern Cutting in 2D Orthotropic Gauze with Deep Reinforcement Learning Policies for Tensioning,” in *IEEE International Conference on Robotics and Automation (ICRA)*, pp. 2371–2378, 2017.
- [145] H. Saeidi, J. D. Opfermann, M. Kam, S. Wei, S. Léonard, M. H. Hsieh, J. U. Kang, and A. Krieger, “Autonomous robotic laparoscopic surgery for intestinal anastomosis,” *Science robotics*, vol. 7, no. 62, 2022.
- [146] J. D. Opfermann, S. Leonard, R. S. Decker, N. A. Uebele, C. E. Bayne, A. S. Joshi, and A. Krieger, “Semi-autonomous electrosurgery for tumor resection using a multi-degree of freedom electrosurgical tool and visual servoing,” in *2017 IEEE/RSJ*

- International Conference on Intelligent Robots and Systems (IROS)*, pp. 3653–3660, IEEE, 2017.
- [147] H. Saeidi, J. Ge, M. Kam, J. Opfermann, S. Leonard, A. Joshi, and A. Krieger, “Supervised autonomous electrosurgery via biocompatible near-infrared tissue tracking techniques,” *IEEE transactions on medical robotics and bionics*, vol. 1, no. 4, pp. 228–236, 2019.
- [148] W. J. Heerink, S. J. Ruiter, J. P. Pennings, B. Lansdorp, R. Vliegthart, M. Oudkerk, and K. P. de Jong, “Robotic versus Freehand Needle Positioning in CT-guided Ablation of Liver Tumors: A Randomized Controlled Trial,” *Radiology*, vol. 290, no. 3, pp. 826–832, 2019.
- [149] P. Tinguely, I. Paolucci, S. J. Ruiter, S. Weber, K. P. de Jong, D. Candinas, J. Freedman, and J. Engstrand, “Stereotactic and Robotic Minimally Invasive Thermal Ablation of Malignant Liver Tumors: A Systematic Review and Meta-Analysis,” *Frontiers in Oncology*, vol. 11, no. September, 2021.
- [150] E. Franco, D. Brujic, M. Rea, W. M. Gedroyc, and M. Ristic, “Needle-guiding robot for laser ablation of liver tumors under MRI guidance,” *IEEE/ASME Transactions on Mechatronics*, vol. 21, no. 2, pp. 931–944, 2016.
- [151] A. Cafarelli, M. Mura, A. Diodato, A. Schiappacasse, M. Santoro, G. Ciuti, and A. Menciassi, “A computer-assisted robotic platform for Focused Ultrasound Surgery: Assessment of high intensity focused ultrasound delivery,” *Proceedings of the Annual International Conference of the IEEE Engineering in Medicine and Biology Society, EMBS*, pp. 1311–1314, 2015.
- [152] A. Diodato, A. Schiappacasse, A. Cafarelli, S. Tognarelli, G. Ciuti, and A. Menciassi, “Robotic-assisted Platform for USgFUS Treatment of Moving Organs,” in *Hamlyn Symposium on Medical Robotics*, pp. 23–24, 2017.
- [153] L. Morchi, A. Mariani, A. Cafarelli, A. Diodato, S. Tognarelli, and A. Menciassi, “A Pilot Study for a Quantitative Evaluation of Acoustic Coupling in US-guided Focused Ultrasound Surgery,” in *Proceedings of the Annual International Conference of the IEEE Engineering in Medicine and Biology Society, EMBS*, pp. 2517–2520, IEEE, 2019.
- [154] V. Simoni, A. Cafarelli, S. Tognarelli, and A. Menciassi, “Ex Vivo Assessment of Multiple Parameters in High Intensity Focused Ultrasound,” *Conference Proceedings*

- of the Annual International Conference of the IEEE Engineering in Medicine and Biology Society, EMBS*, vol. 2018, pp. 5705–5708, 2018.
- [155] L. Morchi, M. Gini, A. Mariani, N. Pagliarani, A. Cafarelli, S. Tognarelli, and A. Menciassi, “A Reusable Thermochromic Phantom for Testing High Intensity Focused Ultrasound Technologies,” *Proceedings of the Annual International Conference of the IEEE Engineering in Medicine and Biology Society, EMBS*, pp. 1431–1434, 2021.
- [156] C. Sozer, A. Cafarelli, M. Brancadoro, and A. Menciassi, “Design and development of a miniaturized intra-abdominal flexible HIFU system: a proof of concept,” in *Hamlyn Symposium on Medical robotics*, 2018.
- [157] J. Kim, H. Wu, and X. Jiang, “Miniaturized focused ultrasound transducers for intravascular therapies,” in *ASME International Mechanical Engineering Congress and Exposition (IMECE)*, 2017.
- [158] H. Kim, H. Wu, N. Cho, P. Zhong, K. Mahmood, H. Lyerly, and X. Jiang, “Miniaturized Intracavitary Forward-Looking Ultrasound Transducer for Tissue Ablation,” *IEEE Trans Biomed Eng*, vol. 67, no. 7, pp. 2084–2093, 2020.
- [159] P. Dell’Oglio, P. Meershoek, T. Maurer, E. M. Wit, P. J. van Leeuwen, H. G. van der Poel, F. W. van Leeuwen, and M. N. van Oosterom, “A drop-in gamma probe for robot-assisted radioguided surgery of lymph nodes during radical prostatectomy,” *European Urology*, vol. 79, pp. 124–132, 1 2021.
- [160] D. Hu, Y. Gong, B. Hannaford, and E. J. Seibel, “Semi-autonomous simulated brain tumor ablation with RAVENII Surgical Robot using behavior tree,” *Proceedings - IEEE International Conference on Robotics and Automation*, pp. 3868–3875, 2015.
- [161] D. Hu, Y. Gong, B. Hannaford, and E. J. Seibel, “Path planning for semi-automated simulated robotic neurosurgery,” *IEEE International Conference on Intelligent Robots and Systems*, vol. 2015-December, pp. 2639–2645, 2015.
- [162] A. Diodato, M. Brancadoro, G. De Rossi, H. Abidi, D. Dall’Alba, R. Muradore, G. Ciuti, P. Fiorini, A. Menciassi, and M. Cianchetti, “Soft Robotic Manipulator for Improving Dexterity in Minimally Invasive Surgery,” *Surgical Innovation*, vol. 25, no. 1, pp. 69–76, 2018.
- [163] M. Schiffman, A. Moshfegh, A. Talenfeld, and J. J. Del Pizzo, “Laparoscopic renal cryoablation,” *Seminars in Interventional Radiology*, vol. 31, no. 1, pp. 64–69, 2014.

- [164] D. I. Galen, R. R. Pemueler, J. G. G. Leal, K. R. Abbott, J. L. Falls, and J. Macer, “Laparoscopic radiofrequency fibroid ablation: Phase ii and phase iii results,” *Journal of the Society of Laparoendoscopic Surgeons*, vol. 18, no. 2, pp. 182–190, 2014.
- [165] T. Wang, X. Y. Zhang, X. Lu, and B. Zhai, “Laparoscopic microwave ablation of hepatocellular carcinoma at liver surface: Technique effectiveness and long-term outcomes,” *Technology in Cancer Research and Treatment*, vol. 18, pp. 1–9, 2019.
- [166] J. M. Ferguson, E. Bryn Pitt, A. A. Ramirez, M. A. Siebold, A. Kuntz, N. L. Kavoussi, E. J. Barth, S. Duke Herrell, and R. J. Webster, “Toward Practical and Accurate Touch-Based Image Guidance for Robotic Partial Nephrectomy,” *IEEE Transactions on Medical Robotics and Bionics*, vol. 2, pp. 196–205, 2020.
- [167] T. K. Adebar, M. C. Yip, S. E. Salcudean, R. N. Rohling, C. Y. Nguan, and S. L. Goldenberg, “Registration of 3d ultrasound through an air-tissue boundary,” *IEEE Transactions on Medical Imaging*, vol. 31, pp. 2133–2142, 2012.
- [168] P. Zhu, W. Liao, Z. Yang Ding, H. chang Luo, B. hao Zhang, W. guang Zhang, W. Zhang, Z. guo Zhang, B. Xiang Zhang, and X. Ping Chen, “Intraoperative ultrasonography of robot-assisted laparoscopic hepatectomy: initial experiences from 110 consecutive cases,” *Surgical Endoscopy*, vol. 32, no. 10, pp. 4071–4077, 2018.
- [169] A. Hung, J., D. C. Abreu, S. Shoji, A. C. Goh, A. K. Berger, A. J. Hung, M. M. Desai, M. Aron, I. S. Gill, and O. Ukimura, “Robotic Transrectal Ultrasonography During Robot-Assisted Radical Prostatectomy,” *European Urology*, vol. 62, pp. 341–348, 2012.
- [170] S. Nia Kosari, S. Ramadurai, H. J. Chizeck, and B. Hannaford, “Control and tension estimation of a cable driven mechanism under different tensions,” *Proceedings of the ASME Design Engineering Technical Conference*, 2013.
- [171] Z. Cui, J. Cartucho, S. Giannarou, and F. R. y. Baena, “Caveats on the first-generation da Vinci Research Kit: latent technical constraints and essential calibrations,” *IEEE Robotics & Automation Magazine*, *early access*, 2022.
- [172] M. Allan, S. Ourselin, D. J. Hawkes, J. D. Kelly, and D. Stoyanov, “3-d pose estimation of articulated instruments in robotic minimally invasive surgery,” *IEEE transactions on medical imaging*, vol. 37, no. 5, pp. 1204–1213, 2018.

- [173] R. Mahony, T. Hamel, P. Morin, and E. Malis, “Nonlinear complementary filters on the special linear group,” *IEEE Transactions on Automatic Control*, vol. 53, no. 5, pp. 1203–1218, 2008.
- [174] W. Xiao and C. Wang, “Robot with Imitation Learning based on Clinical Protocols,” *Robotics and Automation Letters*, vol. 6, 2021.
- [175] A. Karamalis, W. Wein, T. Klein, and N. Navab, “Ultrasound confidence maps using random walks,” *Medical Image Analysis*, vol. 16, no. 6, pp. 1101–1112, 2012.
- [176] I. Kuhlemann, R. Bruder, F. Ernst, and A. Schweikard, “We-g-brf-09: Force- and image-adaptive strategies for robotised placement of 4d ultrasound probes,” *Medical Physics*, vol. 41, no. 6Part30, pp. 523–523, 2014.
- [177] T. J. Vogl, N. E. A. Nour-Eldin, R. M. Hammerstingl, B. Panahi, and N. N. Naguib, “Microwave Ablation (MWA): Basics, Technique and Results in Primary and Metastatic Liver Neoplasms - Review Article,” *RoFo Fortschritte auf dem Gebiet der Rontgenstrahlen und der Bildgebenden Verfahren*, vol. 189, no. 11, pp. 1055–1066, 2017.
- [178] Z. Jiang, M. Grimm, M. Zhou, J. Esteban, W. Simson, G. Zahnd, and N. Navab, “Automatic Normal Positioning of Robotic Ultrasound Probe based only on Confidence Map Optimization and Force Measurement,” *IEEE Robotics and Automation Letters*, vol. 5, 2020.
- [179] A. Taheri, P. Mansoori, L. F. Sandoval, S. R. Feldman, D. Pearce, and P. M. Williford, “Electrosurgery: Part i. basics and principles,” *Journal of the American Academy of Dermatology*, vol. 70, 2014.
- [180] Z. Cheng, D. Dall’Alba, K. L. Schwaner, P. Fiorini, and T. R. Savarimuthu, “Robot assisted electrical impedance scanning for tissue bioimpedance spectroscopy measurement,” *Measurement: Journal of the International Measurement Confederation*, vol. 195, 2022.
- [181] C. B. Barber, D. P. Dobkin, and H. Huhdanpaa, “The Quickhull Algorithm for Convex Hulls,” *ACM Transactions on Mathematical Software*, vol. 22, no. 4, pp. 469–483, 1996.
- [182] G. H. Choi, J. U. Chong, D. H. Han, J. S. Choi, and W. J. Lee, “Robotic hepatectomy: the korean experience and perspective,” *Hepatobiliary Surgery and Nutrition*, vol. 6, no. 4, 2017.

- [183] J. M. Ferguson, L. Y. Cai, A. Reed, M. Siebold, S. De, S. D. Herrell, and R. J. Webster, “Toward image-guided partial nephrectomy with the da Vinci robot: exploring surface acquisition methods for intraoperative re-registration,” in *Proceedings of Medical imaging 2018: Image-guided procedures, robotic interventions, and modeling*, vol. 10576, p. 8, 2018.
- [184] M. Siebold, J. Ferguson, B. Pitt, N. Kavoussi, N. Nimmagadda, D. Herrell, and R. J. Webster, “Choosing Statistically Safe, Variable-Thickness Margins in Robot-Assisted Partial Nephrectomy,” *2020 International Symposium on Medical Robotics, ISMR 2020*, pp. 152–158, 2020.
- [185] T. J. Dubinsky, C. Cuevas, M. K. Dighe, O. Kolokythas, and J. H. Hwang, “High-intensity focused ultrasound: current potential and oncologic applications,” *American journal of roentgenology*, vol. 190, no. 1, pp. 191–199, 2008.
- [186] M. Bailey, V. Khokhlova, O. Sapozhnikov, S. Kargl, and L. Crum, “Physical mechanisms of the therapeutic effect of ultrasound (a review),” *Acoustical Physics*, vol. 49, pp. 369–388, 2003.
- [187] M. H. Raibert and J. J. Craig, “Hybrid Position/Force Control of Manipulators,” *Journal of Dynamic Systems, Measurement, and Control*, vol. 103, pp. 126–133, 06 1981.
- [188] R. Ritchie, J. Collin, C. Coussios, and T. Leslie, “Attenuation and de-focusing during high-intensity focused ultrasound therapy through peri-nephric fat,” *Ultrasound in Medicine & Biology*, vol. 39, no. 10, pp. 1785–1793, 2013.
- [189] K. Li, J. Wang, Y. Xu, H. Qin, D. Liu, L. Liu, and M. Q.-H. Meng, “Autonomous navigation of an ultrasound probe towards standard scan planes with deep reinforcement learning,” in *2021 IEEE International Conference on Robotics and Automation (ICRA)*, pp. 8302–8308, IEEE, 2021.
- [190] A. Munawar, Y. Wang, R. Gondokaryono, and G. S. Fischer, “A Real-Time Dynamic Simulator and an Associated Front-End Representation Format for Simulating Complex Robots and Environments,” *IEEE/RSJ International Conference on Intelligent Robots and Systems (IROS)*, pp. 1875–1882, 2019.
- [191] J. Cartucho, A. Weld, S. Tukra, H. Xu, H. Matsuzaki, T. Ishikawa, M. Kwon, Y. Jang, K.-J. Kim, G. Lee, *et al.*, “Surgt: Soft-tissue tracking for robotic surgery, benchmark and challenge,” *arXiv preprint arXiv:2302.03022*, 2023.

- [192] B. Y. Cho, T. Hermans, and A. Kuntz, “Planning sensing sequences for subsurface 3d tumor mapping,” in *2021 International Symposium on Medical Robotics (ISMR)*, pp. 1–7, 2021.